Determination and application of wavefront attributes

Dissertation
zur Erlangung des Doktorgrades
an der Fakultät für
Mathematik, Informatik und Naturwissenschaften
im Fachbereich Geowissenschaften
der Universität Hamburg

vorgelegt von
Jan Walda

Hamburg, 2016

Tag der Disputation: 15.11.2016
Folgende Gutachter empfehlen die Annahme der Dissertation:
Prof. Dr. Dirk Gajewski
PD Dr. Claudia Vanelle

Abstract

Time imaging is stable and frequently used in seismic processing and stacking is an integral part of it. Stacking is usually performed along the offset in the common-midpoint (CMP) domain. Since the turn of the millennium, more advanced stacking methods are available, e.g. common-reflection-surface (CRS) and multifocusing methods. Additionally to the offset, neighbouring CMP traces are used as well, increasing data redundancy. To describe the traveltime moveout, in the CMP method only one parameter, the moveout velocity, is required which can be picked during velocity analysis. To describe the moveout of the traveltime surface of CRS-type operators and multifocusing, three parameter are necessary which causes a need for an automated parameter estimation. At the time CRS was proposed, the computational demands of a simultaneous three parameter search without an adequate initial solution were to expansive. A three step search strategy, named pragmatic approach was proposed, that searches the individual parameters in subdomains of CRS. This omits the high amount of data redundancy CRS provides, neglecting the main advantages of the method. Another problem of CRS is the occurrence of conflicting dips which is caused by intersecting events, e.g., diffractions and reflections. An deeper investigation of CRS on pure noise data shows, that steep dipping events can be caused by pure noise as well. Previous methods try to find conflicting events during the first step of the parameter estimation, simply stacking every possible operator along a parameter space using a simplified operator or interpolate from different neighbouring locations to account for them. However, they are either not reliable or very expansive and further attribute-based methods might not be able to benefit from those methods.

In this work, I suggest to use differential evolution, a global optimization method, to estimate CRS parameters reliably. Furthermore, I suggest to divide the search space in smaller cluster and apply the parameter estimation for each cluster. Therefore, the intersecting events can be found separately, allowing to treat conflicting dips properly. A comparison on complex synthetic, marine and challenging hard rock land data shows significant improvements to previous methods and demonstrate the impact on CRS wavefront attribute-based methods like diffraction separation and data enhancement which can take advantage of the proposed method to treat conflicting dips as well. A comparison of the frequency content from the CMP, CRS and CRS with the proposed parameter estimation shows, that the method does not distort the frequency content as previously. An investigation of CRS and other multiparameter stacking operators from literature shows that non-hyperbolic CRS

provides the best trade-off between accuracy and computational cost.

Zusammenfassung

Seismische Abbildungsverfahren im Zeitbereich sind stabil und werden häufig in seismischen Prozessierungs- und Stapelverfahren verwendet. Die Stapelung wird normalerweise entlang des *offset* in der *common-midpoint* (CMP) Domäne angewandt. Seit dem Jahrtausenwechsel sind fortgeschrittenere Stapelverfahren verfügbar, wie zum Beispiel *common-reflection-surface* (CRS) und *multifocusing.* Diese Methoden stapeln zusätzlich zum *offset* benachbarte CMP Spuren auf, was die Datenredundanz erhöht. Um den *moveout* der Laufzeitkurve in der CMP Methode zu beschreiben, benötigt man lediglich einen Parameter, die *moveout* Geschwindigkeit, die während der Geschwindigkeitsanalyse bestimmt werden kann. Um den *moveout* der Laufzeitfläche zu beschreiben, werden drei Parameter benötigt, die automatisch bestimmt werden müssen. Als CRS publiziert wurde, war die Rechenanforderung einer simultanen drei Parametersuche ohne angemessene initiale Lösung zu hoch. Eine drei Schritte Suchstrategie, genannt pragmatische Annäherung, wurde vorgeschlagen. Die drei Parameter werden in kleineren Domänen von CRS gesucht. Dadurch wird aber die hohe Datenredundanz von CRS vernachlässigt, einer der Hauptvorteile von CRS. Ein weiteres Problem is das Auftreten von sich kreuzenden Signalen mit verschiedenen Einfallswinkel, wie Diffraktionen und Reflektionen. Eine tiefere Analyse von CRS anhand verrauschter Daten zeigt, dass diese Signale auch von reinem Rauschen erzeugt werden können. Bisherige Methoden versuchen, die sich überlagernden Signale unterschiedlich zu berücksichtigen. Während des ersten Schrittes der Suche, durch Stapelung aller möglichen Operatoren entlang eines Parameters oder interpolieren von benachbarten Spuren. Allerdings sind diese Methoden entweder instabil, teuer oder können nicht in weiteren Attribut basierten Methoden genutzt werden.

In dieser Arbeit schlage ich vor, *differential evolution*, eine globale Optimierungsmethode, für die Parameterbestimmung zu nutzen. Zusätzlich sollte man den Suchraum in kleinere Suchräume unterteilen und in jedem kleineren Suchraum eine Parametersuche vollziehen. Dadurch können sich überlagernde Signale in unterschiedlichen Suchräumen identifiziert und berücksichtigt werden. Ein Vergleich an komplexen synthetischen, marinen und Hartgestein Landdaten zeigt deutliche Verbesserungen zu früheren Methoden. Er demonstriert den Einfluss in CRS Wellenfrontattribut basierten Methoden wie die Separation von Diffraktionen und Datenverbesserung, die mit der vorgeschlagenen Methode überlagernde Signale berücksichtigen können. Ein Vergleich der Frequenzgehalte der CMP, CRS und vorgeschlagenen erweiterten CRS Methode zeigt, dass die vorgeschlagene Methode

den Frequenzgehalt nicht verändert, anders als zuvor. Eine Analyse von CRS und anderen Operatoren, die von mehreren Parametern abhängen, zeigt, dass *non-hyperbolic* CRS den besten Kompromiss zwischen Genauigkeit und Rechenaufwand darstellt.

Contents

List of Figures

List of Tables

Chapter 1.

Introduction

The common-reflection-surface (CRS) (Müller, 1999; Jäger et al., 2001; Mann, 2002) stack increases the signal-to-noise ratio significantly and its attributes can be used for further applications like diffraction separation (Dell and Gajewski, 2011), pre-stack data enhancement (Baykulov and Gajewski, 2009), multiple suppression (Dümmong, 2010), time migration (Spinner and Mann, 2007) and normal-incidence-point (NIP) wave tomography (Duveneck, 2004). However the handling of conflicting dips with the CRS operator (Mann, 2001; Höcht et al., 2009; Müller, 2009) is often not reliable and leads to suppression of the less dominant events. Similar to the dip-moveout (DMO) Soleimani et al. (2009a) proposed the common-diffraction-surface (CDS) method, which stacks along all angles, thus fixing the angle and estimating a mixed curvature parameter called R_{CDS}. This approach uses the CRS operator for diffractions which lacks information about either R_{NIP} or R_N depending on the choice of aperture and can not be used for most further CRS attribute based methods. Therefore, I propose a new method to account for conflicting dips which divides the search space into smaller dip cluster and stacks all cluster contributions.

The pragmatic approach (Müller, 1999) is a fast and efficient method to get initial CRS wavefront parameters for the common-reflection-surface (CRS) stack (Hubral, 1983; Müller, 1999; Mann, 2002). The estimated initial set of parameters can be optimized locally afterwards by a multidimensional search. This approach has been used for a decade and delivered decent results in a manageable amount of time. However, it is not well suited for the handling of conflicting dips, since multiple operators are required and the pragmatic approach mostly works for the most dominant event. Common strategies in other scientific fields to solve complex optimization problems are evolutionary and swarm intelligence based algorithms (Kitano, 1990; Morris et al., 1998). This work uses an algorithm of the family of evolutionary algorithms called differential evolution originally introduced by Storn and Price (1997).

In the recent past, four multiparameter stacking approaches have been introduced: multifocusing (MF, Gelchinsky et al., 1999a), the common-reflection-surface (CRS) stack (Jäger et al., 2001), implicit CRS (iCRS, Schwarz et al., 2014b) and non-hyperbolic CRS (nCRS, Fomel and Kazinnik, 2013). These stacking approaches can all be expressed in terms of three kinematic wavefront attributes introduced by Hubral (1983) but differ in their mathematical expression. Comparisons between these methods have been done in the past (e.g., Dell et al., 2013; Schwarz et al., 2015a). However, some promising stacking methods were not included in these previous studies. Dell et al. (2013) compared the CRS variants using a normal-moveout (NMO) velocity guide function to estimate the attributes. In their study conflicting dips, which often are mainly caused by diffractions, are not carefully accounted for. It was shown that double-square-root operators perform better for diffraction events. Due to their comparably low amplitudes diffractions are often masked by stronger primary reflections. The full potential of higher-order CRS-type approximations can therefore not be revealed, when conflicting dips are not properly treated. In addition, although a quantitative comparability is generally difficult to achieve, a comparison of the computational efficiency, thus far, has not been addressed in this context.

Schwarz et al. (2015a) introduced a new parametrization for CRS-type stacking operators in terms of time and slowness shifts. multifocusing, in contrast to all other approaches, utilizes a different mechanism, a time shift, to perturb the moveout, whereas the other methods shift the slowness in order to account for overburden heterogeneity. Schwarz et al. (2015a) also introduced a recipe to translate time shifts into slowness shifts and vice versa, which allows the comparison of all the operators in the same domain. However, in this study the authors used a synthetic model and estimated attributes based on an initial solution obtained by the so called pragmatic approach (Jäger et al., 2001) which can be inaccurate for complex geology. Since in all previous studies, hyperbolic and higher-order CRS expressions including multifocusing were formulated in terms of the two aforementioned mechanisms, they were not compared on common ground, i.e., the gained results are hard to appreciate. In this work, we present an unbiased comparison of the double-square-root operators and conventional hyperbolic CRS for both possible mechanisms consistently, using a global optimization scheme and sophisticated conflicting dip processing on a strongly scattering industrial field data set.

In this thesis I describe the concept of the CDS and extend it to the CRS method. I introduce the general scheme of an evolutionary and genetic algorithm and describe the variation I use in the examples. Finally I compare the conventional simplex based optimization approach with the proposed one. I apply it to a synthetic and a field data set and discuss occurring issues. Additionally I perform a CRS attribute based diffraction separation.
In the following, I will give a brief overview of the structure of this thesis.

Chapter 2 explains conventional and modern seismic stacking methods which are used within the thesis. It introduces the conventional common-midpoint stacking, connects it with multiparameter stacking and the concept of slowness and time shifts. Furthermore, advanced methods are revisited like diffraction separation and prestack data enhancement.

Chapter 3 elaborates on the necessity of optimization methods and their importance in the parameter estimation. I comment on the difference between local and global optimization and introduce the well known genetic algorithm and its variant differential evolution which is used in this thesis.

Chapter 4 reviews existing methods to account for conflicting dips in the CRS framework and develop a new workflow to incorporate conflicting dip processing into the CRS framework while improving the parameter estimation reliably.

Chapter 5 investigates the behaviour of CRS in the presence of data containing only zero and pure noise of Gaussian and uniform distribution. I highlight pitfalls that are of importance when CRS is applied to challenging noisy data.

Chapter 6 shows the application of CRS on an industrial field data set. Furthermore, I compare the different operators available and show improvements in CRS attribute-based methods. It proves the viability of the proposed method which enables new future possibilities.

Chapter 7 proves the necessity of conflicting dip processing in a crystalline environment within the framework of CRS. I compare results of the conventional common-midpoint (CMP) processing with conventional CRS processing and the methodology developed in this thesis and show improvements achieved, which can help to gather more information such as the velocity content.

Chapter 8 concludes the thesis and **Chapter 9** provides an outlook to future possibilities, in particular diffraction imaging and multiple suppression.

Chapter 2.

Seismic stacking

Stacking is a stable and integral part of seismic data processing. It can be done in various stages of the processing sequence. A rough constant velocity brute stack for example can be done in the very beginning with less effort in order to get an idea of the acquired data or in field for quality control. In later stages, after pre-processing, stacking can be performed to increase the quality (signal-to-noise ratio) of the data and provide input for poststack processing like poststack migration methods. It is also possible to use more advanced stacking methods to further increase the signal-to-noise ratio or use estimated attributes for certain applications. A common method is to migrate common-offset or common-shot-gather and sum them up. However, it is also possible to use more advanced multiparameter methods like common-migrated-reflector-element stacking (Dell et al., 2012). In this chapter I give an overview of the most common classical CMP stacking and more advanced multiparameter stacking methods that can be expressed with the same parametrization. Furthermore, I investigate a commonly used efficient method to estimate initial parameters.

2.1. The seismic experiment

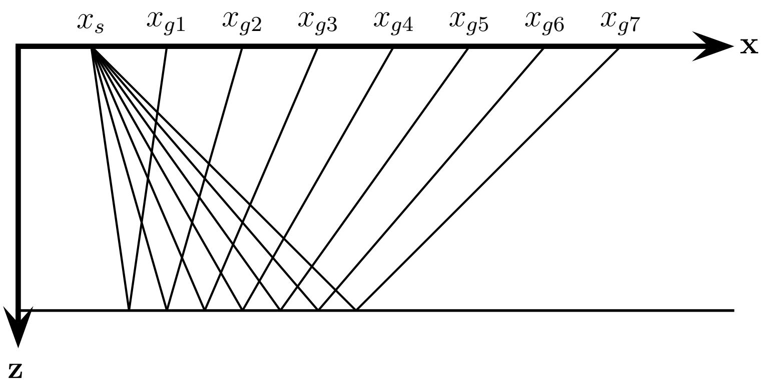

Figure 2.1.: Exemplary layout of a marine data acquisition. Each shot x_s is measured at several receiver x_g leading into a common-shot-gather.

In order to image the subsurface with seismic data, it is necessary to record them with a suitable acquisition. The type of acquisition depends on the target and the environment. In a marine environment, e.g., the traditional method is a ship towing a seismic source like an airgun and a long streamer containing hydrophones. The data is recorded at every hydrophone for a specific recording time, where reflected and scattered wavefields of one source signal are measured. Each shot generates new data for all receivers that are ideally allocated along a straight line. The data has two dimensions, namely the recoding time and the distance of source and receiver called offset. This is known as a common-shot-gather. Modern acquisitions are usually done in three dimensional experiments where receivers are not allocated along a line but on a grid. Rather than a recording time and offset, the data in this case depends on two orthogonal offsets. This translates on larger data and longer processing. Most of the processing steps however are similar. In my thesis I will stick to 2-D data due to the required computational effort. However, The methods can be in principle applied to 3-D data as well.

Common-shot-gather are used in modern migration algorithms. However, traditional processing (before migration) often requires another sorting. Since many shots are acquired and usually a high number of receiver are available it is desirable to sort the data based on the midpoint between the shot and a corresponding receiver. Due to different source and receiver locations with each shot, a common-midpoint (CMP) is illuminated many times. The amount of source and receiver combinations that contribute to a midpoint is called fold. A high fold is often the aim but not always possible for various reasons, like difficult terrain, an urban environment, permissions or economic reasons.

2.2. Common-midpoint stack

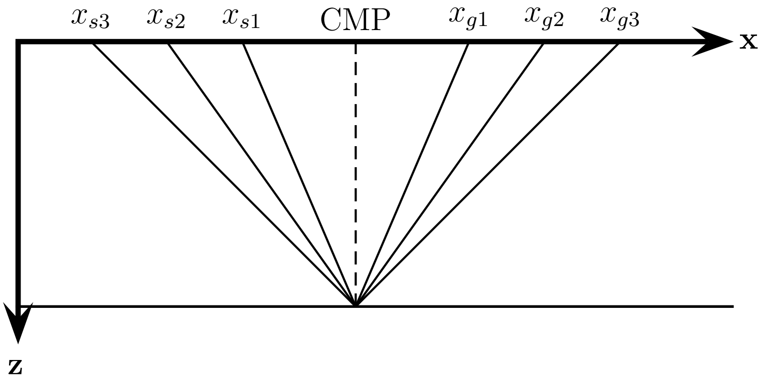

Figure 2.2.: Data sorted into common-midpoint-gather where midpoints of source and receiver locations coincide.

Seismic data can be sorted from common-shot-gather to common-midpoint-gather by a simple rearrangement following

$$m = \frac{x_s + x_g}{2} \quad , \tag{2.1}$$

where m is the common-midpoint, x_s the source and x_g the receiver position. Each resulting midpoint contains as many traces as offsets are available for the specific midpoint. In case of the horizontal reflector the common-midpoint is also the reflection point as can be seen in Figure 2.2. If source and receiver positions coincide, the traveltime of the seismic ray is minimal in isotropic media. With an increasing offset, the traveltime of the ray increases accordingly. In applied seismic this is called moveout. In a homogeneous isotropic medium the traveltime of the ray is hyperbolic

$$t(h, t_0) = \sqrt{\frac{t_0^2}{4} + \frac{2h^2}{V_{NMO}^2}} \quad , \tag{2.2}$$

where t_0 is the zero-offset traveltime, $h = (x_g - x_s)/2$ the half-offset and V_{NMO} the moveout velocity. For a homogeneous isotropic medium with a horizontal reflector V_{NMO} is the actual medium velocity. In field data this assumption is not valid as there are more than one reflector in the subsurface and a reflector is also usually not horizontal. In the common-midpoint stack (Mayne, 1962) the data is summed up along the offset using Equation 2.2 to increase the signal-to-noise ratio, decrease the amount of data and provide a first non-migrated image of the subsurface.

Equation 2.2 is a simple formula that is valid within the hyperbolic limit. In more complicated media, extensions are possible to account for heterogeneity or anisotropy. This will lead to traveltime expressions that differ. Following Fomel and Kazinnik (2013) a more general formulation for the CMP stack S is

$$S(t_0, m_0) = \int P(t(h, t_0), m_0, h) dh \quad . \tag{2.3}$$

The stack of a CMP m_0 is achieved by a summation of the prestack data P along the offset h using an operator $t(h, t_0)$ which can be Equation 2.2 or another one.

The desired fold is not always achievable, as mentioned previously. Furthermore, data in challenging environments like crystalline rocks can be of poor quality where barely anything is visible. To increase the image quality more advanced stacking methods are required.

2.3. Multiparameter stacking

Challenging data where CMP processing does not produce desired results benefit from stacking techniques where the stacking is done in offset and midpoint direction

$$S(t_0, m_0) = \iint P(t(\Delta x_m, h, t_0), m, h) dm dh \quad , \tag{2.4}$$

where $\Delta x_m = m_0 - m$ is the midpoint displacement. Since neighbouring midpoints m are stacked into the midpoint under consideration m_0 as well, a higher amount off traces are summed which results in a better signal-to-noise ratio. However, the traveltime description depends on more parameters compared to classical CMP stacking. Hubral (1983) introduced wavefront attributes that can be used as a parametrization to describe the required traveltime surface $t(\Delta x_m, h, t_0)$ shown in Figure 2.3. Traveltime operators that use these attributes can be classified as common-reflection-surface (CRS) type operators. They differ in their mathematical expressions which stem from the underlying assumptions. While CRS itself is a hyperbolic single square root traveltime expression, the other three introduced in the following sections are double square root operators.

2.3.1. Common-reflection-surface stack

The CRS stack is a multiparameter stacking technique developed by the WIT Consortium group in Karlsruhe, Germany (Müller, 1999; Mann et al., 1999; Jäger

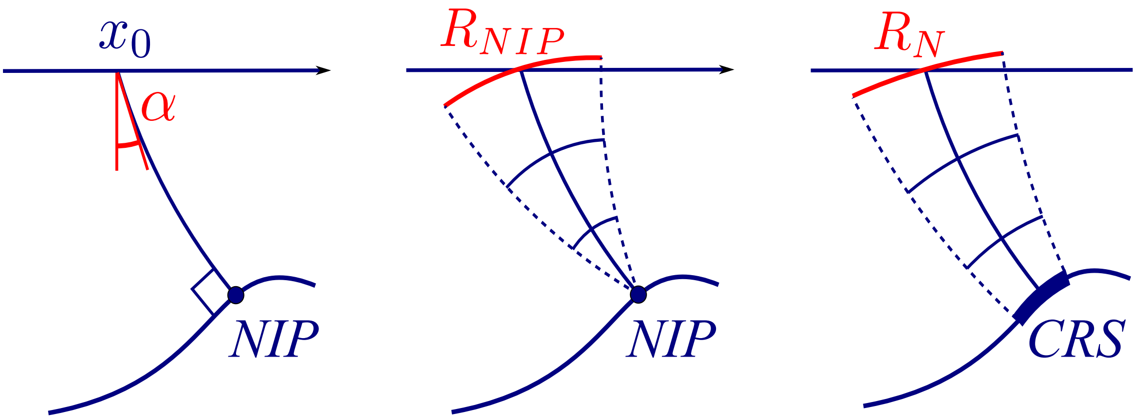

Figure 2.3.: Two hypothetical experiments: The normal-incidence-point wave is shown in the middle with its radius of curvature R_{NIP}. The normal wave with the radius of curvature R_N, is caused by an exploding reflector experiment (right). Both have the angle of emergence α (left).

et al., 2001; Mann, 2002) that considers neighbouring midpoints as well as the offset (see Figure 2.4) while the CMP method uses only offsets. It describes an event in the vicinity of the zero-offset (ZO) sample by a second-order traveltime approximation. Since more traces are stacked, the signal-to-noise ratio is improved significantly.

The CRS operator consists of three wavefront attributes, which are related to two hypothetical one-way experiments as shown in Figure 2.3. The resulting two waves are described by the angle of emergence α of the ZO ray and the corresponding radii of curvature: R_N for the normal (N) wave and R_{NIP} for the normal-incidence-point (NIP) wave (Hubral, 1983). The N wave is generated by an exploding reflector model around the normal-incidence-point. The NIP wave is generated by a point source at the normal-incidence-point for a specific reflector.

The CRS formula in its hyperbolic expression is given by

$$t^2(\Delta x_m, h, t_0) = \left(t_0 + \frac{2\sin\alpha}{v_0}\Delta x_m\right)^2 + \frac{2t_0\cos^2\alpha}{v_0}\left(\frac{\Delta x_m^2}{R_N} + \frac{h^2}{R_{NIP}}\right) \quad . \tag{2.5}$$

The parameter v_0 is the near surface velocity. The red colour indicates the wavefront attributes that are estimated during the fitting process.

2.3.2. Implicit common-reflection-surface stack

The implicit common-reflection-surface (iCRS) stack is a further development of the common-reflection-surface (CRS) stack. In contrast to the conventional CRS

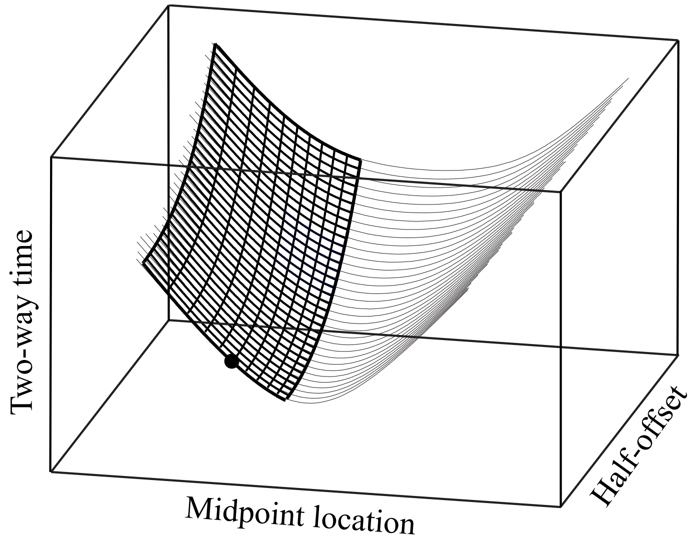

Figure 2.4.: The CRS method stacks along the fat black traveltime surface and assign the value to the point (x_0, t_0). The Figure is modified after Schwarz et al. (2015b).

technique, iCRS is a model based approach that assumes a circular reflector in the subsurface.

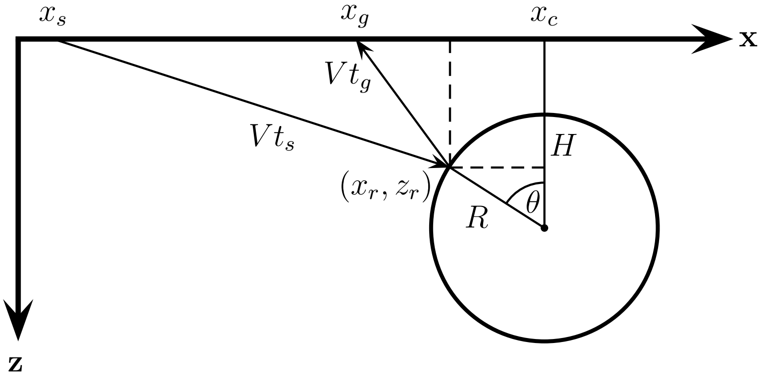

Figure 2.5.: Deviation of the iCRS operator modified after Schwarz (2011).

The iCRS operator is another multiparameter stacking technique derived by a model based approach by the Wave Inversion Technology (WIT) Consortium group in Hamburg, Germany (Schwarz et al., 2014a). It assumes a locally circular reflector as shown in Figure 2.5. It depends on three parameters of the circle (x_c, H and R)

as well as the background velocity of the medium V and reads

$$\begin{aligned} t_s(\Delta x_m, h) &= \frac{1}{V}\sqrt{(\Delta x_m - h - \Delta x_c - R\sin\theta)^2 + (H - R\cos\theta)^2} \quad , \\ t_g(\Delta x_m, h) &= \frac{1}{V}\sqrt{(\Delta x_m + h - \Delta x_c - R\sin\theta)^2 + (H - R\cos\theta)^2} \quad , \\ t(\Delta x_m, h) &= t_s(\Delta x_m, h) + t_g(\Delta x_m, h) \quad , \end{aligned} \tag{2.6}$$

where Δx_m is the midpoint displacement, h the half-offset, θ the reflection point angle on the circle and Δx_c the displacement of the circle. Additionally the reflection angle θ on the circle has to be calculated. It depends on the traveltimes t_s and t_g

$$\tan\theta = \tan\theta_0 + \frac{h}{H}\frac{t_s - t_g}{t_s + t_g} \tag{2.7}$$

and can be solved in an iterative fashion with the first assumption of an zero offset ray, where the dependence on t_s and t_g vanishes

$$\tan\theta_0 = \frac{\Delta x_m - \Delta x_c}{H} \quad . \tag{2.8}$$

Schwarz (2011) showed, that a few iterations are already sufficient. The parameters of the circle can be related to wavefront attributes by

$$\begin{aligned} V_{NMO} &= \sqrt{\frac{2v_0 R_{NIP}}{t_0\cos^2\alpha}} \\ V &= \frac{V_{NMO}}{\sqrt{1 + \frac{V_{NMO}^2}{v_0^2}\sin^2\alpha}} \\ \Delta x_c &= \frac{-R_{NIP}\sin\alpha}{\cos^2\alpha\left(1 + \frac{V_{NMO}^2}{v_0^2}\sin^2\alpha\right)} \\ H &= \frac{v_0 R_{NIP}}{V_{NMO}\cos^2\alpha\left(1 + \frac{V_{NMO}^2}{v_0^2}\sin^2\alpha\right)} \\ R &= \frac{\frac{v_0 R_N}{V_{NMO}\cos^2\alpha} - \frac{V_{NMO}t_0}{2}}{\sqrt{1 + \frac{V_{NMO}^2}{v_0^2}\sin^2\alpha}} \quad . \end{aligned} \tag{2.9}$$

2.3.3. Non-hyperbolic common-reflection-surface stack

Fomel and Kazinnik (2013) introduced another extension of CRS. In contrast to iCRS the non-hyperbolic common-reflection-surface (nCRS) method assumes a hyperbolic reflector since there is no closed form solution for a circular reflector. This requires additional iterations to estimate the reflection point angle θ for the iCRS operator. The nCRS does not need this iterations and therefore saves computation time.

The CRS operator from Equation 2.5 can be formulated as

$$t(\Delta x_m, h, t_0) = \sqrt{f(\Delta x_m, t_0) + b_2 h^2} \quad , \tag{2.10}$$

$$f(\Delta x_m, t_0) = (t_0 + a_1 \Delta x_m)^2 + a_2 \Delta x_m^2 \quad . \tag{2.11}$$

The coefficients a_1, a_2 and b_2 can be related to the wavefront attributes α, R_{NIP} and R_N as

$$\begin{aligned} a_1 &= \frac{2\sin\alpha}{v_0} \\ a_2 &= \frac{2\cos^2\alpha t_0}{v_0 R_N} \\ b_2 &= \frac{2\cos^2\alpha t_0}{v_0 R_{NIP}} \quad . \end{aligned} \tag{2.12}$$

The extension to nCRS

$$t(\Delta x_m, h, t_0) = \sqrt{\frac{f(\Delta x_m, t_0) + ch^2 + \sqrt{F(\Delta x_m - h, t_0) f(\Delta x_m + h, t_0)}}{2}} \quad , \tag{2.13}$$

apart from some prefactors, adds an additional square root which makes it very easy to implement in existing CRS codes. Furthermore, the calculating of the second square root is not as problematic since most quantities can be calculated before.

2.3.4. Multifocusing

Planar multifocusing introduced by Gelchinsky et al. (1999a) and revisited by Landa et al. (2010) attempts to express the traveltime in terms of the traveltime of a central ray and two corrections at the source S and receiver G positions from a paraxial ray. To achieve this, a parameter to focus the NIP and N wave for a planar reflector is required which reads

$$\gamma = \frac{\Delta x_s - \Delta x_g}{\Delta x_s + \Delta x_g + 2\frac{\sin\alpha}{R_{NIP}}\Delta x_s \Delta x_g} \quad , \tag{2.14}$$

where $\Delta x_s = \Delta x_m - h$ and $\Delta x_g = \Delta x_m + h$. It is called focusing parameter, which together with the equations

$$\begin{aligned} t(\Delta x_m, h) = & \frac{1}{v_0}\sqrt{(R^+)^2 + 2R^+\Delta x_s \sin\alpha + (\Delta x_s)^2} \\ & + \frac{1}{v_0}\sqrt{(R^-)^2 + 2R^-\Delta x_g \sin\alpha + (\Delta x_g)^2} \end{aligned} \tag{2.15}$$

$$R^{\pm} = \frac{1 \pm \gamma}{\frac{1}{R_N} \pm \frac{\gamma}{R_{NIP}}} \quad , \tag{2.16}$$

leads to the multifocusing operator. However, multifocusing as presented here and in literature uses a time shift to account for heterogeneity. Therefore, previous comparisons of multifocusing with other CRS type operators as in Tygel et al. (1999), Landa et al. (2010) and Fomel and Kazinnik (2013) are not on common ground. In the next section I explain the difference and introduce a method to transform multifocusing to a slowness shifted operator.

2.3.5. Time shift and slowness shift

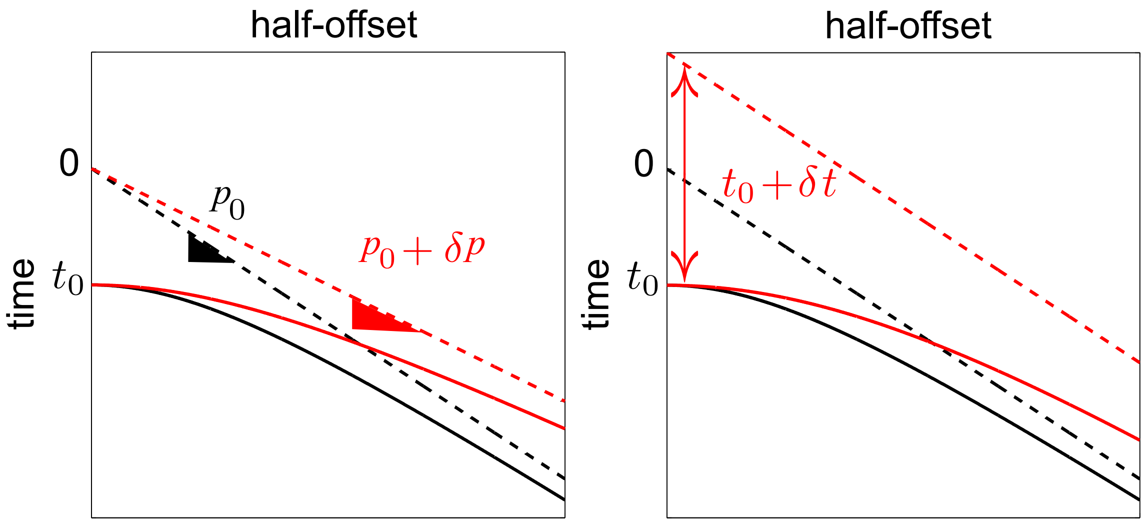

Figure 2.6.: Illustration of the two possible mechanisms to perturb the moveout to account for overburden heterogeneity. The solid line represent the actual unperturbed (black) and perturbed (red) moveout. For the slowness shift, the slope of the moveouts asymptote (meshed) is changed. In case of the time shift, the time of origin of the asymptote is changing. After Walda et al. (2016)

In the recent work of Schwarz et al. (2015a), the authors showed that the multifocusing moveout, despite being parametrized in terms of the same kinematic wavefront attributes, behaves differently from all other approaches when heterogeneity is present. In this study they found, that a time shift is responsible for perturbing the moveout, whereas for all other moveouts mentioned in this thesis, a slowness shift allows to account for velocity changes in the overburden. In Figure 2.6 the conceptual difference between either shifting the time or the slowness is illustrated. Schwarz et al. (2015a) introduced a simple recipe to transform time shifts to slowness shifts and vice versa,

$$p_{shift}^2 = p_{0x}^2 + \frac{t_0}{t_{shift}}(p_0^2 - p_{0x}^2) \quad , \tag{2.17}$$

where $p_{0x} = p_0 \sin\alpha$ is the emergent horizontal slowness, p_0 the near surface slowness, t_0 the zero-offset reference traveltime and $t_{shift} = p_0 2 R_{NIP}$ the shifted zero-offset traveltime. Equation 2.17 connects both parametrizations. The time shift mechanism can be appealingly illustrated in the framework of geometrical optics and since the dip is naturally accounted for, Equation 2.17 can be considered as a generalized osculating equation. This allows to freely choose the desired mechanism to account for heterogeneity. However, this also means each operator introduced in literature has two versions. Four CRS type operators are available in literature, namely CRS (Jäger et al., 2001), multifocusing (MF, Gelchinsky et al., 1999b), implicit CRS (iCRS, Schwarz et al., 2014b) and non-hyperbolic CRS (nCRS) introduced by Fomel and Kazinnik (2013). This means there is a choice of eight CRS type traveltime expressions that can be used in Equation 2.4. In order to evaluate differences in the practical application I apply all operators under the same conditions to a marine industrial field data in chapter 6.5.

2.4. Conventional parameter estimation

At the time the common-reflection-surface method was developed, the computational capacities where lower than today. Therefore, an efficient method to estimate the wavefront attributes was required which lead to a three step search called pragmatic approach by Müller (1999). In the first step a classical CMP stack is performed using $\Delta x_m = 0$

$$t(h, t_0) = \sqrt{\frac{t_0^2}{4} + \frac{2h^2}{V_{NMO}^2}} \quad , \tag{2.18}$$

with

$$V_{NMO} = \sqrt{\frac{2 v_0 R_{NIP}}{t_0 \cos^2\alpha}} = \frac{2 v_0}{q t_0} \quad . \tag{2.19}$$

The moveout equation in this formulation only depends on one parameter q, which contains information about α and R_{NIP}.

The next step assumes a zero offset section, where $h = 0$ under the assumption of a plane wave where $R_N \to \infty$. Under this assumptions the CRS operator reduces to

$$t(\Delta x_m, t_0) = t_0 + \frac{2\sin\alpha}{v_0}\Delta x_m \quad . \tag{2.20}$$

This estimates the angle of emergence α. With Equation 2.19 the second wavefront attribute R_{NIP} can be calculated. In the third and final step the CRS operator for the zero offset case ($h = 0$) is used for an one parameter optimization of R_N

$$t(\Delta x_m, t_0) = \left(t_0 + \frac{2\sin\alpha}{v_0}\Delta x_m\right)^2 + \frac{2\Delta x_m^2 t_0 \cos^2\alpha}{v_0 R_N} \quad . \tag{2.21}$$

While the parameter estimation in this fashion is efficient, it ignores most of the prestack data volume. This does not take advantage of the improved signal-to-noise ration CRS is capable of. Furthermore, strong assumptions are involved like a plane wave. Since modern computers are magnitudes faster than seventeen years ago, I suggest to take advantage of the rich prestack data volume and perform a three parameter simultaneous global optimization described in detail in Chapter 3. The obtained CRS wavefront attributes not only describe the traveltime surface which stacks the data. They contain useful information about the subsurface as well. In the next section I introduce methods that take advantage of those CRS wavefront attributes and are used within this thesis.

2.5. CRS attribute-based methods

The wavefront attributes have a physical meaning and provide a lot of information that can be exploited in different ways. Many CRS attribute-based methods have been developed since CRS was introduced like normal-incidence-point tomography (Duveneck, 2004), multiple suppression (Dümmong, 2010), partial CRS (Baykulov and Gajewski, 2009), diffraction separation (Dell and Gajewski, 2011) and data-driven time migration (Bobsin et al., 2015). In this section I briefly introduce those methods I use within this work.

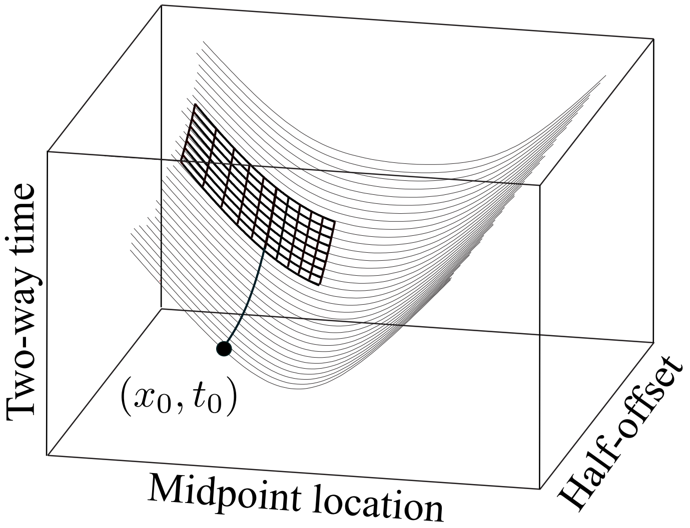

Figure 2.7.: The partial CRS method stacks neighbouring traces (fat black surface) of a specific point on a CMP traveltime curve. It coincides with a subsurface of the CRS surface as shown in Figure 2.4. After Schwarz et al. (2015b).

2.5.1. Partial common-reflection-surface stack

The common-reflection-surface method stacks all offsets into a zero offset section. While this increases the signal-to-noise ratio, CRS wavefront attribute-based applications are limited to poststack processing.

Baykulov and Gajewski (2009) introduced the partial CRS stack to interpolate, regularize and enhance the prestack data using the CRS concept to stack locally at a specific offset as shown in Figure 2.7. The wavefront attributes from the zero-offset CRS stack are used at the considered offset to calculate the CRS surface. However, an additional search for t_0 is required to find the best hyperbola due to the discrete sampling rate. This is achieved by minimizing the deviation between computed and observed traveltime. The t_0 is calculated from the wavefront attributes corresponding to the discrete sample by

$$t_0 = -\frac{h^2 \cos^2\alpha}{v_0 R_{NIP}} + \sqrt{\left(\frac{h^2 \cos^2\alpha}{v_0 R_{NIP}}\right)^2 + t^2(\Delta x_m, h)} \quad . \tag{2.22}$$

This t_0 is used in Equation 2.5. The result is prestack data of better quality which can improve the performance of migration.

2.5.2. Diffraction separation

Dell and Gajewski (2011) introduced a method to separate diffractions from reflections by the wavefront attributes. It is an exponential function that can be used as a binary threshold or to weight contributions. It depends on the two curvature attributes R_{NIP} and R_N and reads

$$W_{f1} = \exp\left(-\left|\frac{R_{NIP} - R_N}{R_{NIP} + R_N}\right|\right) \quad . \tag{2.23}$$

In a recent work by Wissmath (2016) an adjustment was introduced to reduce the value of the exponential function for reflections. This allows to use the function as a threshold like before, or as a simple weight to avoid truncation of events. It reads

$$W_{f2} = \exp\left(-\frac{1}{2}\left|\left(1 - \frac{R_{NIP}}{R_N}\right) + \left(1 - \frac{R_N}{R_{NIP}}\right)\right|\right) \quad . \tag{2.24}$$

Previously, the separation suffered from conflicting dip situations. In such situations, two or more events, like reflections and diffractions, intersect with each other. The required attributes were usually available for the strongest event but not necessarily for weaker events when the conflicting dip handling by Mann (2002) was not successful. I introduce an improved conflicting dip handling in Chapter 4 that improves the separation dramatically. It is also possible to apply the diffraction separation threshold in conjunction with the partial CRS method to generate prestack data which ideally only contains diffractions. This allows to directly pick time migration velocities (Dell and Gajewski, 2011) during velocity analysis. Furthermore, it allows for a reliable diffraction imaging workflow.

2.5.3. Data driven time migration

Based on the Equations 2.9 it is possible to calculate the moveout velocity V_{NMO} from wavefront attributes and apply a dip correction to estimate an effective medium velocity V that represents the root-mean-square velocity V_{RMS} which can be used for time migration (Bobsin et al., 2015). The advantage is a solely data driven estimation of the time migration velocity as a by-product of the CRS stack. This velocity can be used in pre- and poststack time migration similar to a manually derived velocity field. However, the estimated velocity field might lack information when no events are present. A simple and straight forward way to deal with this problem is to take only velocities from samples of high coherence and interpolate resulting gaps. This has the disadvantage of strong smoothing over areas where only low coherent events are present. However, the obtained velocity information can certainly help to build a more refined time migration velocity field Glöckner et al. (2016).

Another problem can occur when different events are fitted as in case of conflicting dip situations. This might lead to a significant difference in velocities of neighbouring samples leading to errors in the migrated section. If information for different dips α are available, it is possible to weight the moveout velocity contributions based on the coherence of the intersecting events:

$$\tilde{V}_{NMO} = \frac{V_{NMO}\tilde{S}}{\tilde{S}_N} \quad . \tag{2.25}$$

The semblance of the corresponding moveout velocity is $\tilde{S}$, while the sum of all semblance contributions is $\tilde{S}_N$. The same dip correction can be applied for V as in Equation 2.9 with the difference of using $\tilde{V}_{NMO}$ instead of V_{NMO}. This is applied to every dip available and finally summed

$$\tilde{V}_{tmig} = \int \tilde{V}_{NMO} \left(1 + \frac{\tilde{V}_{NMO}^2}{v_0^2} \sin^2\alpha\right)^{-\frac{1}{2}} d\alpha \quad . \tag{2.26}$$

This leads to a smooth velocity field where lateral inhomogeneities are still present as can be seen in Figure 9.1.

Independent of the explicit choice of the multiparameter stacking operator, the CRS wavefront attributes need to be determined. Since previous implementations only use a small amount of data redundancy, I propose to use a global optimization scheme with a simultaneous multiparameter search in order to find the best CRS wavefront attributes possible using all available data redundancy. Modern computing facilities provide magnitudes of increased computing power compared to the time those previous implementations were suggested. Thus, a multiparameter global optimization for seismic data is applicable. In the following chapter I introduce the optimization scheme used within the thesis.

Chapter 3.

Optimization

Numerical optimization is necessary, e.g., when no adequate information of the problem at hand or no analytical solutions are available. Furthermore, it is always required when a model needs to be obtained from measurements, e.g. inversion, which is a primary goal in applied seismics, since it is required for depth imaging. In the context of my thesis, I use numerical optimization to fit the CRS traveltime operator to seismic data in order to find suitable CRS wavefront attributes for reflected and scattered events.

In a mathematical description the goal of an optimization is to find the best solution (minimum or maximum) of an objective function $f(x)$. By definition a minimum or maximum is achieved when the first derivative (gradient) of the objective function is zero: $\vec{\nabla} f(x) = 0$. Whether a minimum or maximum is found can be determined by the second order derivative of the objective function. A maximum is achieved for $\vec{\nabla}^2 f(x) < 0$ and a minimum for $\vec{\nabla}^2 f(x) > 0$. Most optimization methods are designed to find a minimum. If a maximum is sought, most of the time the negative objective function $-f(x)$ is minimized. These criteria require a differentiability of the objective function which is not always the case. Fortunately, derivative free algorithms where developed for this case.

Optimization problems are usually formulated to solve a given problem where a priori information might be available and/or certain criteria need to be fulfilled. Examples are physical limitations, to maximize profit, or not exceed a certain amount of cost. In optimization they are formulated as constraints. While physical limitations can be used to constrain the search space of the variables that determine the objective function or the objective function itself, other limitations can guide algorithms into a specific direction or exclude undesired possible solutions. A priori information can be further used to define a starting point. In general, better constraints yield a higher chance to find a good solution fast. If the shape of the objective function or its behaviour is known, specialized algorithms are suited best. If gradients can be computed reliably, Quasi-Newton or conjugate gradient methods are useful. The

Hessian matrix can be used in Newton methods. However, a gradient or Hessian is not always available or very noisy. Unfortunately, the objective function in seismic problems tends to be very noisy, especially in challenging data and in the vicinity of weak events. Therefore, I use an optimization method called differential evolution (DE) that does not rely on derivatives. Instead, it tries to explore the search space based on available information.

3.1. Objective function

In the common-reflection-surface method it is required to search for three attributes. Optimization algorithms try to minimize or maximize a given function. Therefore, the three attributes must be represented by a meaningful mathematical expression that can be compared to the data. In case of the CRS operator, the three attributes are used to estimate a traveltime surface. Since seismic data is band-limited and therefore, contains waveforms, a simple traveltime fit is not sufficient. Taner and Köhler (1969) developed a coherency measurement named semblance (C_S) to estimate the coherent energy along a traveltime curve, or in case of CRS: traveltime surface

$$C_S = \frac{\sum_{i=1}^{M} \left(\sum_{j=1}^{N} A_{ij}^2 \right)}{N \sum_{i=1}^{M} \sum_{j=1}^{N} A_{ij}^2} \quad , \tag{3.1}$$

where N is the number of traces, M the number of samples within the time window and A_{ij} the amplitudes. The width of the time window is called coherence band and should cover the waveform of the source signal. The semblance is one when the energy along the operator is in phase within the time window. This represents a perfect fit. In case no coherent energy along the operator can be found the coherence becomes zero.

The goal of stacking is to sum data along coherent signals to increase the signal-to-noise ratio and reduce the data volume. Therefore, maximizing the semblance delivers a great criterion which an optimization algorithm can use to measure whether a solution is an improvement or not. The function maximized as the optimization criterion is called an objective function and of tremendous importance in optimization. However, depending on initial information, it is not necessary to try every possible solution. With a priori information the range of possible solutions can be constrained. When the room of possible solutions is small, a local optimization is preferable. Otherwise, a more expansive global optimization scheme becomes necessary.

3.2. Local vs. global optimization

While in general, the search space of most optimization problems can be limited and a starting solution can be guessed. The difference between the needs of a local or global optimization method often lies in the accuracy or confidence in these information. If the starting estimation is already quite accurate and the space of possible solutions small, it is sufficient to search the nearest minimum/maximum. Algorithms that achieve this are often referred to as local optimization methods. Global optimization methods are often used if less about the optimization problem is known and/or many local extrema are present, which should be avoided. They can be used as a black box, where no constraints and starting information are provided. Their goal is to provide a solution that is good enough in those cases. Since the amount of possible solutions is higher and the constraints worse than in the local optimization, they are more computational demanding. These demands, can be reduced by better constraints, better starting information and so on, making the transition between local and global optimization fluent. In fact, many optimization methods can be used local or global or even adapt from a global to a local scale like the particle swarm optimization and others. With modern computing facilities becoming more powerful, global and local optimization algorithms are often used together to improve obtained solutions. However, depending on the shape of the objective function different algorithms can perform very differently on various objective functions. The sheer amount of optimization methods available, the continuous excessive research on them and discovery of new optimization algorithms show that there is no perfect method and the choice can be quite challenging. Since in my work, I use field data, the general shape of the objective function is unknown and constraints as well as a priori information heavily depend on the investigated data. Therefore, I choose a global optimization algorithm that does not rely on a specific shape nor differentiability or starting information to be able to estimate good attributes without any knowledge in general. However, if information are available they can be optionally used as constraints.

3.3. Evolutionary algorithms

Evolutionary algorithms (EA) are meta-heuristics that use lower-level heuristics to provide a good solution to a given problem. Heuristics are experience based strategies for problem solving that are able to learn and therefore adapt to a problem. The solution is usually not guaranteed to be optimal but is mostly sufficient for a certain task.

Evolutionary algorithms are inspired by nature, e.g. biological evolution (Eigen, 1973). In contrast to the pragmatic approach evolutionary algorithms use a starting population of potential solutions rather than one initial solution. The Population is usually randomly generated. After the initialization, the fitness (here coherence) of each individual is evaluated. It follows a loop until a certain criterion is fulfilled like number of iterations, calculation time and/or accuracy. Within this loop, the fittest parents are used for reproduction. The reproduction is done by mutation and crossover of parent genes (or chromosomes) to produce the next generation. The fitness of the new generation is evaluated again and a substitution of the old generation with the new generation is performed. There are several ways to do that but the fittest individuals should always be kept to avoid losing the current best solutions and achieve a better convergence. The two EAs presented in this thesis differ in the way the reproduction is performed.

3.3.1. Genetic Algorithm

Since genetic algorithms (GA) are evolutionary algorithms the overall strategy is very similar to other algorithms of this kind. The main differences origin in the way how the selection of parents, the crossover of their genes and mutations are done. For each of them there are various variations suited for different tasks and shapes of the objective function as well as encoding dependent. The encoding defines the way chromosomes, the attributes of the operator, are parametrized. The most common is a binary encoding where the attributes are encoded in a bit string containing ones and zeros. Another method of encoding the attributes is to represent them as real numbers. Janikow and Michalewicz (1991) found that real encoding usually is more stable and converges faster then binary encoding for real number problems.

The most common selection method is the roulette wheel scheme, where the individuals are sorted by their fitness and their probability to be chosen as a parent is determined by their fitness value (Bäck, 1996). Another approach is the rank based selection. The individuals are again sorted but instead of a probability based on their fitness, a probability dependent on their rank is used. This increases the chance of less fit individuals to become parents while the fittest are less likely to become a parent (Baker, 1985). This is used to avoid strong bias in the optimization. For a parallel implementation tournament selection (Goldberg, 1990) is useful. In this method two or three random individuals are chosen where the fittest individual becomes a parent for the new offspring.

The crossover determines how chosen parents pass their genes to the next generation. One can use an addition of the parameters from the parents with a weight w

$$O_i = w \cdot Y_i^1 + (1 - w) \cdot Y_i^2 \quad . \tag{3.2}$$

The parameter O_i is the i-th attribute of the offspring, Y_i^1 the i-th attribute of the first parent and the Y_i^2 the i-th attribute of the second parent. If $w = 1$, the child takes the value of the first parent. In case $w = 0$ the child gets the same value as the second parent. There are various other crossover methods that can be used. However simple arithmetics are easy to implement and work well.

Mutation is often considered to be the main reason (or only reason) why a genetic algorithm converges. The most common form of mutation is a random mutation where a value gets replaced with a new random value. The probability decreases with iterations.

The reason why genetic algorithms work for most problems is still not solved, Holland (1975) introduced the schema theorem. However Grefenstette and Baker (1989) found issues applying the theorem. Mühlenbein (1992) even showed that an evolutionary algorithm solely based on mutations works well for simple tests. Furthermore hybrid approaches (usually genetic algorithms combined with hill-climbing methods) are better suited for optimization (Davis, 1991). However, the building block hypothesis (Goldberg, 1989) is still an easy to grasp explanation.

Independent of the chosen implementations of selection, crossover and mutation it is highly recommended to use elitism. It means passing the best individual(s) to the next generation in order to preserve the already best obtained solution(s) and further improve the convergence. The performance of genetic algorithms can be enhanced by a combination with other optimization methods, especially in the context of CRS (Walda and Gajewski, 2015b). Within the time frame of this work, I tested several optimization methods. The best trade-off between results and performance where achieved by genetic algorithm and differential evolution, which is introduced in the following section.

3.3.2. Differential Evolution

Differential evolution (DE) is a meta-heuristic optimization algorithm that iteratively optimizes an objective function, without any assumptions about the physical problem itself. In my case the objective function is the semblance (Taner and Köhler, 1969). DE was originally introduced by Storn and Price (1997) and can be classified as an evolutionary algorithm. Heuristics do not rely on gradients, specific type of functions or continuity which is beneficial for very complex shapes of the objective function. In practice the algorithm converges more often to the desired result than other optimization schemes, especially when the shape of the objective function is unknown in general.

DE is popular as a modern global optimization technique and is used in a variety of scientific fields (see, e.g. Das and Suganthan (2011)). DE is very similar to the better known genetic algorithm, described in the previous section, since both are EAs. Like all EAs both algorithms use a number of initial solutions. In most cases they are randomly distributed and called starting population in the algorithms. It is also possible to provide previously determined solutions into the starting population, for example neighbouring samples or velocity estimations. In the next step information obtained from the initial solutions is used to generate a new set of trial solutions. Each iteration, which generates new potential solutions, is called generation. The process of creating new generations is done until a satisfying solution is found. DE and GA differ in the way the next generations are generated.

In DE for each candidate solution (or individual) x_i a trial vector u_i (or agent) is generated which only gets into the next generation if its fitness value (i.e., semblance) is better, than the original candidate solution. The trial vector is generated by mutation and crossover. The index i denotes the individual in the population. The mutation of an individual x_i is done by the formula

$$y_j = a_j + F \cdot (b_j - c_j) \quad , \tag{3.3}$$

where a, b and c are randomly selected individuals of the population that are different from each other and x_i. The index j denotes one dimension of the problem, here the number of parameters, and $F \in [0, 2]$ is called the differential weight. The crossover parameter $C_R \in [0, 1]$ is chosen by the user. A random number $r_i \in [0, 1]$ is generated and if $r_i < C_R$ equation 3.3 is applied. The crossover parameter therefore determines the permutation probability of a dimension. To ensure that at each iteration a trial vector different from the candidate solution is tested, at least one randomly determined dimension j is forced to mutate. If the fitness value of the trial vector $f(u_i)$ is higher than the fitness of the former solution $f(x_i)$ the trial vector becomes the new candidate solution, otherwise it is discarded. This process is called reproduction. Figure 3.1 shows an iteration exemplary on the 2-D Rosenbrock function which reads

$$f(x_1, x_2) = 100(x_2 - x_1^2)^2 + (1 - x_1)^2 \quad , \tag{3.4}$$

where x_1 and x_2 are the two dimensions.

DE has three control parameters C_R, F and N_P which is the size of the population. They dramatically influence the computational effort and accuracy. A trend is to adapt them within the process of optimization (Price, 2005; Brest et al., 2006; Liu and Lampinen, 2005; Qin and Suganthan, 2005; Qin et al., 2009). This introduces new parameters and more complexity rather than a simple solution. I decided to stay with the simple standard DE, as described in this section, denoted as *DE/rand/1/bin* in literature. *DE* stands for differential evolution, *rand* how the individual a is

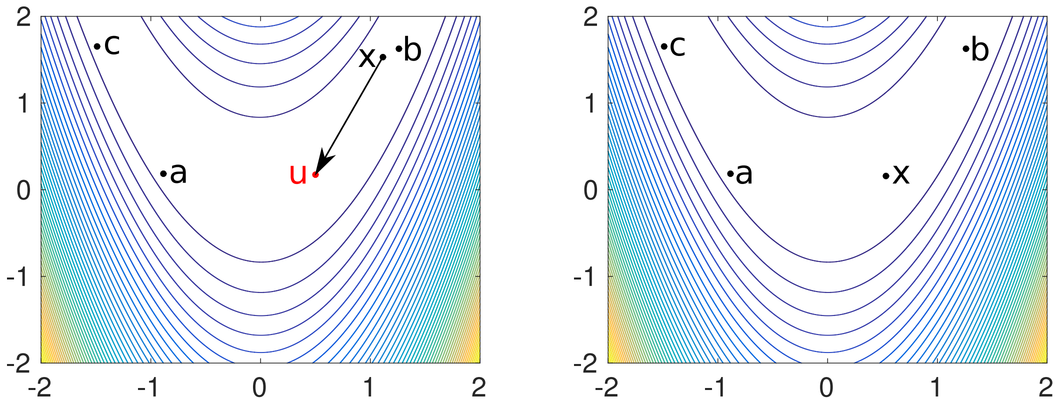

Figure 3.1.: One iteration of the differential evolution algorithm for an individual x. On the left hand side the initial state is shown. A trial solution u is generated by mutating both coordinates using equation 3.3 and a crossover probability of 1. The objective function of the individual $f(x)$ and its trial solution $f(u)$ are compared. In this example the trial solution is better and it becomes the new solution in the next iteration shown on the right hand side.

chosen, *1* is the number of difference vectors considered perturbing x_i and *bin* refers to the crossover operation performed (Das and Suganthan, 2011). There are various guidelines on how to choose the parameters C_R, F and N_P (Storn, 1996; Price, 2005; Liu and Lampinen, 2002). However, I used parameters determined by a meta-optimizer by Pedersen (2010) as they performed best. The choices were $N_P = 20$, $C_R = 0.7455$ and $F = 0.9362$. Barros et al. (2015) applied differential evolution in the context of CRS successfully on land data. However, they did not treat conflicting dips. A stacking velocity model can be used to constrain the search, accelerating and stabilizing the convergence. In case of the marine data, I just fixed lower and upper limits without a previously obtained velocity field. The attributes for the land data were obtained using a velocity guide function that served as a constrain. However, to not rely to much on the picked velocities a variation 20% is allowed (Walda and Gajewski, 2015a).

For consistency reasons, all results shown here were obtained by DE, however, similar results can be achieved with GA as well.

Since optimization algorithms try to find the global maximum, it will search for the most coherent event. However, if events intersect with one another, e.g. diffraction tail and reflection, the weaker event is represented by a local and the stronger by the global maximum. The purpose of global optimization is to not get trapped in such a local maximum. However, in order to image both events in the context of CRS, it is necessary to find both maxima, including the local one. Therefore, I propose a method to find several maxima in the search space to account for conflicting events within the CRS wavefront parameter search and consequently stack in the following chapter.

Chapter 4.

Conflicting dip handling

In multiparameter processing conflicting events become an important issue since they need to be recognized in the data to be imaged. Conflicting events are usually caused by reflections, diffractions, multiples and noise that interfere with one another. As described in the previous chapter, optimization algorithms in principal can only detect the most coherent event. Other, weaker events are usually masked and cannot be recognized as shown for a synthetic data example in Figure 4.1. Strong diffractions, caused by a rough top of salt topography, cut through reflections and other diffractions of the salt body. On the left side, within the layered structure, are diffractions masked by the layered events. This example shows that a strategy to find weaker events, local maxima in the context of optimization, is needed.

In the context of CRS-type operators, several strategies were proposed that all have limitations. The first approach was by Mann (2002) who proposed an extended pragmatic approach that tries to detect conflicting events during the angle scan. However, only a subset of the redundant data is used in this step, which contradicts the idea of CRS and is more susceptible to noise. Additionally, the semblance of intersecting events can be very different which makes it difficult to differentiate between weak events and noise.

A conceptually different approach (target oriented) was propose by Höcht et al. (2009), who interpolate target traces from neighbouring data traces. The CRS method estimates attributes at data traces. The amplitude at the target trace is a weighted sum from neighbouring data traces within the aperture. If two events intersect another at the location of the target trace, they mostly diverge in the vicinity, e.g., a diffraction tail crosses a horizontal reflector. Contributions from data traces in the vicinity of the target trace should contain information from different events. The density of data traces can be sparse which is the major benefit of this method. However, this interpolation only works for the amplitude, not for the CRS wavefront attributes.

Soleimani et al. (2009a) proposed to simply estimate the CRS operator for every angle and stack each contribution. This is a brute-force method which is expansive. To compensate for that, the authors use the CRS operator for the diffraction case and fix the angle during the parameter estimation. This reduces the required parameter from three to one but has limitations. The operator leads to a poor fit for reflections and poorly estimated CRS parameters since the angle is fixed.
In this chapter I review operator oriented methods by Mann (2002) and Soleimani et al. (2009a) and develop a new approach and compare their performance on a complex synthetic data set.

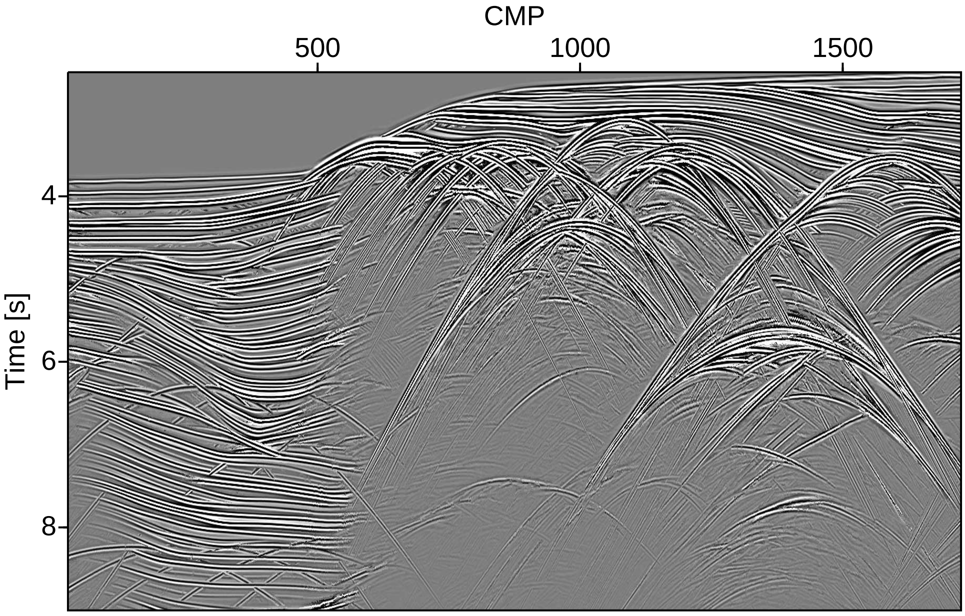

Figure 4.1.: Conventional CRS stack the synthetic Sigsbee 2A data. Only the most coherent event is visible.

4.1. Extended pragmatic approach

In the second step of the previously described pragmatic approach (Chapter 2.4) the angle of emergence α is estimated from the zero offset geometry using a plane wave assumption. An investigation of the objective function by Mann (2002) showed, that several additional local maxima can be observed besides the global maximum, if several events intersect. The authors therefore proposed to search for these maxima to determine multiple CRS operators. The missing attributes are determined based on the found angles. Thus, all found events during the angle search are treated separately and describe a different event. Since operators for different events are available, they can be treated during stacking and other CRS attribute-based methods. However, since only zero offsets are taken into account and a plane wave assumption is used, the approach is not stable in practical applications. Furthermore, this approach relies on the three step search strategy of the pragmatic approach and cannot be used in a simultaneous parameter estimation using the full data redundancy CRS offers.

4.2. Common-diffraction-surface stack

Soleimani et al. (2009a) suggested to stack along all possible angles. This has the advantage that every event which does not come from the same direction and is recorded at the same time will be recognized. This makes it in principle a very stable approach. However, considering every angle is impossible since it would require infinite dense sampling. In practice a predefined grid is required. Depending on the density of the grid, a high amount of operators needs to be determine, which results in a high computational cost. If the grid is too coarse, the wavefront attributes will become inaccurate.

Due to the high computational cost, Soleimani et al. (2009a) suggest to use the CRS operator for the diffraction case where two wavefront attributes become equal ($R_{NIP} = R_N$) and reads

$$t^2(\alpha, x_m, h) = \left(t_0 + \frac{2\sin\alpha}{v_0}\Delta x_m\right)^2 + \frac{2t_0\cos^2\alpha}{v_0 R_{NIP}}\left(\Delta x_m^2 + h^2\right). \tag{4.1}$$

Since the angle α is fixed, only an one parameter search is required. Depending on the size of the aperture, the estimated attribute might take either the value of R_{NIP} or R_N. Furthermore, the approximation is not valid for reflections which leads to a poor semblance shown in chapter 4.4. This makes its usage for further CRS attribute-based methods like partial CRS (Baykulov and Gajewski, 2009) unreliable. Therefore, the full CRS operator is preferable but more expansive. However, due to the fixed angle, inaccuracies are represented in the estimated curvatures and thus leading to undesired behaviour shown in chapter 6.1. In the following section, I introduce a new method to account for conflicting dips that takes advantage of advanced optimization techniques and the full data redundancy of CRS to avoid such problems.

4.3. Angle domain decomposition

Instead of one attribute for the CMP case the Common-reflection-surface stack requires to determine three wavefront attributes. This is a more expansive search, however, there are also exploitable advantages. Since the wavefront attributes can be physically interpreted, they contain useful information. Figure 4.2 shows the α-R_{NIP} plane for a constant R_N. The attributes α and R_{NIP} can be related to the classical moveout by Equation 2.9. Three events can be observed which have a similar R_{NIP} value but different dip angles which also means different moveout velocities. In conventional CMP processing however, only the moveout velocity of the event with the highest semblance would be considered, which is a reflection in this example. The reflection event is clipped for the purpose of the other two events. These are diffraction tails that intersect with the reflection. Since they differ in their dip angle a proper choice of three smaller cubes would allow to find all three events with three individual searches.

I take advantage of this by a discretization of the α space with varying discretization steps. In each of the α intervals all wavefront attributes are searched using a global optimization scheme called differential evolution. The search algorithm was successfully applied recently by Barros et al. (2015). They achieved significant improvements in their case study. The partitioning of the parameter cube into smaller ones reduces the search space and increases the performance of the optimization. Furthermore, if the discretization is chosen properly, intersecting events are recognized in different sub-cubes. This enables many possibilities for quality-control and filtering. Since it is not a priori known at which dip angles α an event is located there is no general choice of interval possible. However, since most intersecting events are either diffractions and reflections or multiples and reflections, a denser discretization is required at smaller dips while the grid can become coarse for higher dips since the chance of intersecting events with a similar high dip angle is rather small.

Each dip range creates their own attribute sections and stack. Therefore, they can be used in further CRS attribute based methods like prestack data enhancement (Baykulov and Gajewski, 2009), diffraction separation (Dell and Gajewski, 2011) or wavefront tomography (Duveneck, 2004) allowing for conflicting dip treatment in these applications as well. Furthermore, the user can conveniently choose in the decomposed sections what to stack or where to apply masks and thus filter unwanted energy like noise and artefacts or use only specific information, depending on the task. This is possible since every dip cluster creates their own attributes.

In the next section, I verify the proposed method on a complex synthetic data set and compare it to previous methods.

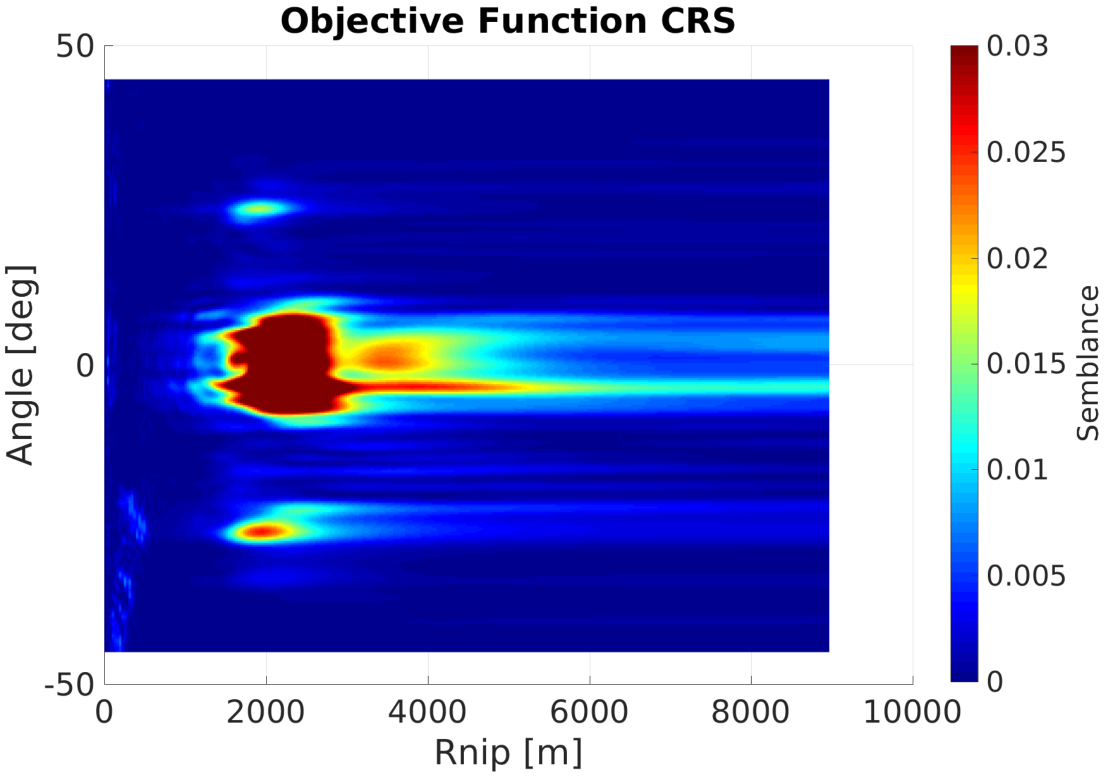

Figure 4.2.: Slice of the 3-D search space with a constant R_N. The colour indicates the semblance value of the attribute triplet.

4.4. Synthetic data example

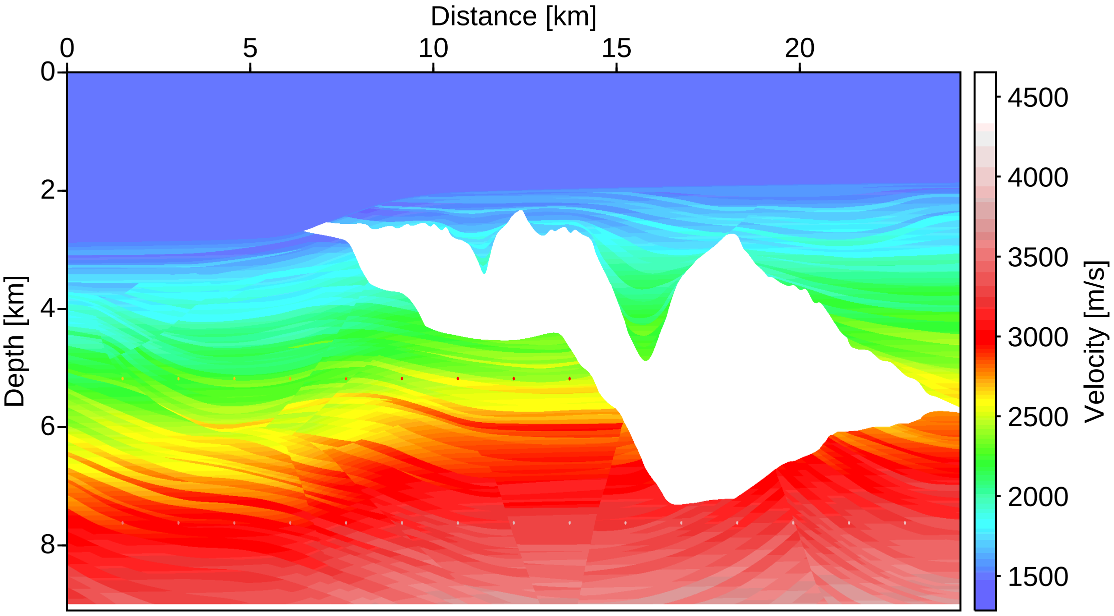

Figure 4.3.: Sigsbee 2A data set representing a geological setting of the Gulf of Mexico. The model contains a large salt body displayed by a white colour due to high velocities.

In order to validate the proposed approach I compare previous existing conflicting dip methods with the developed one on a synthetic data set. The data is provided by the Subsalt Multiples Attenuation And Reduction Team (SMAART) Joint Venture consisting of BHP Billiton, BP and Chevron Texaco and represents a geological setting in the Gulf of Mexico shown in Figure 4.3. The model contains a large salt body with a rough surface causing lots of diffractions intersecting with reflection events. This feature makes it suitable for the purpose of conflicting dip treatment during the CRS workflow. The used processing parameters and apertures are listed in Table 4.1.

The first approach to handle conflicting dips was introduced by Mann (2002) and is shown in Figure 4.4. While conflicting events are mostly imaged in the layered part on the left hand side, diffractions caused by the top of salt cut through reflections which are hidden beneath. In general events of similar amplitude are mostly imaged while conflicting events of differing amplitudes are barely imaged correctly.

Figure 4.5 shows the approach by Soleimani et al. (2009a), where the CRS operator for the diffraction case ($R_{NIP} = R_N$) was used. Conflicting events are imaged very well even those stemming from stair stepping effects of the velocity model during the modelling process. The stack shows, that this method is very well suited

General parameters	
Dominant frequency	20 Hz
Coherence measurement	Semblance
Coherence time window	56 ms
Velocity constraints	
Near surface velocity	1500 m/s
Lower moveout velocity constraints	1400 m/s
Upper moveout velocity constraints	6000 m/s
Search apertures	
Minimum midpoint aperture	300 m at 2 s
Maximum midpoint aperture	500 m at 11 s
Minimum offset aperture	750 m at 2 s
Maximum offset aperture	3000 m at 11 s
Conflicting dip handling	
Number of dip intervals	17
Dip intervals in °	[-90,-45], [-45,-30], [-30,-20], [-20, -12.5], [-12.5,-7.5], [-7.5,-3], [-3,3], [3, 7.5] ,[7.5,12.5], [12.5,20], [20,30], [30,45], [45,90]
Global optimization parameters	
Algorithm	Differential evolution
Number of individuals	20
Crossover probability	74.55 %
Differential weight	0.9362
Minimum number of iterations	30
Maximum number of iterations	200
Number of allowed stagnated iterations	10
Local optimization parameters	
Lower coherence threshold	1.00 at 0 s
Upper coherence threshold	1.00 at 10 s
Maximum Number of iterations	100
Minimum deviation required	10^{-5}
Transformation radius of R_N	100 m
Initial variation of emergence angle	2 °
Initial variation of R_{NIP}	3 %
Initial variation of R_N	4 °

Table 4.1.: Search parameters used for the Sigsbee 2A data set. A local optimization was not performed. Stacking and search parameters are identical.

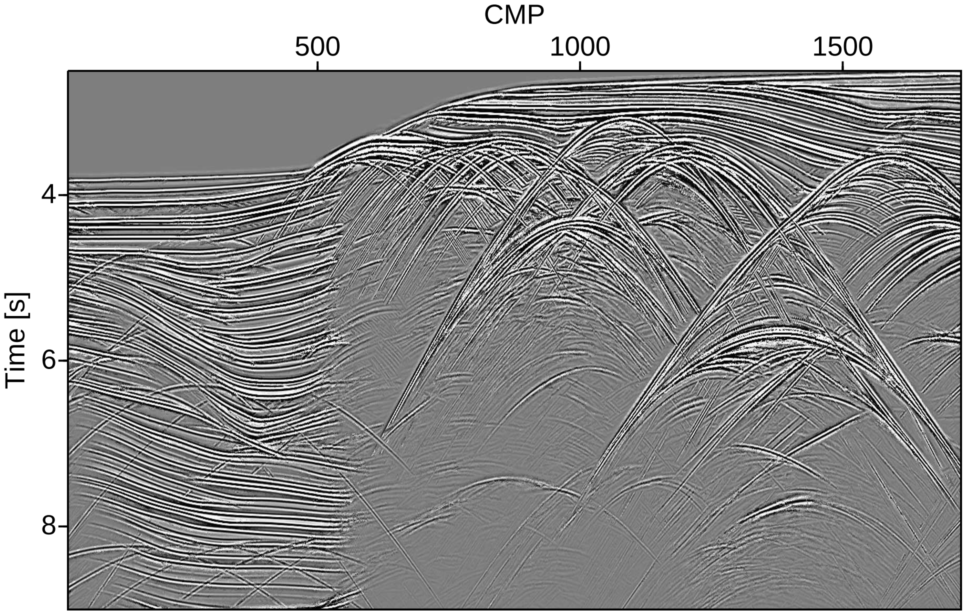

Figure 4.4.: CRS stack of the Sigsbee 2A data using the extended pragmatic approach by Mann (2002).

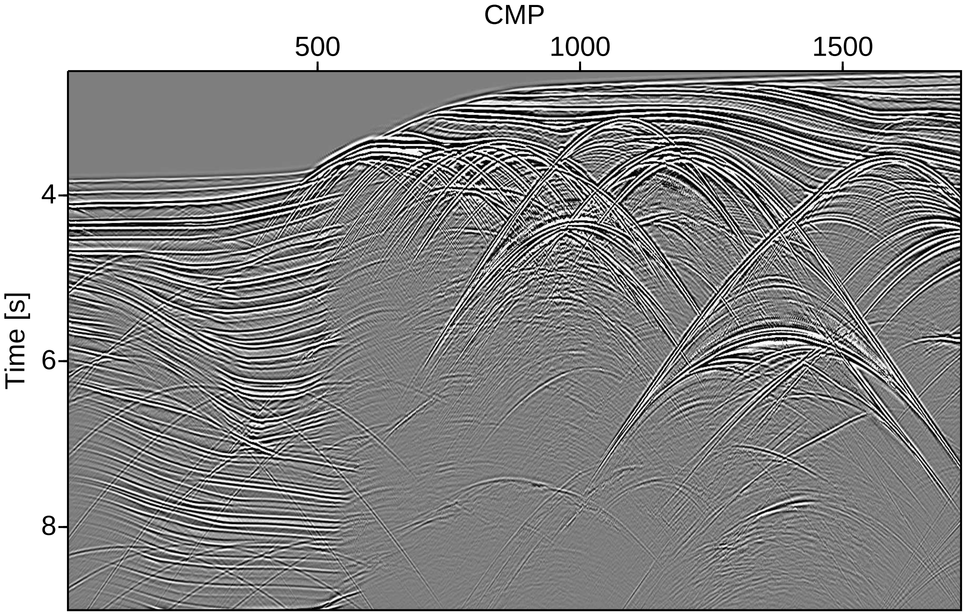

Figure 4.5.: CRS stack of the Sigsbee 2A data using the CDS concept by Soleimani et al. (2009a) on the full CRS operator.

to image conflicting dip situations. However, drawbacks are the high amount of operators needed and the limited accuracy of the estimated parameters due to the fixed emergence angle. In the example I used 121 dips with a spacing of 1° from -60° to +60° which requires 121 operators to be determined per sample. This is not necessary with the suggested angle decomposition approach which requires less operators but achieves a higher accuracy since the wavefront attribute α is not fixed.

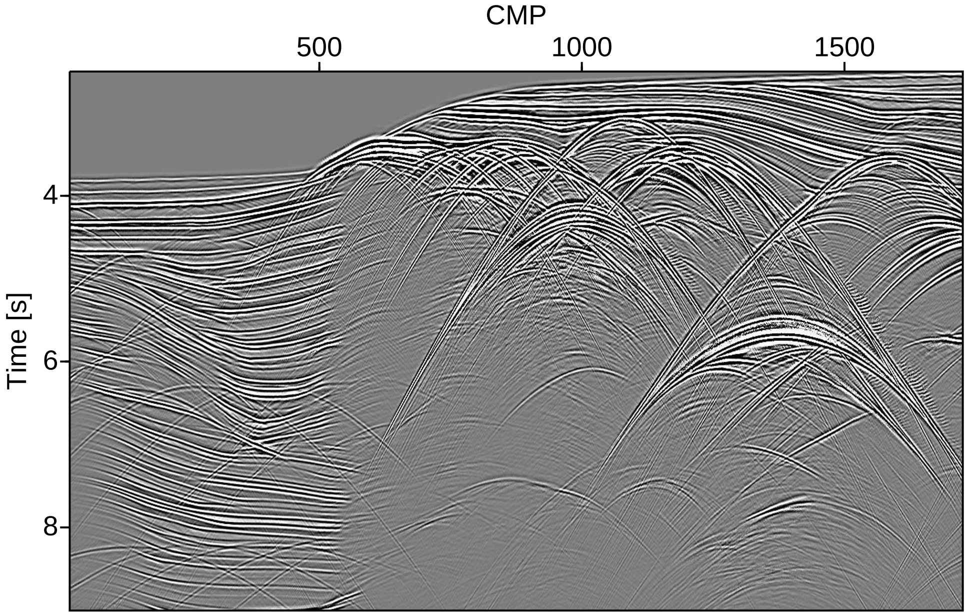

Figure 4.6.: CRS stack of the Sigsbee 2A data using the proposed angle decomposition.

Figure 4.6 shows the stack of the Sigsbee 2A data using the proposed method. Conflicting dips are imaged correctly similar to the approach by Soleimani et al. (2009a). However, the quality of the stack is much better due to the better parameter estimation of the wavefront attributes. This can be seen especially at events from the salt body, which are mainly diffractions. The events are more consistent and diffraction tails are imaged much better. Furthermore, in this example I used nine dip intervals which is far less than previously. This allows a more advanced optimization technique due to a much lower computational cost.

The stacks show the improvements achieved by more advanced techniques to image conflicting dips from the extended approach over the CDS up to the proposed method. However, the stack is not necessarily the best method to evaluate the improvements. A better criterion is the semblance since this is the objective function in the optimization process. This means, a better semblance is equivalent to a better fitted operator. Since it is very difficult to compare the semblance for every event found at every sample in a fair way for all presented methods, I will compare the highest semblance found at every sample, as it should be, in principal, the same for all methods.

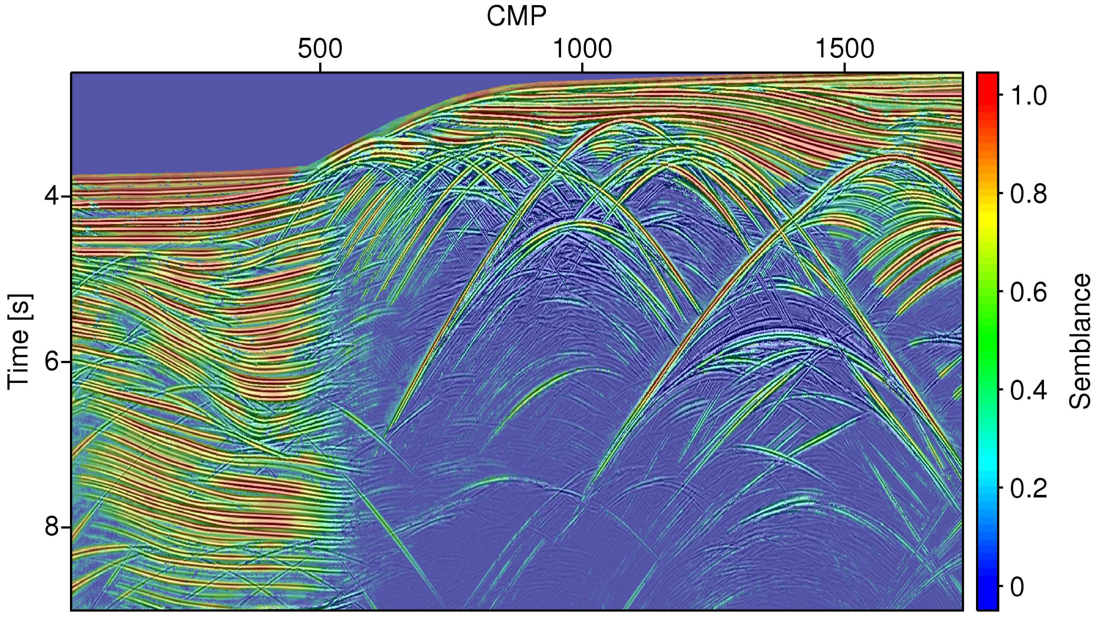

Figure 4.7.: Semblance overlay of the CRS stack using the extended pragmatic approach by Mann (2002).

The extended pragmatic approach shows a high semblance for reflections and top of salt diffractions. This means most parts of the data are estimated correctly. However, the section is noisy indicating many samples where no proper operator could be found. This shows evidence that a better optimization scheme is required. The problem is, the conflicting dip handling cannot benefit from a better optimization scheme since it relies on the initial three step search strategy to recognize conflicting dips.

The semblance section of the most coherent event obtained by the method of Soleimani et al. (2009a) is shown in Figure 4.8. Since the diffraction operator (Equation 4.1) is used, reflections are fitted poorly with a low semblance compared to Figure 4.7. However, for diffractions the semblance is slightly improved. The poor semblance of reflections indicates a poor wavefront attribute estimation which will not provide good results in further attribute-based methods.

Figure 4.9 shows the semblance of the proposed angle decomposition method. The semblance has similar high values as for the extended pragmatic approach but is less noisy. Since the method encourages a better optimization technique than the extended pragmatic approach, events are fitted better at challenging areas like events stemming from the salt body and diffraction tails. This indicates that the wavefront

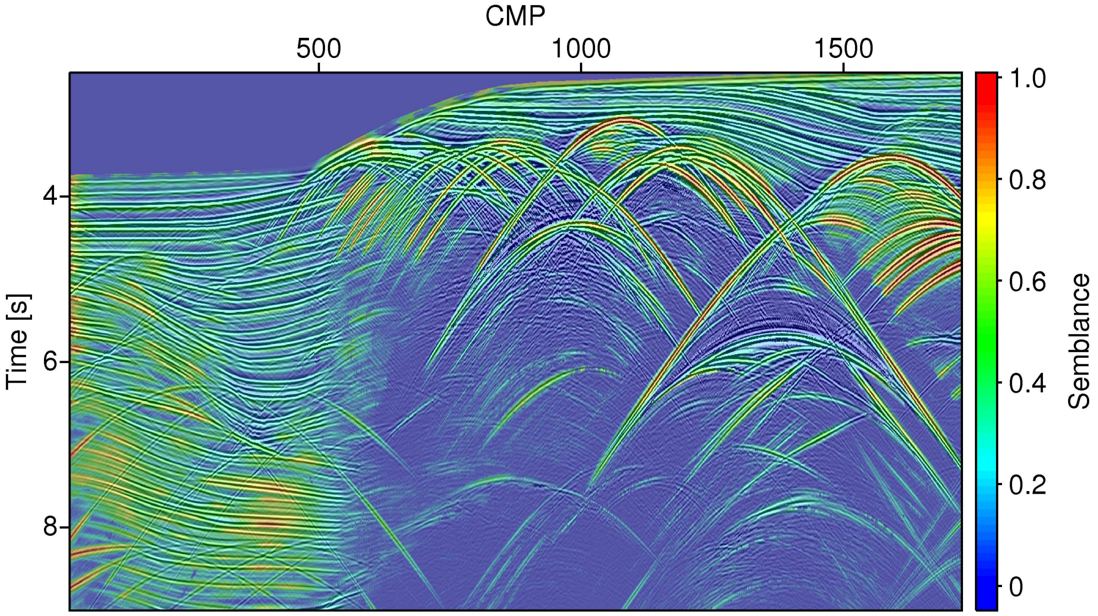

Figure 4.8.: Semblance overlay of the CRS stack using the CDS method by Soleimani et al. (2009a).

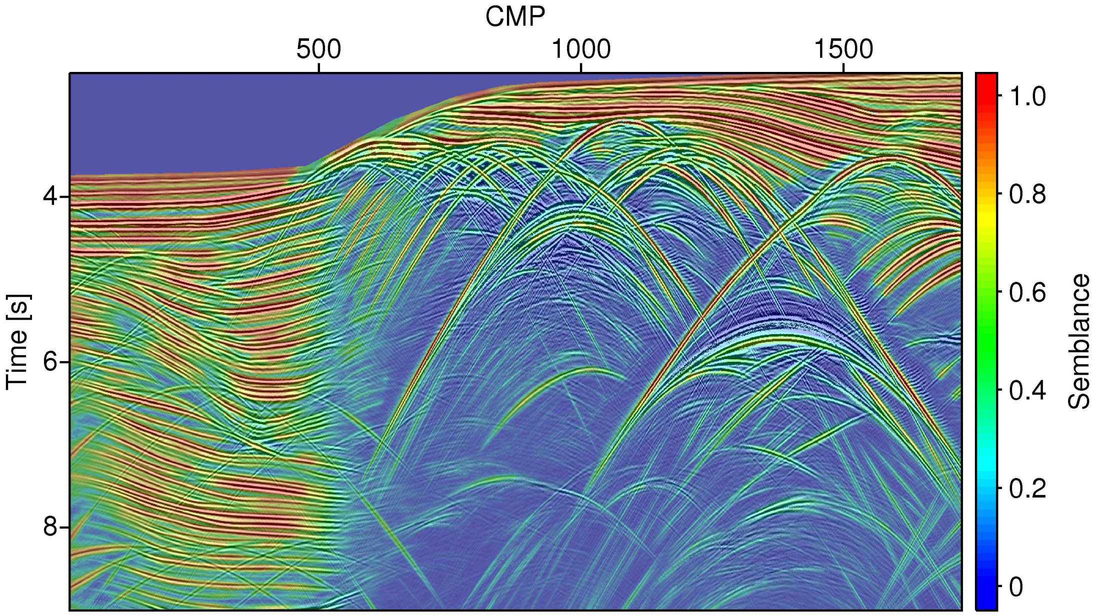

Figure 4.9.: Semblance overlay of the CRS stack using the proposed angle decomposition.

attributes are continuous and of high quality and can be used reliably in further methods as diffraction separation or partial CRS.

Since in the angle decomposition CRS all contributions are available as individual sections as well, more information become available. A directly available information is the dip of the individual events. Figure 4.10 shows contributions from a dip range of [-22.5°,-11.25°], Figure 4.11 from dip ranges of [-5.625°,5.625°] and Figure 4.12 from dip ranges [11.25°,22.5°]. In the dip range around 0° mostly horizontal layering and diffraction apexes are visible. In the other dip ranges diffraction flanks are the most dominant events, even at locations where diffractions and reflections overlap. Since reflections and diffractions are decomposed in different sections the stack contains both information.

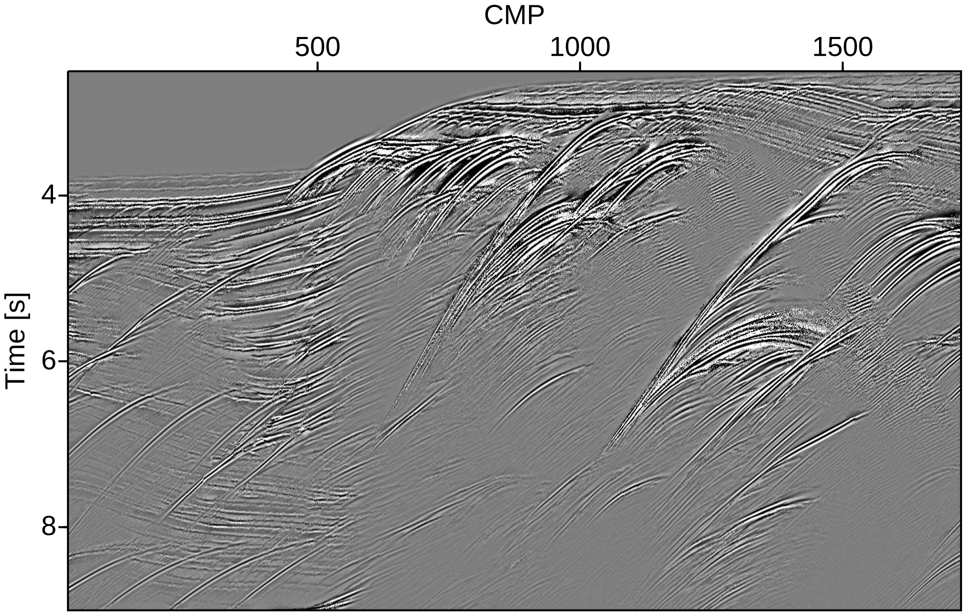

Figure 4.10.: CRS stack of the Sigsbee 2A data using a single decomposed dip range of [-22.5°,-11.25°].

The synthetic data example is free of noise which is not the case for field data. To understand the behaviour of CRS-type operators in the presence of noise, the next chapter investigates pitfalls and challenges of CRS-type operators in the presence of noise.

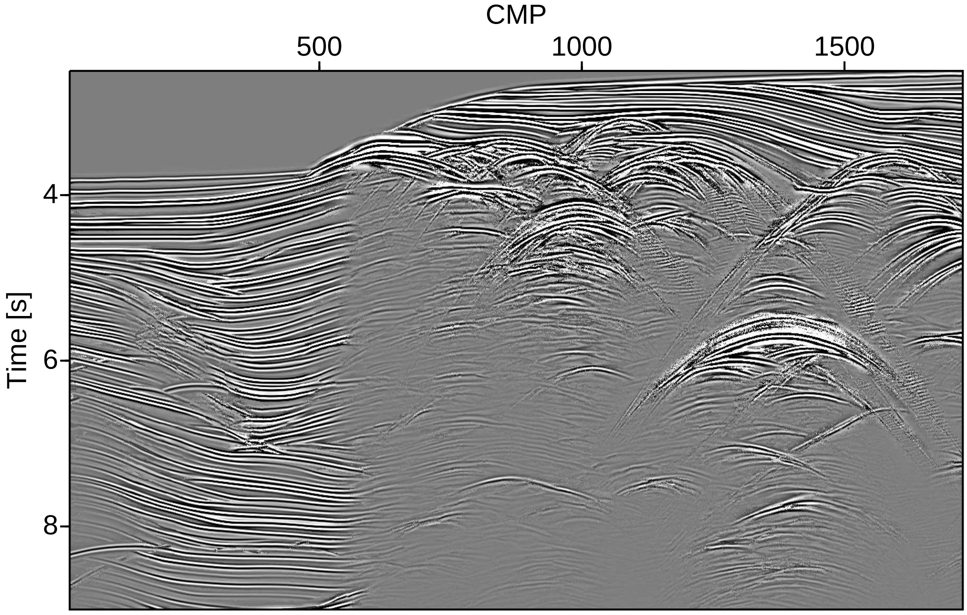

Figure 4.11.: CRS stack of the Sigsbee 2A data using a single decomposed dip range of [-5.625°,5.625°].

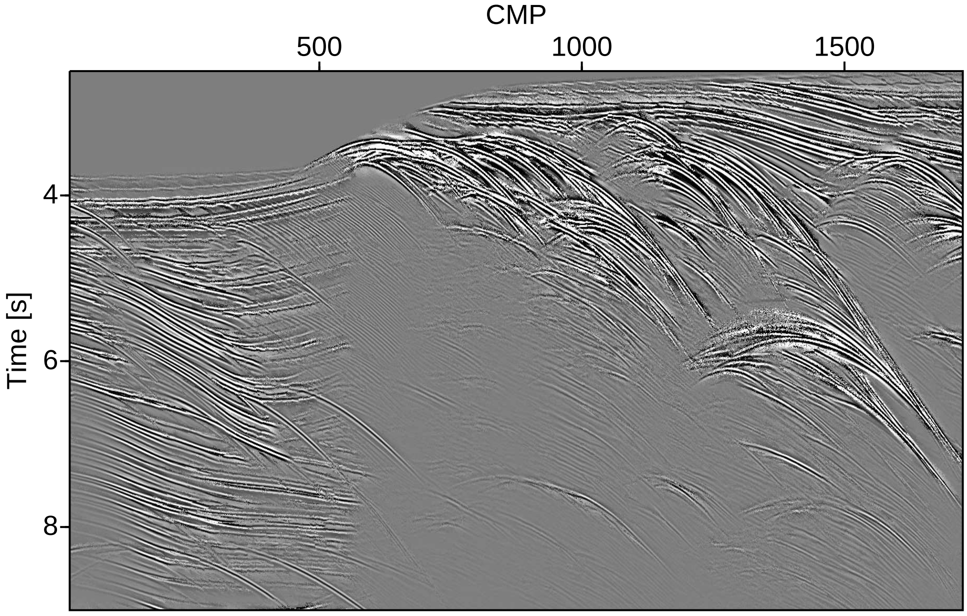

Figure 4.12.: CRS stack of the Sigsbee 2A data using a single decomposed dip range of [11.25°,22.5°].

Chapter 5.

CRS in the presence of noise

Depending on the environment the data is acquired, noise becomes an important aspect of the seismic processing. Since the land data examples in chapter 7 are acquired in a crystalline environment the noise level is very high. In order to appropriately validate, if I observe signal or noise it is necessary to understand how the used operator behaves in the presence of noise. Therefore, I test three cases and apply a CRS-type operator to those to evaluate possible pitfalls. The first pre-stack data contains only zeros, the second uniformly distributed normalized noise and the third Gaussian (normal) distributed normalized noise. The Gaussian probability distribution is given by

$$p_n(x) = \frac{1}{\sigma\sqrt{2\pi}} \exp\left(-\frac{(X-\mu)^2}{2\sigma^2}\right), \tag{5.1}$$

where X is the random variable, μ the mean value and σ the standard deviation. I chose the standard normal distribution where $\mu = 0$ and $\sigma = 1$. The CRS attribute search and stack was obtained using the processing parameters shown in Table 5.1.

5.1. Zero data

In order to validate unexpected bias of the parameter estimation and wavefront attributes in general, I apply the developed CRS workflow without conflicting dip processing on pre-stack data containing only zeros. In this case I expect the CRS parameters (Figure 5.1) to contain only noise and no bias or any kind of pattern. The α section in Figure 5.1(a) indeed seems noisy where no pattern is visible which is confirmed by the histogram in Figure 5.1(b) where an uniformly distributed angle besides boundary effects can be seen. However, the R_{NIP} parameter in Figure 5.1(c) shows a gradient which is related to the initial choice of the near surface velocity that CRS requires. Investigations from Guntern (2016) show, that the choice of the near

General parameters	
Dominant frequency	30 Hz
Coherence measurement	Semblance
Coherence time window	20 ms

Velocity constraints	
Near surface velocity	2000 m/s
Lower moveout velocity constraints	1400 m/s
Upper moveout velocity constraints	4000 m/s

Search apertures	
Minimum midpoint aperture	500 m at 0 s
Maximum midpoint aperture	500 m at 4 s
Minimum offset aperture	2000 m at 0 s
Maximum offset aperture	2000 m at 4 s

Conflicting dip handling	
Number of dip intervals	1
Dip intervals in °	[-90,90]

Global optimization parameters	
Algorithm	Differential evolution
Number of individuals	20
Crossover probability	74.55 %
Differential weight	0.9362
Minimum number of iterations	30
Maximum number of iterations	200
Number of allowed stagnated iterations	10

Local optimization parameters	
Lower coherence threshold	0.01 at 0 s
Upper coherence threshold	0.01 at 4 s
Maximum Number of iterations	100
Minimum deviation required	10^{-5}
Transformation radius of R_N	100 m
Initial variation of emergence angle	2 °
Initial variation of R_{NIP}	3 %
Initial variation of R_N	4 °

Table 5.1.: Processing parameters for all noise data sets. In these cases, the stacking apertures were the same as the search apertures.

surface velocity can have significant influence on the estimated parameters which is corresponding with this observation. For this test I chose a near surface velocity of 2000 m/s. The inverse of the R_N parameter represents normal distributed noise similarly to the α section.

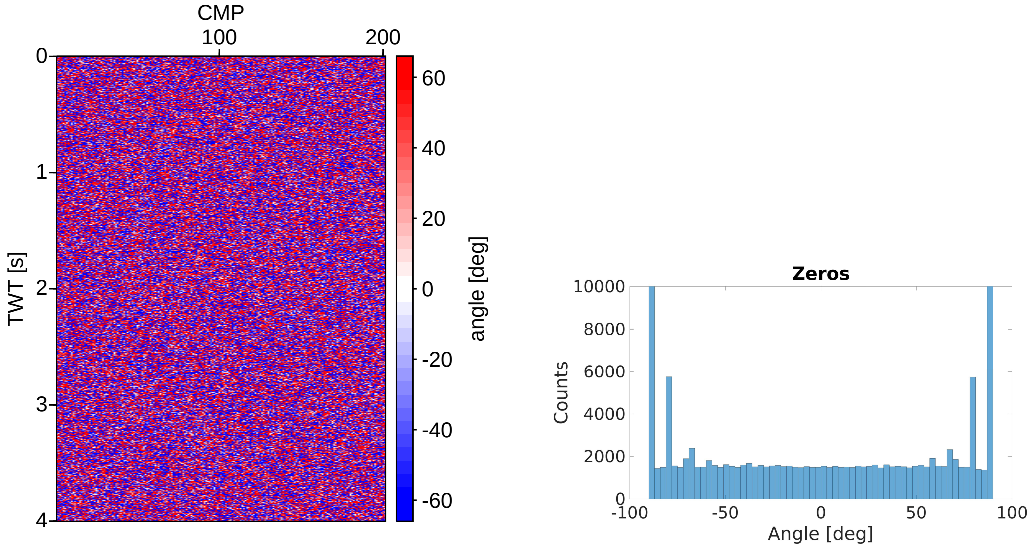

(a) α

(b) Histogram of α

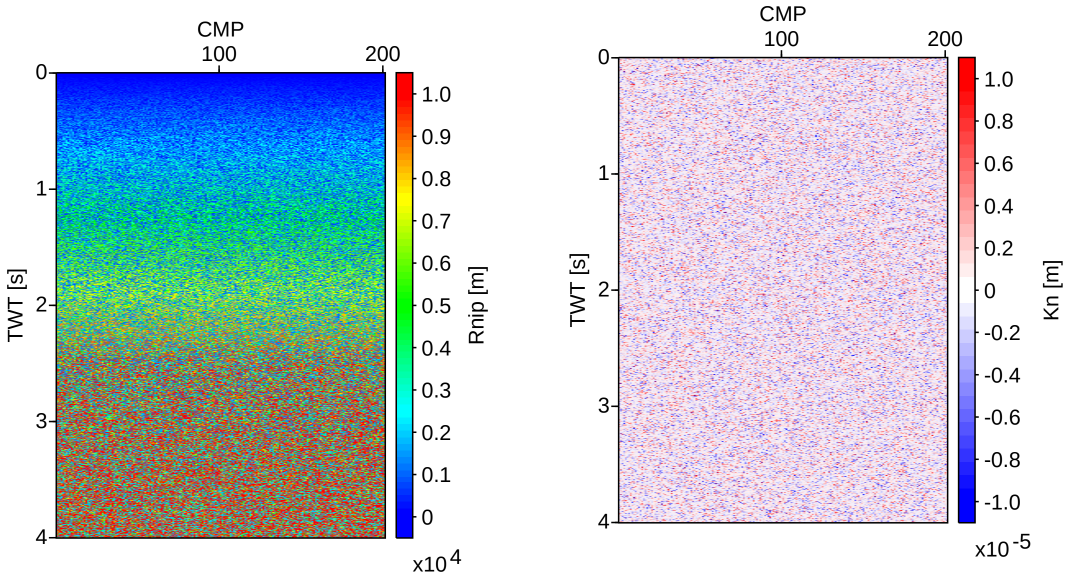

(c) R_{NIP}

(d) $K_N = 1/R_N$

Figure 5.1.: Wavefront attributes and histogram of data containing purely zeros.

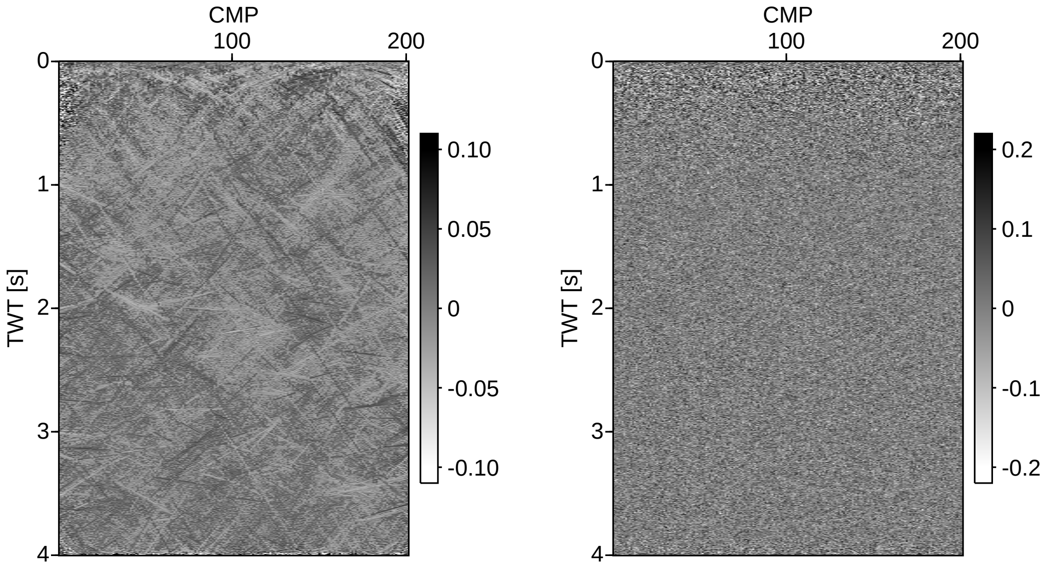

(a) CRS stack on uniform noise

(b) CMP stack on uniform noise

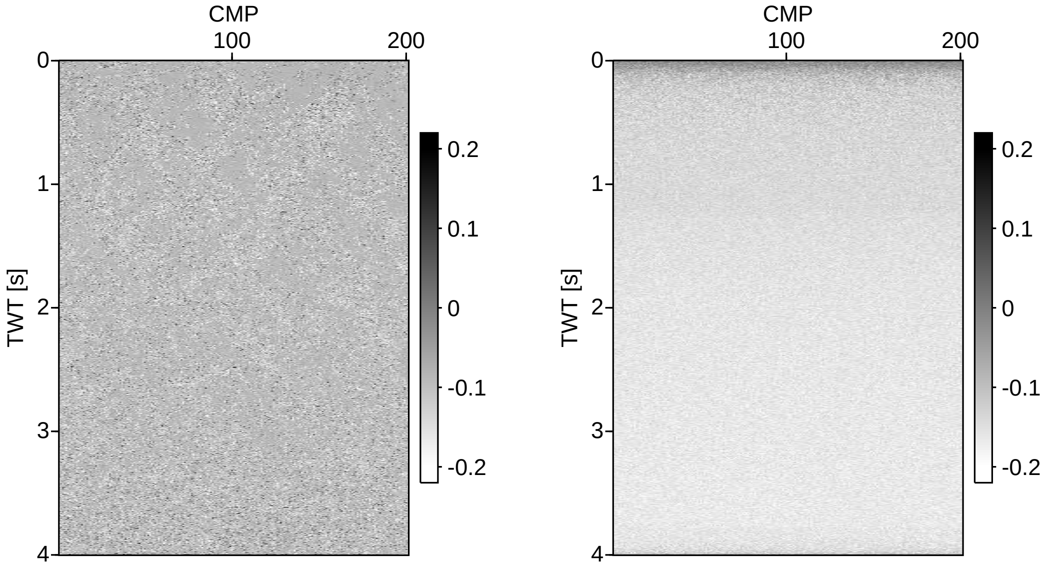

(c) CRS stack on Gaussian noise

(d) CMP stack on Gaussian noise

Figure 5.2.: CRS (Figure (a) and (c)) and CMP stack (Figure (b) and (d)) of data containing uniform and Gaussian noise.

5.2. Noise

I demonstrated in the previous section that at least the angle section of α and the Radius of the normal wave R_N show no initial bias. In field applications however, the data does not contain zeros but rather signals and noise. Therefore, seismic data usually does not contain zeros. I investigate the behaviour of the CRS method on data of uniformly and Gaussian distributed noise to learn which arbitrary patterns can be generated by the application of CRS in presence of strong noise.

Unfortunately the CRS method shows clearly visible coherent patterns in the stack (Figure 5.2(a)) of uniformly distributed noise compared to the CMP stack in Figure 5.2(b). In case of Gaussian noise the coherent patterns are hidden beneath a bias towards a non zero value for the CRS stack (Figure 5.2(c)). However, differences to the CMP stack (Figure 5.2(d)) are still visible.

The observed patterns become more apparent in the semblance in Figure 5.3. Especially in case of Gaussian noise (Figure 5.3(b)) I observe preferred directions. This indicates that coherent noise can be hidden in the CRS stack while still having strong impact on the semblance and the estimated attributes I show in the following.

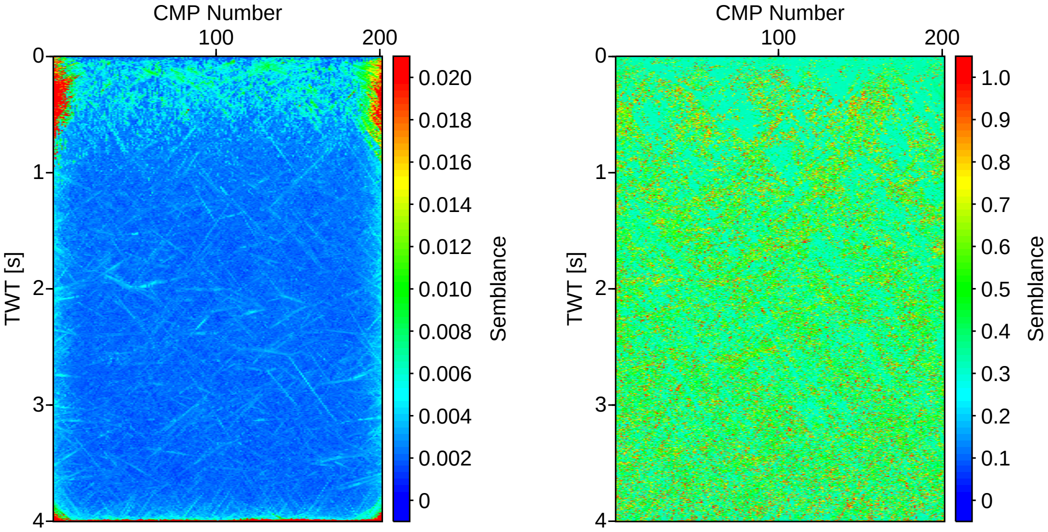

(a) Uniform noise

(b) Gaussian noise

Figure 5.3.: Semblance of the estimated CRS traveltime surface of input data containing uniform and Gaussian noise.

The α section is shown in Figure 5.4 for the uniform (Figure 5.4(a)) and Gaussian noise (Figure 5.4(b)). While the general appearance is similar, the histogram for the Gaussian noise (Figure 5.4(d)) shows two preferred directions at ±70° compared to the uniform noise (Figure 5.4(c)). The general distribution in both cases is a Gaussian bell curve. This is expected for Gaussian noise, however, not for uniformly distributed noise. One possible explanation is a low number of random values. Another possibility is that a limited discretization never leads to purely uniform noise. Boundary effects of the search space might also play a role. I suggest a deeper investigation of the origin for future work.

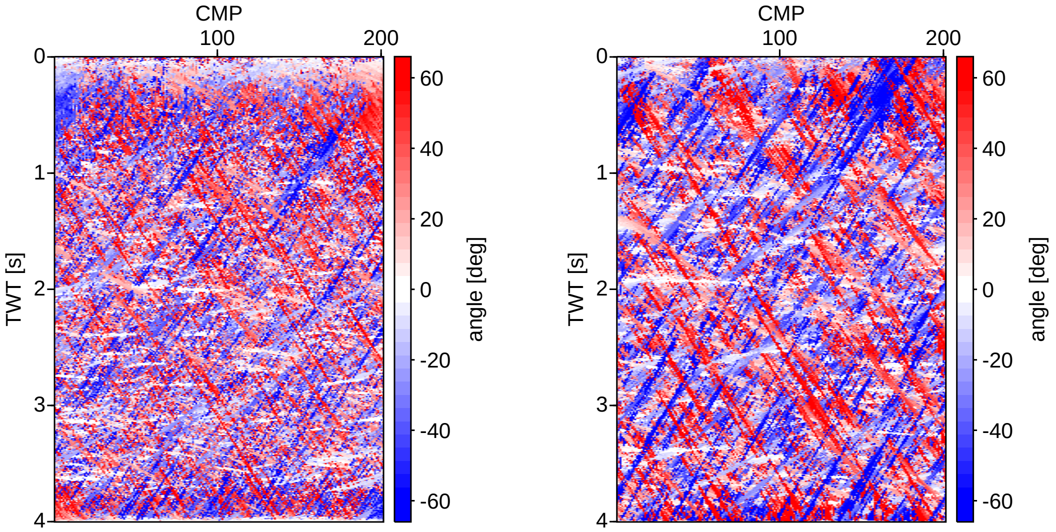

(a) Uniform noise

(b) Gaussian noise

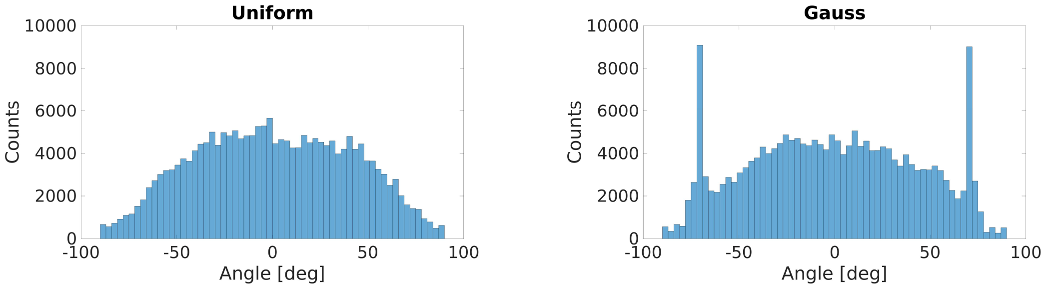

(c) Histogram of uniform noise

(d) Histogram of Gaussian noise

Figure 5.4.: CRS attribute α and histograms of data containing uniform and Gaussian noise. The histogram the Gaussian noise (d) shows undesired preferred directions at roughly ±70°.

In Figure 5.1(c) I showed, similar to Guntern (2016) that the radius of the normal-incidence-point wave R_{NIP} has a bias due to the choice of the near surface velocity. The same gradient can be observed for apparent events which are not present in the actual pre-stack data as the stacks have shown. However, their position coincides with coherent events in the angle section shown before.

According to Equation 2.9 α and R_{NIP} can be translated to the moveout velocity V_{NMO} which is shown in Figure 5.6. The Gaussian noise (Figure 5.6(b)) shows more coherent events than the uniformly distributed noise (Figure 5.6(a)) which is undesired. In principal, the input data should ideally not show any coherence at all. Some apparent events have hyperbolic shape and can be mistaken as diffractions, which is really troublesome when diffraction imaging is an aim.

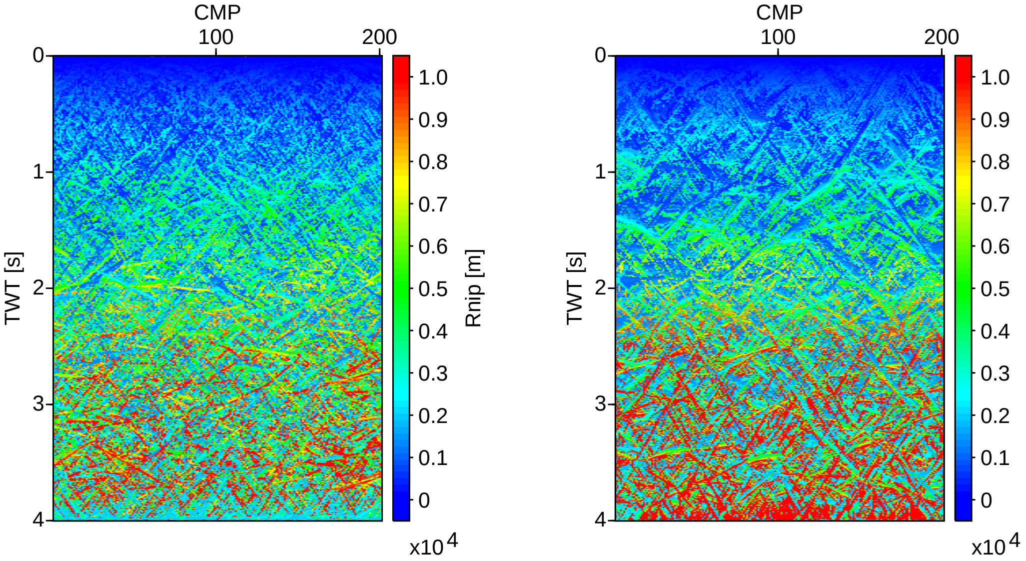

(a) Uniform noise (b) Gaussian noise

Figure 5.5.: CRS attribute R_{NIP} of data containing uniform and Gaussian noise.

The radius of the normal wave R_N is the least stable parameter of the CRS parameter estimation and shows very few coherent signals in case of uniform noise (Figure 5.7(a)). Like in the other attribute sections before, Gaussian noise shows more coherent events (Figure 5.7(b)) in principle. However, the differences for R_N are not as pronounced as in other attribute sections.

Noise is an issue in CRS processing as it can introduce non-existing events. If misinterpreted and/or not removed prior to migration they will be migrated as well, disrupting the final image. Therefore, interpretation of steep dipping events and hyperbolic events in CRS stacks need to be done carefully.

In the next chapter I show results of the introduced method on an industrial marine data set.

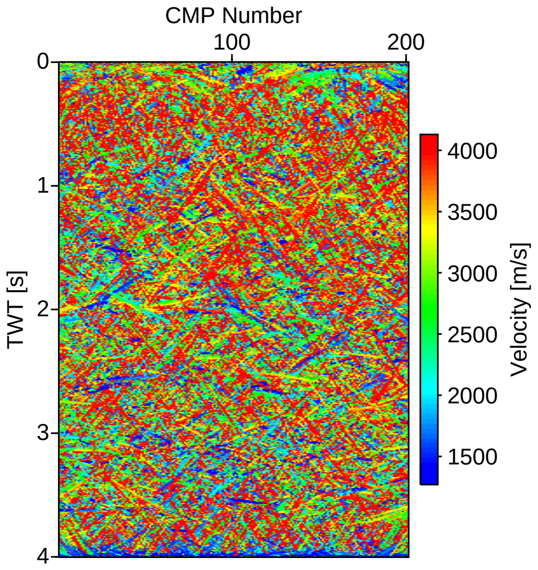

(a) Uniform noise

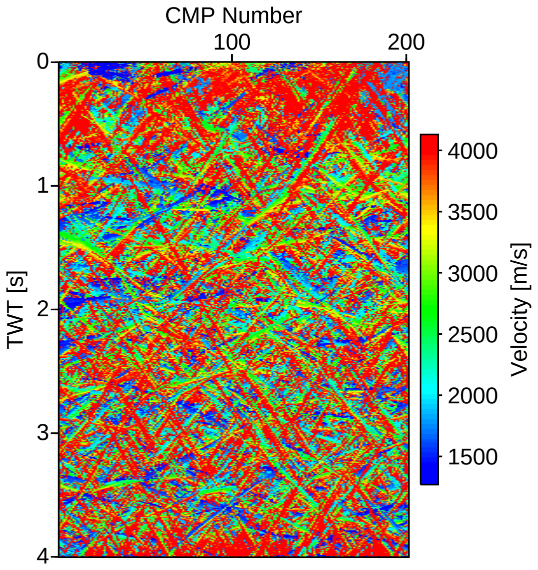

(b) Gaussian noise

Figure 5.6.: Moveout velocity V_{NMO} of data containing uniform and Gaussian noise.

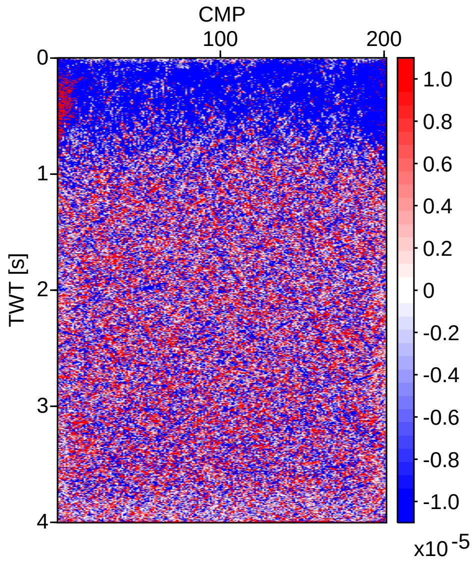

(a) Uniform noise

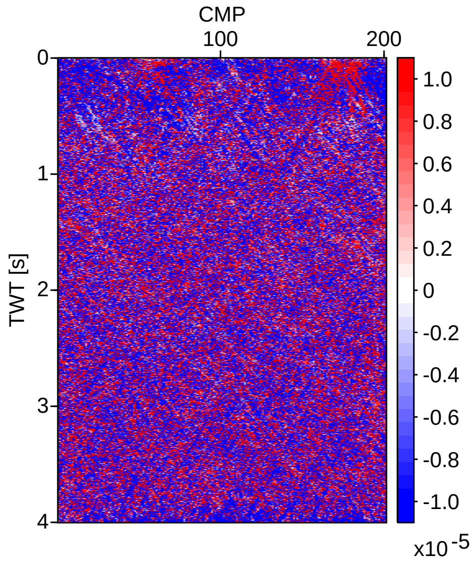

(b) Gaussian noise

Figure 5.7.: CRS attribute $K_N = 1/R_N$ of data containing uniform and Gaussian noise.

Chapter 6.

Marine data

The marine field data set was acquired by TGS-NOPEC and is located in the Levantine basin in the Eastern Mediterranean Sea (Figure 6.1). The Levantine basin extends to Cyprus in the north, the Egyptian coast in the south and the Levantine coast in the east. The Levantine basin is rich of salt tectonics (Netzeband et al., 2006) leading to a complex geological setting, which becomes challenging in seismic imaging, especially time processing.

The data was acquired by the company TGS-NOPEC from September to December 2001. The processed profile is a 2-D line in SW-NE orientation from a large number of profiles in Strike (SW-NE) and Dip (NW-SE) orientation. The shot point interval is 25 m and the group interval of the receiver is 12.5 m. It has a minimum offset of 150 m and a maximum offset of 7338 m covered by 576 recording channels resulting in a nominal fold of 144. The covered subsurface contains a fault system in the central part of the data, salt rollers beneath and a slump complex surrounded by sediments, shown in Figure 6.2 (Netzeband et al., 2006). Due to the faults and the rough top of salt topology, a high amount of diffractions can be observed in the data. Therefore, it is particularly suited for diffraction imaging and suffers severely from conflicting dip situations, making it an excellent data set to demonstrate the potential of the proposed method. During early stages of the work, Walda and Gajewski (2015a) showed first results. However, no constraints during optimization were used. The required processing parameters to perform the CRS attribute search are listed in Table 6.1. Apertures used in ZO and partial stack as well as diffraction separation and migration are shown in Table 6.2. The threshold for the diffraction weight is applied for Equation 2.24.

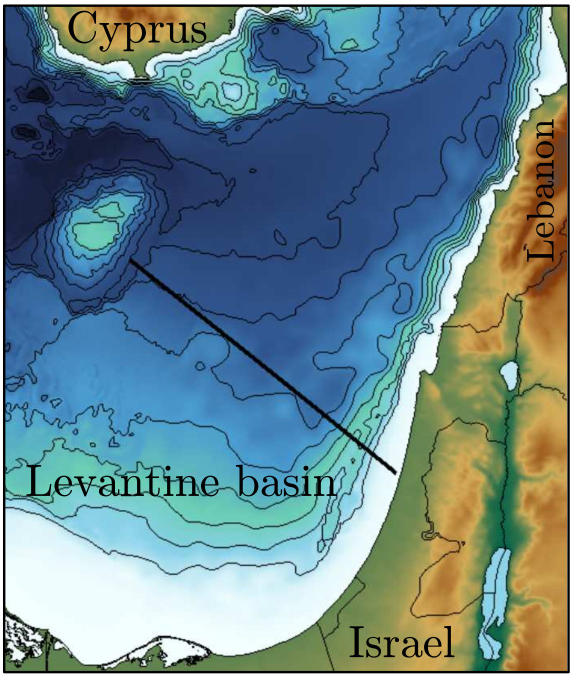

Figure 6.1.: Location of the marine profile (black line) in the Mediterranean Sea (modified after Netzeband et al., 2006).

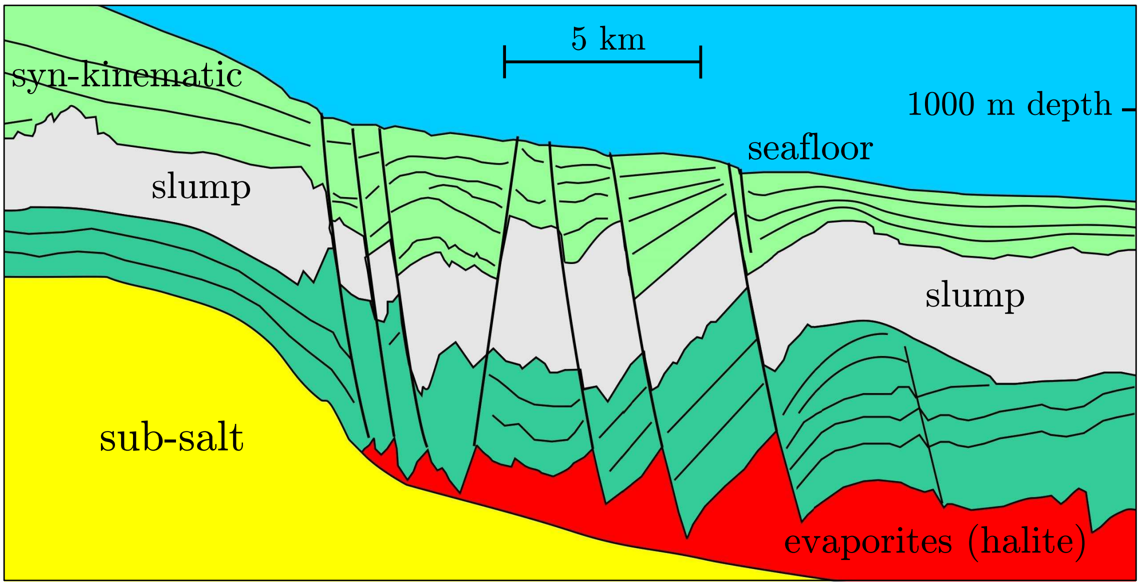

Figure 6.2.: Geological setting of the marine data after Netzeband et al. (2006).

General parameters	
Dominant frequency	40 Hz
Coherence measurement	Semblance
Coherence time window	26 ms
Velocity constraints	
Near surface velocity	1480 m/s
Lower moveout velocity constraints	1300 m/s
Upper moveout velocity constraints	4000 m/s
Search apertures	
Minimum midpoint aperture	300 m at 0 s
Maximum midpoint aperture	500 m at 5 s
Minimum offset aperture	750 m at 0 s
Maximum offset aperture	3000 m at 5 s
Conflicting dip handling	
Number of dip intervals	17
Dip intervals in °	[-90,-45], [-45,-22.5], [-22.5,-15], [-15, -10], [-10,-7], [-7,-4], [-4,-2], [-2, -0.75] ,[-0.75,0.75], [0.75,2], [2,4], [4,7], [7,10], [10,15], [15,22.5], [22.5, 45], [45,90]
Global optimization parameters	
Algorithm	Differential evolution
Number of individuals	20
Crossover probability	74.55 %
Differential weight	0.9362
Minimum number of iterations	30
Maximum number of iterations	200
Number of allowed stagnated iterations	10
Local optimization parameters	
Lower coherence threshold	1.00 at 0 s
Upper coherence threshold	1.00 at 5 s
Maximum number of iterations	100
Minimum deviation required	10^{-5}
Transformation radius of R_N	100 m
Initial variation of emergence angle	2 °
Initial variation of R_{NIP}	3 %
Initial variation of R_N	4 °

Table 6.1.: Search parameters for the marine data. For this data the local optimization was not used.

Stacking parameters	
Minimum midpoint aperture	50 m at 0 s
Maximum midpoint aperture	150 m at 5 s
Minimum offset aperture	100 m at 0 s
Maximum offset aperture	3000 m at 5 s
Velocity tolerance for multiple prediction	5 %

Diffraction separation	
Minimum midpoint aperture	50 m at 0 s
Maximum midpoint aperture	150 m at 5 s
Minimum offset aperture	750 m at 0 s
Maximum offset aperture	3000 m at 5 s
Diffraction weight threshold	0.5

Partial stacks	
Regularized receiver interval	25 m
Minimum local midpoint aperture	50 m at 0 s
Maximum local midpoint aperture	150 m at 5 s
Local offset aperture	50 m

Migration	
Minimum midpoint aperture	1000 m at 0 s
Maximum midpoint aperture	2000 m at 5 s
Minimum offset aperture	2000 m at 0 s
Maximum offset aperture	4000 m at 5 s

Table 6.2.: Stacking parameters for the marine data. In case of a post-stack migration the offset aperture is zero.

6.1. Stack and attributes

The stack is mostly the first interpretable image of the subsurface available during the processing. It is important to identify important geological features that need to be taken into account in further processing steps, particularly velocity model building. Furthermore, it is the input for poststack migration algorithms. Events lost during this processing step cannot be recovered in poststack migration and lead to misinterpretation.

The CRS wavefront attributes are of importance for many CRS applications as described in Chapter 2. Better estimated attributes improve the result of, e.g., data enhancement and diffraction separation. The quality of the estimated attributes are measured by the obtained semblance. In general, the higher the semblance the more energy is stacked constructively. This happens when the traveltime curve or surface fits the data accurately. In the following section I compare the stacks obtained by the previously introduced methods from literature and the proposed method using the hyperbolic second order CRS operator (Equation 2.5).

6.1.1. CRS stack

The conventional CRS stack result is shown in Figure 6.3. The stack shows the main features of the data set but provides very little information on smaller details due to truncated and hidden events. The CRS stack obtained by the idea of Soleimani et al. (2009b) using the full CRS operator introduces a number of problems (Figure 6.4). In principle conflicting events are imaged but an undesired signal stretch can be observed which causes several problems (Walda and Gajewski, 2015c). This is equivalent to a major change in the frequency content, destroying amplitude information. Also events are balanced unreasonably. Diffractions scatter in every direction while reflections reflect all incoming energy according to Snell's law. Assuming a similar impedance contrast between two layers, this means the measured energy at a receiver for a diffraction should be far lower. This is not the case in Figure 6.4 where diffraction tails from faults are of higher energy than slightly dipping reflections. Furthermore, 161 operators had to be determined. This leads to a tremendous computational cost. Figure 6.5 shows the proposed method with 19 dip cluster. Conflicting events are well imaged, no signal stretch or change in frequency content is observable and the amplitude distribution is more consistent with Figure 6.3. In this case I used far more dip clusters then necessary to obtain a good image. Similar results are achievable with 8-10 dip cluster. Compared to before this means roughly 20 times fewer operators need to be determined. Therefore, this approach is less computational demanding.

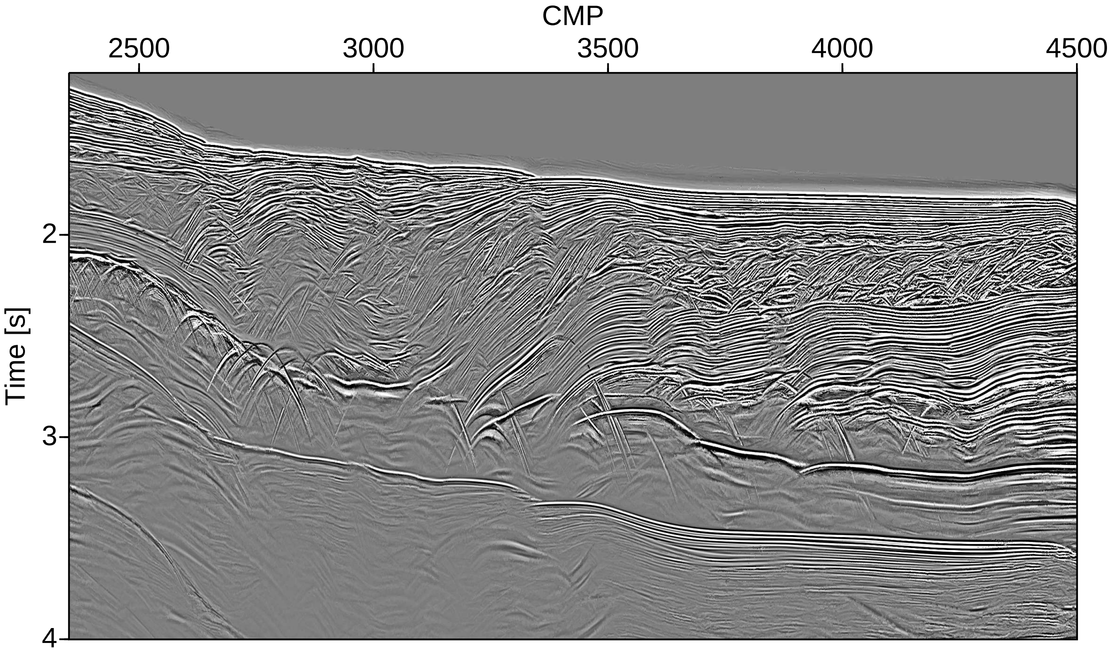

Figure 6.3.: Conventional CRS stack of the marine data from the Levantine Basin.

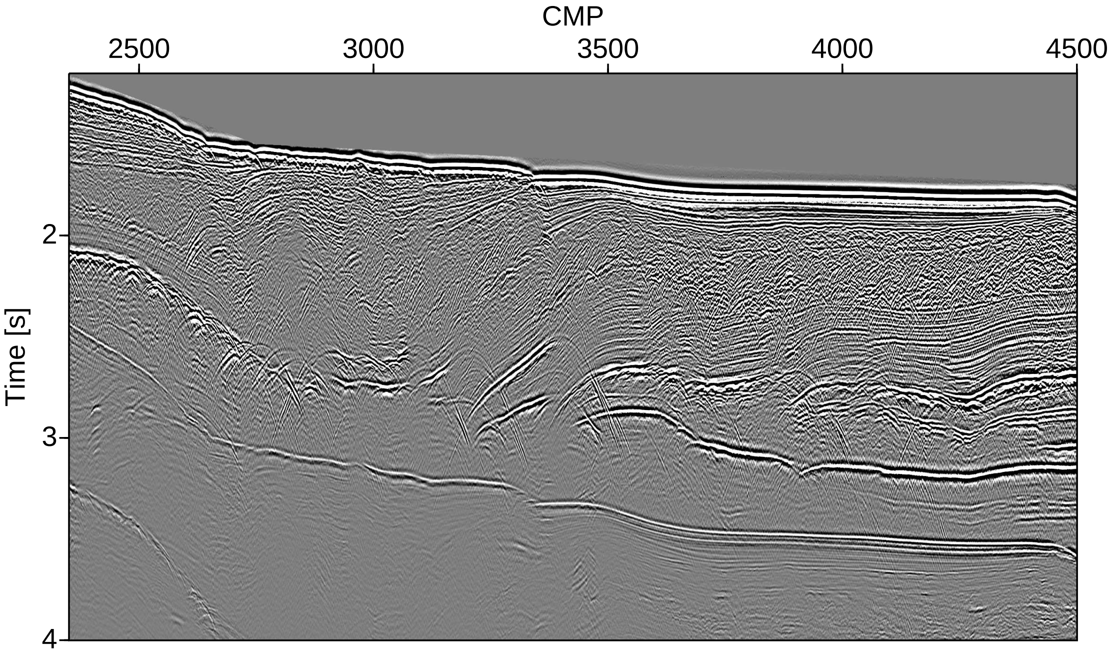

Figure 6.4.: CDS stack of the marine data from the Levantine Basin using the full CRS operator.

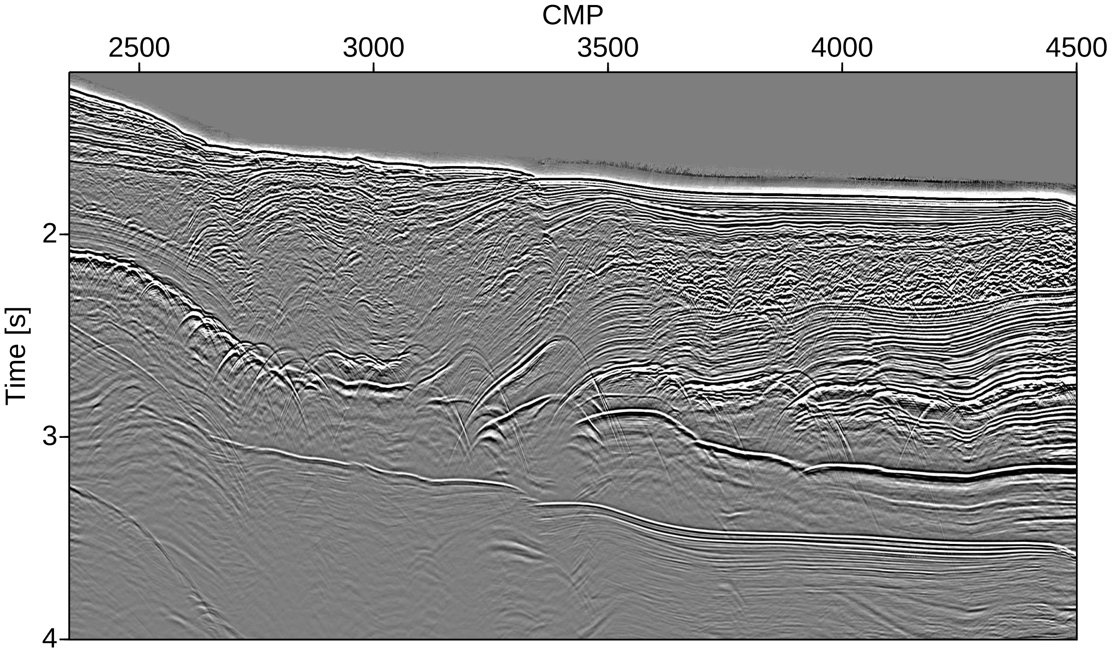

Figure 6.5.: Proposed angle decomposition CRS stack of the marine data from the Levantine Basin.

6.1.2. CRS wavefront attributes

The estimated CRS wavefront attributes are critical for a high quality stack and additional applications like prestack data enhancement, diffraction separation and time migration. Wrongly estimated parameters will lead to an inaccurate velocity and moveout estimation as well as noisy fluctuations which requires parameter smoothing. This however, smoothed over small scale information. The CRS wavefront attributes consist of two wavefront curvatures, which are of second order, and a first order angle of incidence or scaled slope. Therefore, the angle α is the most impactful and thus the most stable and reliably estimated parameter. The NIP wave radius R_{NIP} is in general more stable than the N wave radius R_N. Since it is not possible to show all results here, I demonstrate the improvements of the developed method on the most stable parameter α and the least stable parameter R_N. Furthermore, the objective function optimized, the semblance is shown to evaluate the optimization success.

Figure 6.6 shows an overlay of the estimated angle α and the corresponding conventional CRS stack. The attribute becomes noisy at the beginning of the salt body and below. furthermore, small angles of reflections cut through diffractions which leads to very inconsistent attributes in further applications. Figure 6.7 shows the angle of incidence of the most coherent event per sample found in the 121

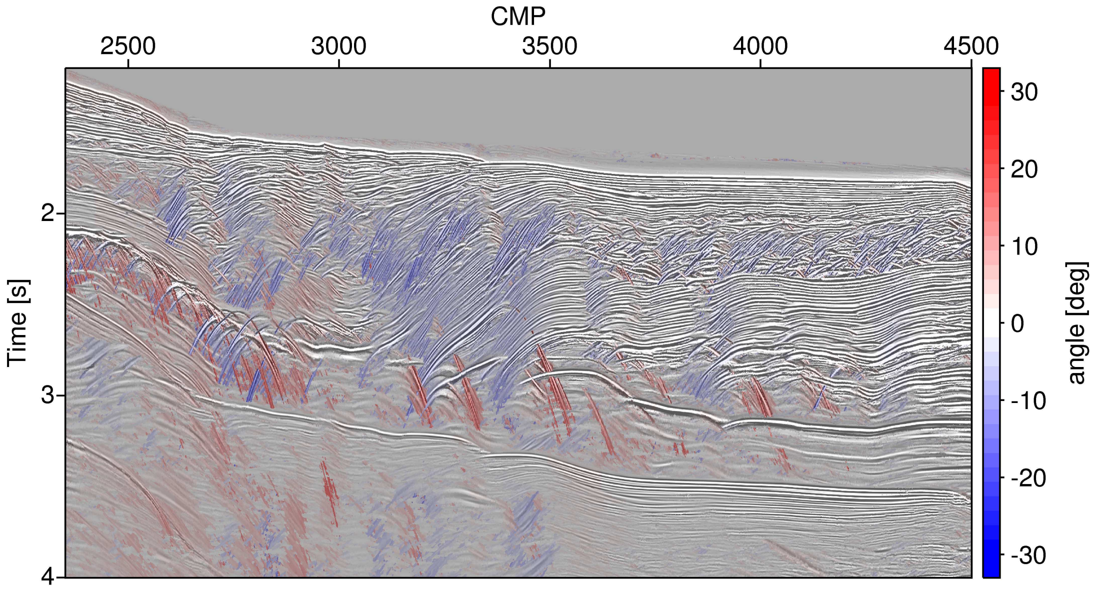

Figure 6.6.: Overlay of the conventional CRS stack with the wavefront attribute α.

estimated CRS operators. While each operator delivers their own angle section, they cannot be displayed here since there are too many. They also do not deliver any information when no event is found for a specific angle. The accuracy of the angle attribute is rather low, since in the extension of the CDS method, the angle is fixed with a 1° spacing. However, a difference of 1° can have a significant impact in the accuracy of other attributes. In principle, the section should deliver similar results as Figure 6.6 which is the case. However, within and below the salt body the angle is more noisy, indicating worse attributes. Figure 6.8 shows the angle of the most coherent event for the proposed angle decomposition method. The estimated angles are much more consistent and less noisy, even in and below the salt body. Almost no parameter noise indicates reliable attributes which is important for further applications.

To visualize the radius of the N wave, it is not suitable to choose the Radius itself, as nearly horizontal reflections will lead to an infinite radius of the N wave and depending on the shape, also might alternate between positive and negative algebraic sign. It is more practical to plot the inverse, K_N, where a plus/minus infinite radius becomes 0. Another advantage of this is, that diffractions have high positive values and are easy to spot. This directly indicates if they can be identified in diffraction separation methods. Figure 6.9 shows the K_N section of the conventional CRS stack. While the most prominent diffractions can be identified, the slump complex between the two layer parts above the salt body is very diffuse and noisy. The values indicate diffractions but non are clearly visible. The results of the most coherent sample for the extended CDS method in Figure 6.10 show better results for the slump complex

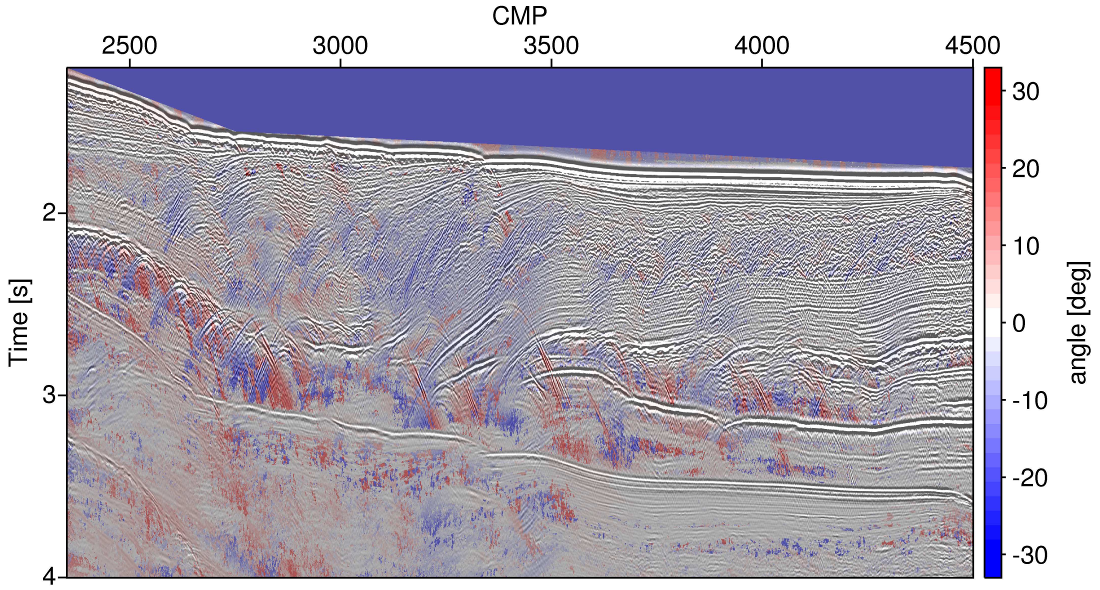

Figure 6.7.: Overlay of the CDS stack with the wavefront attribute α using the full CRS operator. The blue area at the top was not calculated.

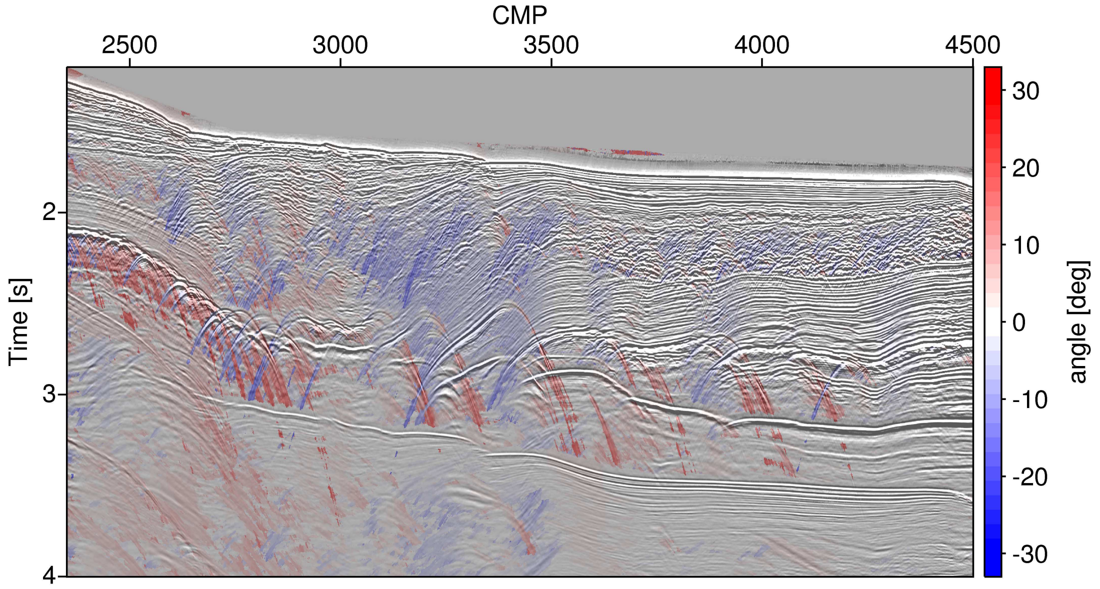

Figure 6.8.: Overlay of the proposed angle decomposition CRS stack with the wavefront attribute α.

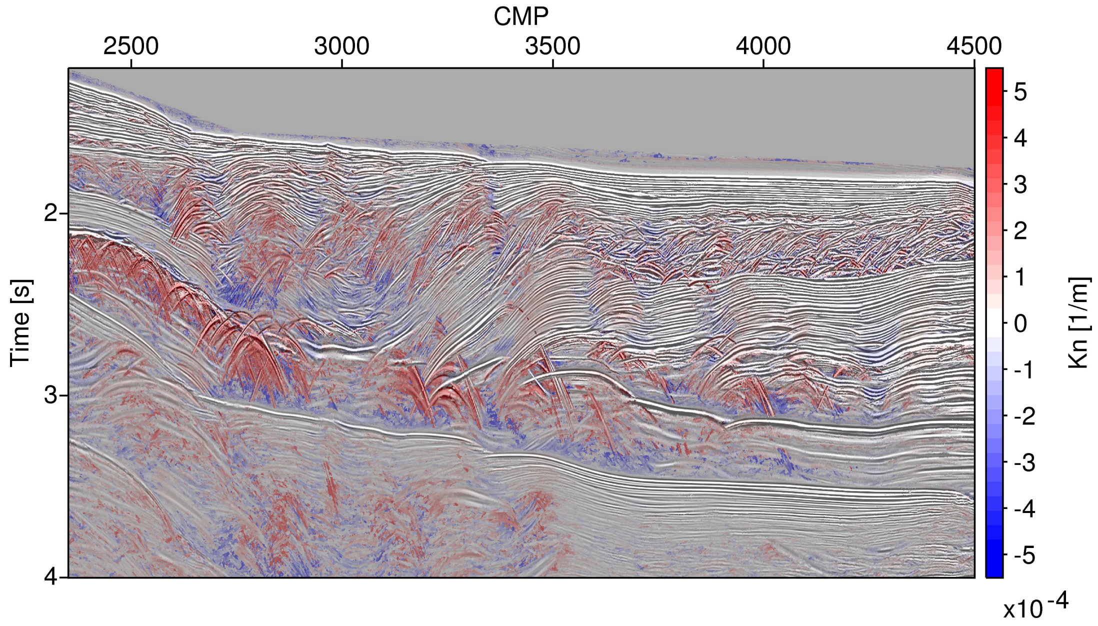

Figure 6.9.: Overlay of the conventional CRS stack with the wavefront attribute K_N.

where diffractions can be identified. However, within and below the salt, the section becomes very noisy. It seems that the attribute is smeared arbitrarily in some areas of the image. This is not so much the case for the proposed method shown in Figure 6.11. The estimated attribute coincides better with the events and are not smeared as much. Furthermore, much more details can be observed in the slump complex, showing a highly scattering complex.

One way to evaluate the estimated CRS wavefront attributes is to investigate the obtained section as done above. Another important asset to analyse is the value of the actual objective function that is maximized. The semblance varies between zero and one. A value of one means that all energy in the used window is fitted perfectly which is rarely ever the case in field data. However, high semblance values indicate a good fit. This is best criterion available to decide, whether the estimated attributes are accurate or not. The semblance of the conventional CRS stack is shown in Figure 6.12. The layered area shows quite high semblance values which means they are fitted well. The slump complex and the salt body have lower values which indicates a less accurate fit for the more complex areas of the data. The semblance along diffraction events becomes noisy and very low. This is equivalent to a bad fit for diffractions due to the parameter estimation. Another problem is a truncation of fitted events, mostly in the deeper parts, leading to inconsistent results. Diffractions are fitted better by the extended CDS method (Figure 6.13), however reflections show a much lower semblance. This means overall, the fit is worse and the estimated attributes are less reliable. This is especially visible in the lower part of the data. Using the obtained attributes of such worse fits can lead

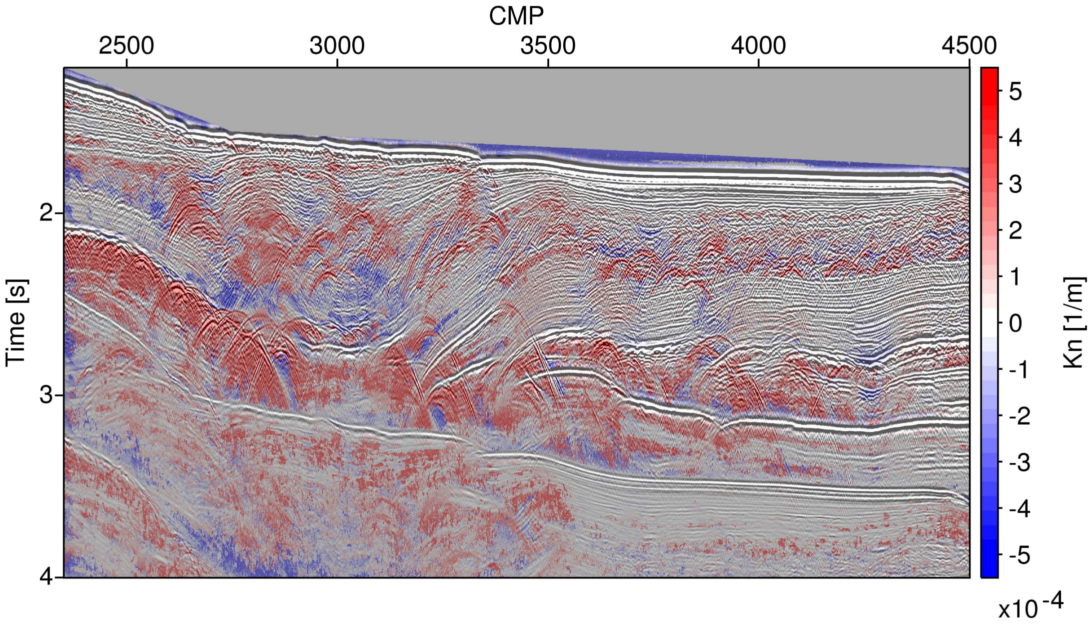

Figure 6.10.: Overlay of the CDS stack with the wavefront attribute K_N using the full CRS operator.

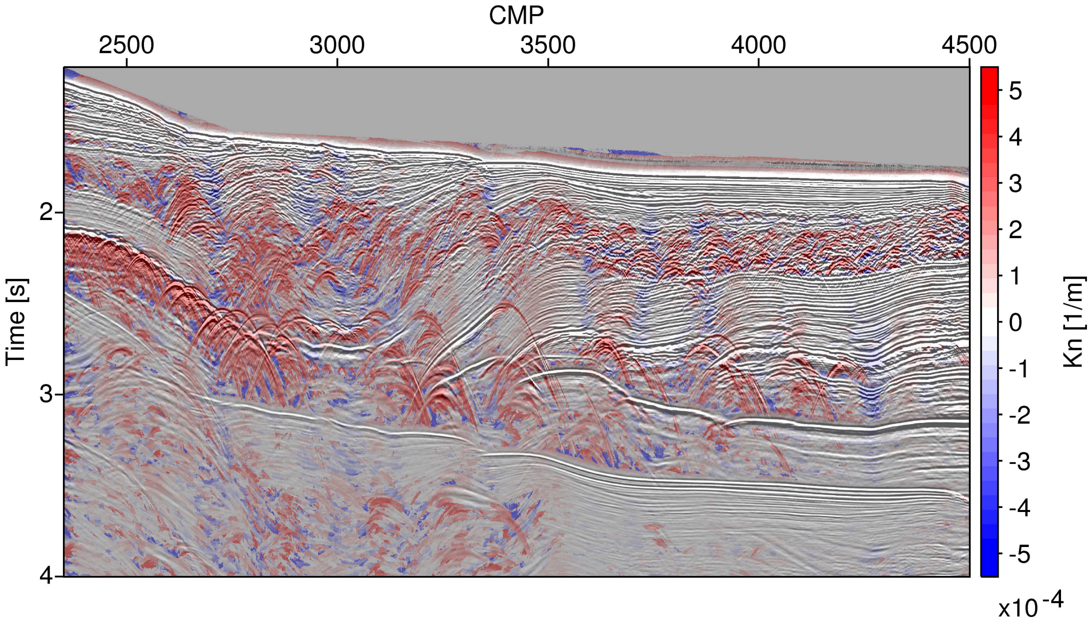

Figure 6.11.: Overlay of the proposed angle decomposition CRS stack with the wavefront attribute K_N.

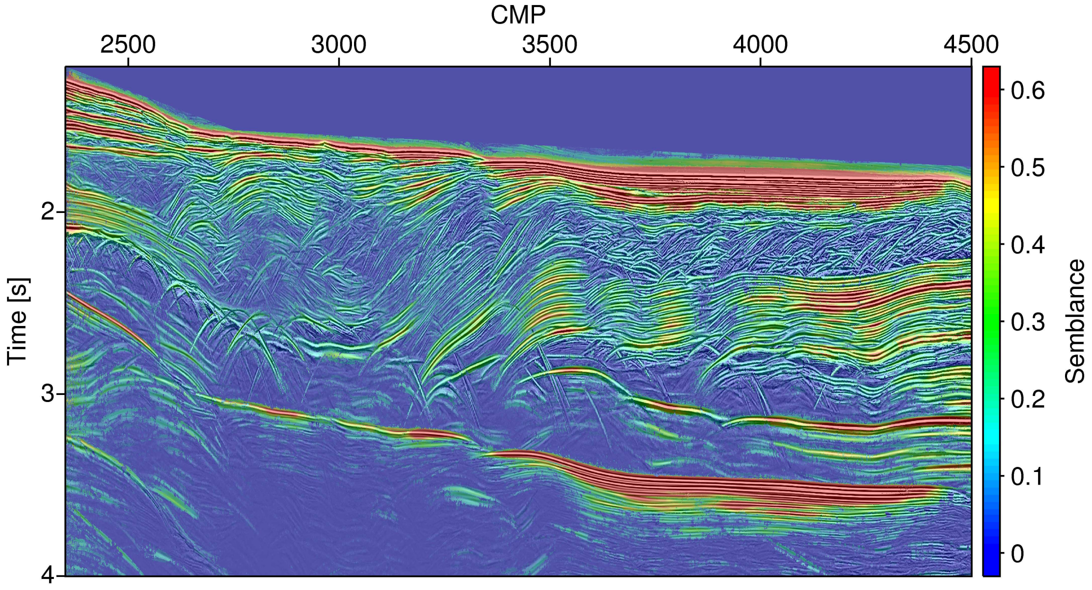

Figure 6.12.: Section showing the highest semblance found per sample of the conventional CRS. The stack is overlain.

to errors, e.g. in data enhancement or velocity estimation. Figure 6.14 shows the semblance of the most coherent event for the proposed method. The reflections are fitted as well as in the conventional CRS method while diffractions are fitted as nicely as in the extended CDS method. The results show the best of both previous methods without most of the disadvantages like signal stretch or bias towards either diffractions or reflections. Furthermore, the overall semblance is the highest which means more energy is fitted constructively. Since the objective function has higher values, the used optimization method delivers a better result in the sense of function maximization.

Since the CMP method is used for more than fifty years, the corresponding attribute: normal-moveout velocity V_{NMO} is better known within the community. It can be calculated from the CRS attributes α and R_{NIP} using Equation 2.9. Figure 6.15 shows the overlay of the estimated moveout velocity with the stack for the most coherent event of the proposed method. It should be noted, that every operator provides a moveout velocity field which can be used to approximate a better migration velocity, shown in Chapter 6.3. The velocity field is very smooth which is expected in time imaging. However, smaller features like strongly dipping events near faults, which show a higher moveout velocity, are still visible. Since no velocity guide function is used for the marine data, the algorithm images multiples well, which show a higher semblance than events beneath. This is not necessarily a disadvantage. In principle, it can be used to image and remove multiples as touched briefly in the outlook (Chapter 9).

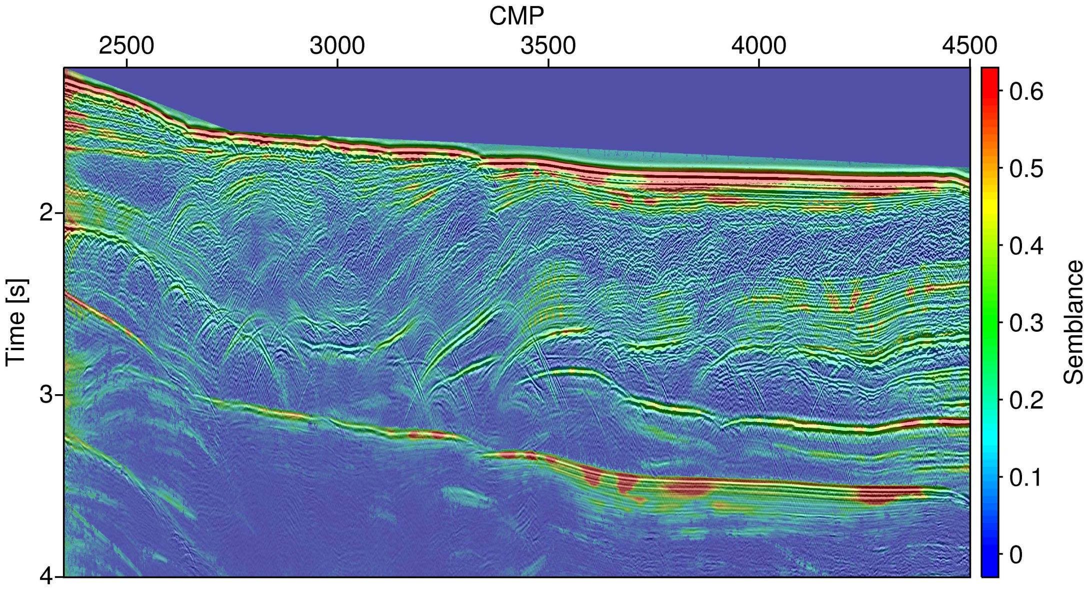

Figure 6.13.: Section showing the highest semblance found per sample of the CDS method using the full CRS operator. The stack is overlain.

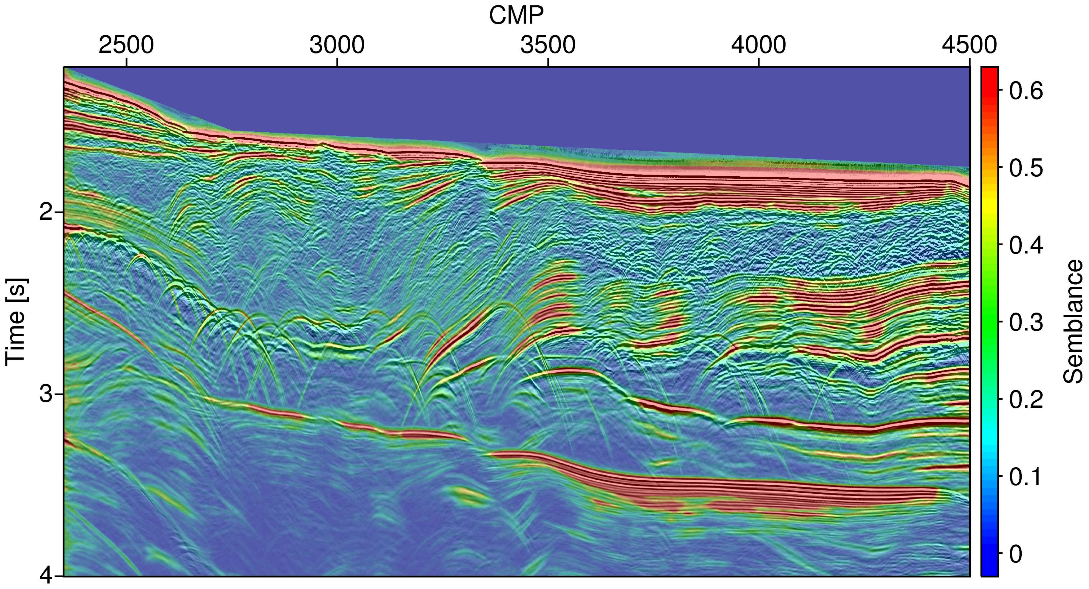

Figure 6.14.: Section showing the highest semblance found per sample of the proposed angle decomposition CRS. The stack is overlain.

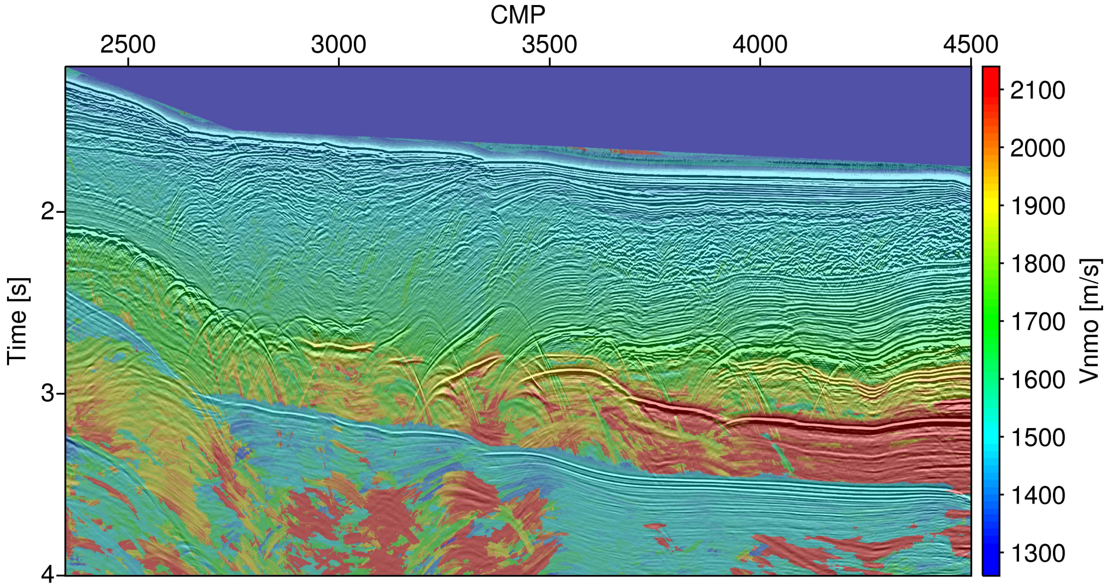

Figure 6.15.: Improved CRS stack of the marine data from the Levantine Basin overlain with the estimated moveout velocity.

6.2. Data enhancement

A highly valuable application of the shown wavefront attributes is the partial CRS stack, where regularized and enhanced prestack data is generated from extrapolated traveltimes based on ZO wavefront attributes. Results for one CMP are shown in figure 6.16. A general reduction of noise and regularized offsets can be observed while all conflicting events are recovered which was not possible so far. This is further shown in common-offset gather for an offset of 2000 m of the original data (Figure 6.17), the CRS method without conflicting dip treatment (Figure 6.18) and the proposed workflow shown in Figure 6.19. In this case the original data is of good quality. Therefore, I expect to recover and enhance all events present in the data. CRS without conflicting dips is able to enhance the data but loses of information, especially in the slump complex, the salt body and when multiples occur. The angular decomposition workflow enhances the data quality as well while not losing any visible information. The prestack data shows that a correct treatment of conflicting dips in data enhancement is mandatory. Otherwise, useful energy is filtered out during the enhancement process and filtering out important energy leads to wrong results.

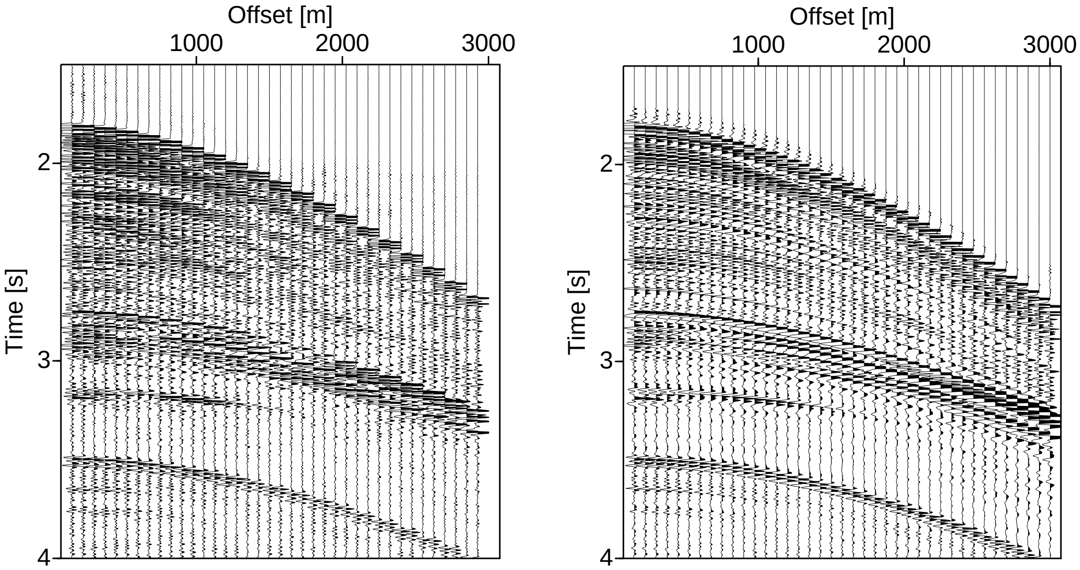

(a) Original CMP gather 3946

(b) Partial CRS gather 3946

Figure 6.16.: Original (a) and partial CRS (b) CMP gather 3946 using 19 dip ranges and DE optimization algorithm.

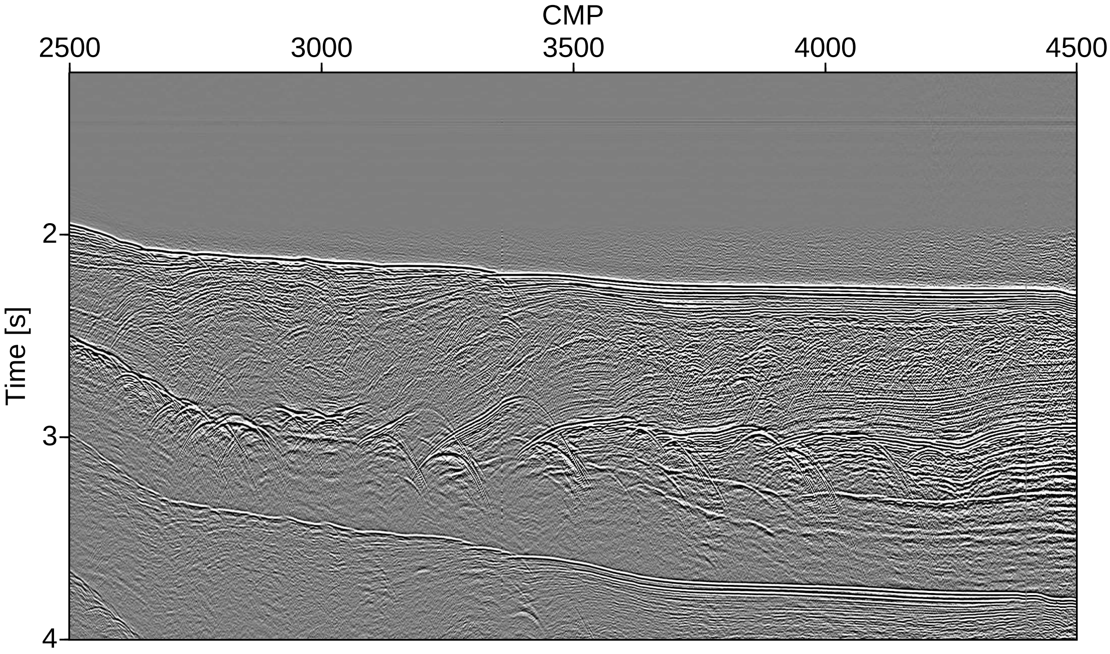

Figure 6.17.: Common-offset gather of the original data at an offset of 2000 m.

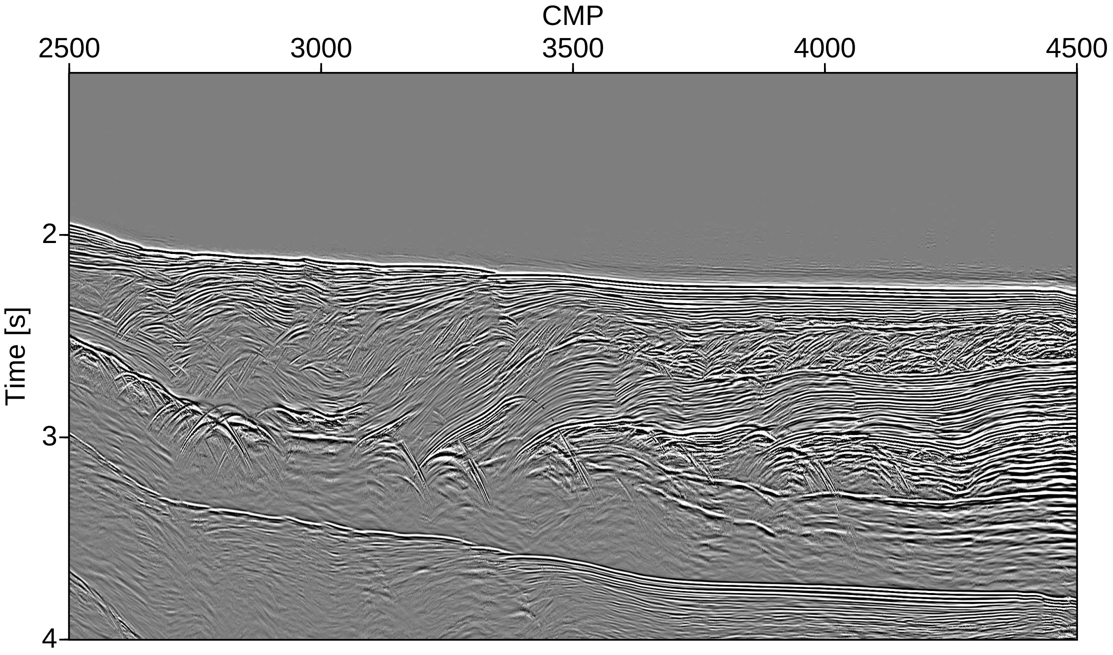

Figure 6.18.: Common-offset gather of, by partial CRS without conflicting dips, enhanced data at an offset of 2000 m.

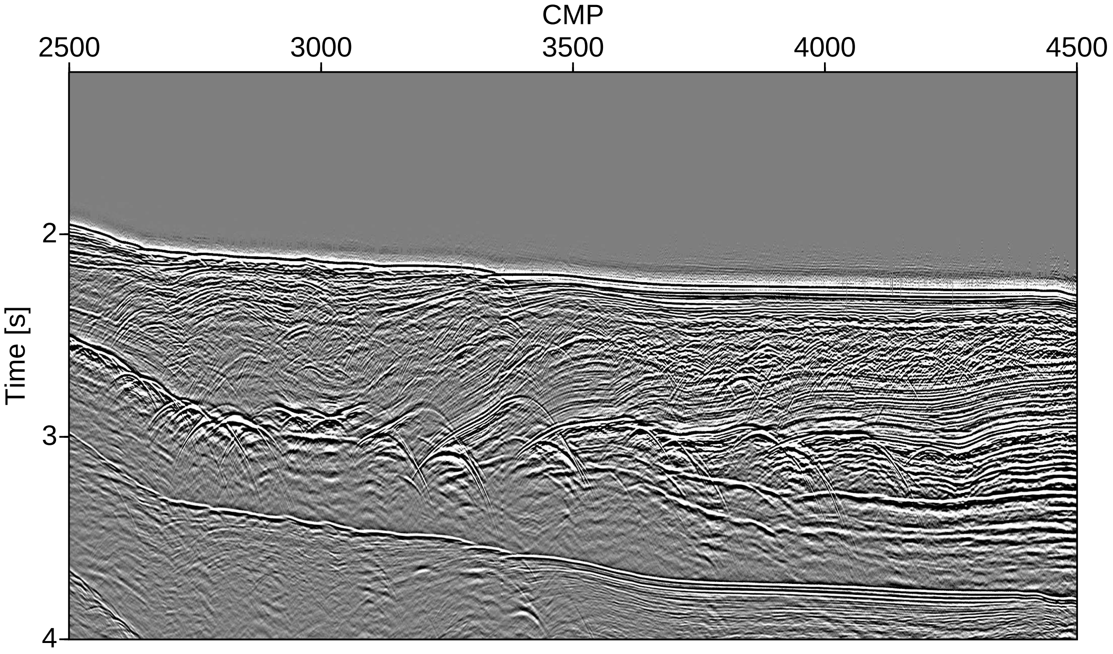

Figure 6.19.: Common-offset gather of, by partial CRS with conflicting dips, enhanced data at an offset of 2000 m.

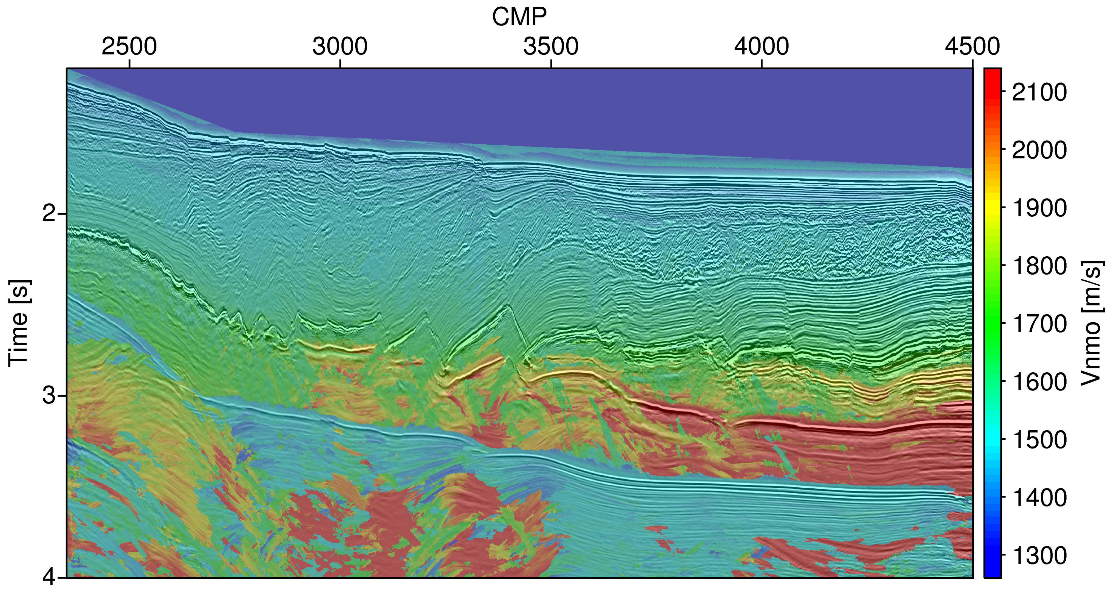

Figure 6.20.: Post-stack migration using the dip corrected velocity of Equation 2.9.

6.3. Migration

Since the CRS wavefront attributes contain velocity and dip information the obtained moveout velocity model can be dip corrected. This represents the root-mean-square velocity which is appropriate for the use in time migration. Figure 6.20 shows the time migration result of the data where the velocity is taken from the most coherent event, i.e. global maximum. However, the proposed method delivers the CRS attributes for all intersecting events. Therefore, using all contributions by Equation 2.26 improves the velocity model and therefore the migration result shown in Figure 6.21. The main improvements are visible for the salt roller, especially the bottom of salt at 2.8 s to 3 s. The velocity model is more consistent and smoother while the migration shows more precise boundaries.

6.4. Diffraction separation

Diffractions contain tremendous amounts of useful information and can contribute significantly, if exploited well. In recent years, a lot of research is going in this direction and the CRS method is a particularly useful tool since the CRS wavefront attributes differ in case of reflections and diffractions. This can be used for diffraction separation. The application to the marine data set is displayed in Figure 6.22, where I calculated a diffraction weight using Equation 2.24. The weight function is close to

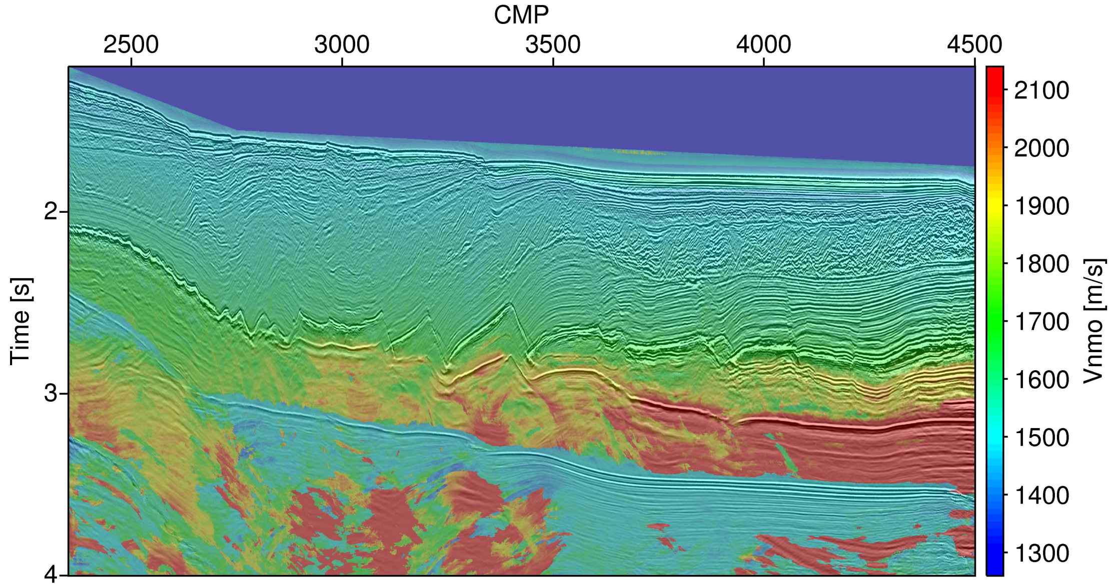

Figure 6.21.: Post-stack migration using the semblance weighted and dip corrected velocity of Equation 2.26.

zero for almost all reflections visible in the data while diffractions have high values, thus making a separation in principle feasible. However, most diffractions are hidden beneath reflections since they are weaker signals. A simple diffraction separation by the choice of a threshold (here 0.5) for the most coherent event delivers only very few and partly truncated diffractions as shown in Figure 6.23. The proposed angular decomposition is able to provide CRS wavefront attributes for the weaker diffraction events as well, which results in a tremendous amount of recovered diffraction energy (Figure 6.24) compared to Figure 6.23. The diffraction separation can be applied in conjunction with partial CRS to generate prestack diffraction only data. This data can be used in prestack time migration to characterize faults. A basic diffraction summation migration result is shown in the outlook (Chapter 9) as a first result. However, diffraction imaging still suffers from problems regarding artefacts and incontinuous events after separation.

The results up to this point are obtained using the second order hyperbolic CRS operator. As introduced in the theory (Chapter 2), higher order double square root operators are available. In the next section I will use the proposed method to competitively compare all those operators without initial bias, the same parametrization and algorithm. This ensures that all differences are caused solely by the investigated operator.

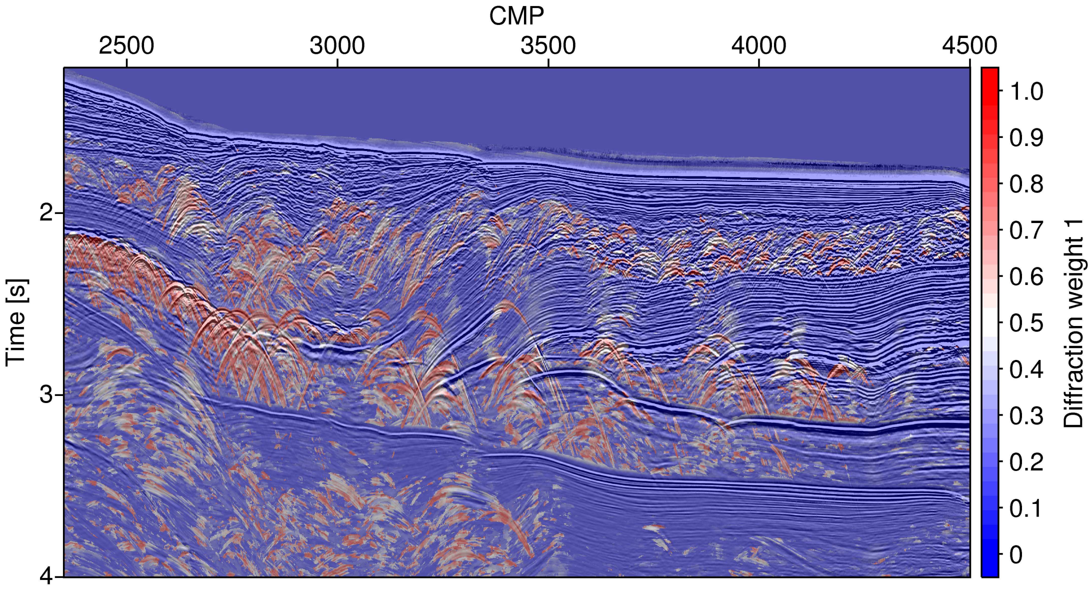

Figure 6.22.: Weight function of the most coherent event for the diffraction separation overlain with the stack.

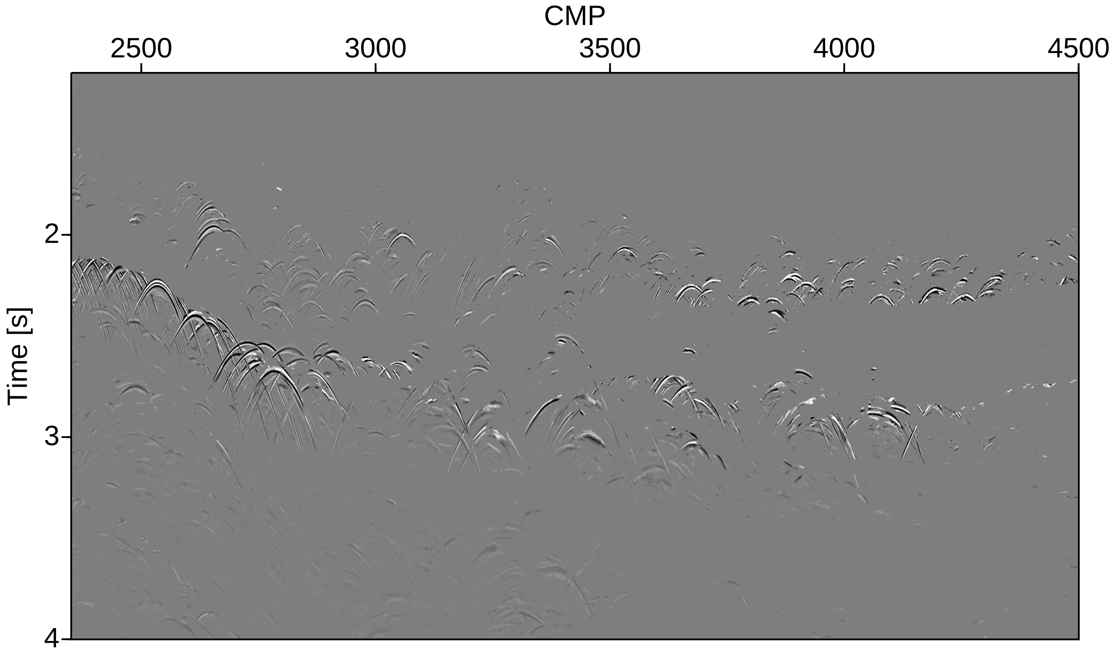

Figure 6.23.: Diffraction separation without conflicting dip treatment. A few diffractions can be seen. However, most diffractions within the data are hidden.

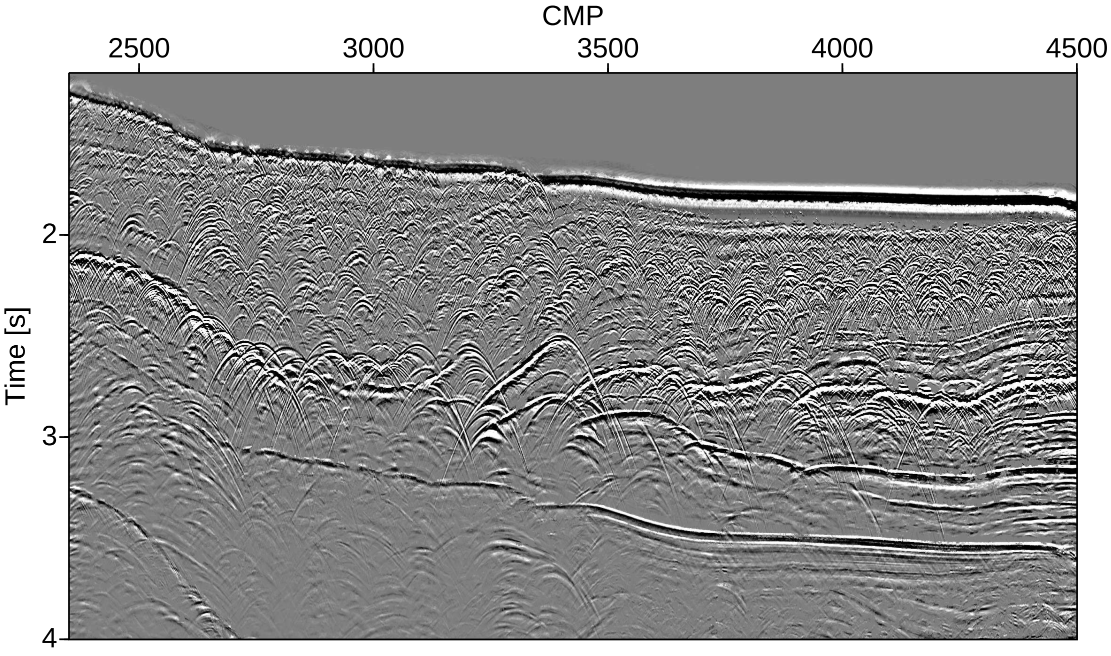

Figure 6.24.: Diffraction separation considering conflicting dips. Most diffractions can be successfully separated. However, residuals are left at the seafloor, the bottom of salt and the respective multiples.

6.5. Comparison of CRS type operators

In the previous sections, only the performance of the proposed angular decomposition method with previously existing ones are investigated. However, there are more CRS-type operators available than the conventional CRS method. In Chapter 2 alternatives are introduced, i.e. non-hyperbolic CRS, implicit CRS and multifocusing. In order to find the most suited operator, especially for diffraction imaging, their performance under the very same conditions, e.g., algorithm, aperture and parametrization, are compared. The sole difference is the operator used for traveltime fitting to calculate the semblance.

A method to gain more insight on the behaviour of the operators and how they shape the objective function is to calculate the objective function on a specific test case. Figure 6.25 shows the location of a test sample where the objective function is investigated in the following. The α-R_{NIP} planes of constant R_N of every operator is plotted in Figure 6.26. The aperture is rather small in this case, with a midpoint aperture of 200 m and an target-offset ratio of roughly 0.5. The colour coded semblance is clipped to show the diffractions, since the reflection has a much higher semblance. The chosen aperture is within the hyperbolic limit of a target-offset ratio of roughly 1:1, therefore all operators fit the events well and we do not observe significant differences between each operator. This changes when the aperture is increased as in Figure 6.27. The midpoint aperture in this case is 800 m and the target-offset ratio approximately 2:1. Since this is far beyond the hyperbolic limit, the CRS operator cannot fit the diffractions anymore and they are hardly recognizable. Furthermore, the estimated attributes differ as well as the general shape of the objective function. This is not so much the case for the higher order operators multifocusing, iCRS and nCRS. They do not differ at the event location, only further away in the noisy part of the objective function.

In the same way as the last section, a comparison of the fitted semblance value allows to evaluate how successful the operators fitted the data. Since every operator has their slowness and time shifted version (see Chapter 2.3.5), it is necessary to investigate which representation is better suited for stacking. Figure 6.28 shows the semblance of slowness shifted nCRS as a reference and the difference plots of three exemplary chosen operators. In the difference plots, a red colour represents higher semblance values for the slowness shifted version whereas blue colours show higher semblance for the time shifted operator. Independent of the actual operator, the slowness shifted versions show a higher coherence almost everywhere and a better fit for the same events.

Figure 6.29 shows the semblance obtained by nCRS as well as difference plots of nCRS and the other operators in their slowness shifted version. Red colours represent a better fit for nCRS, blue colours for CRS, iCRS or multifocusing. The

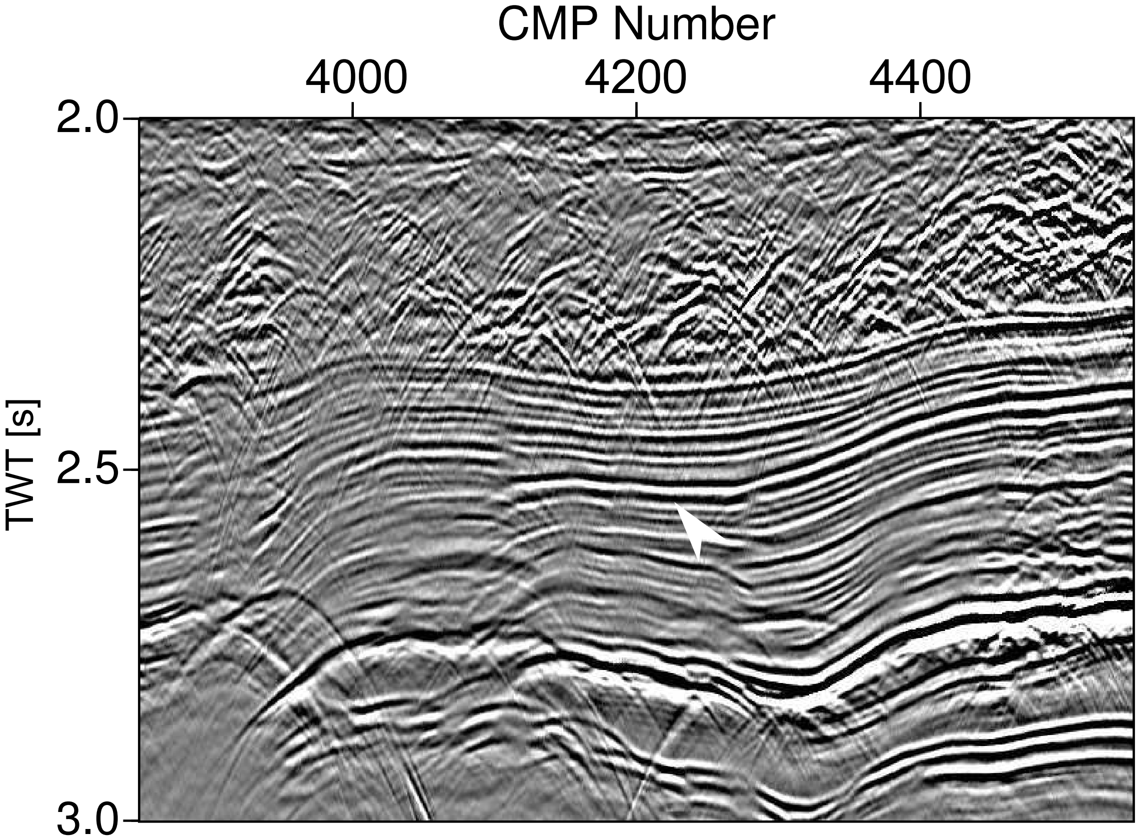

Figure 6.25.: Stacked section in the north east of the profile. The arrow indicates the location of the sample investigated in Figures 6.26 and 6.27.

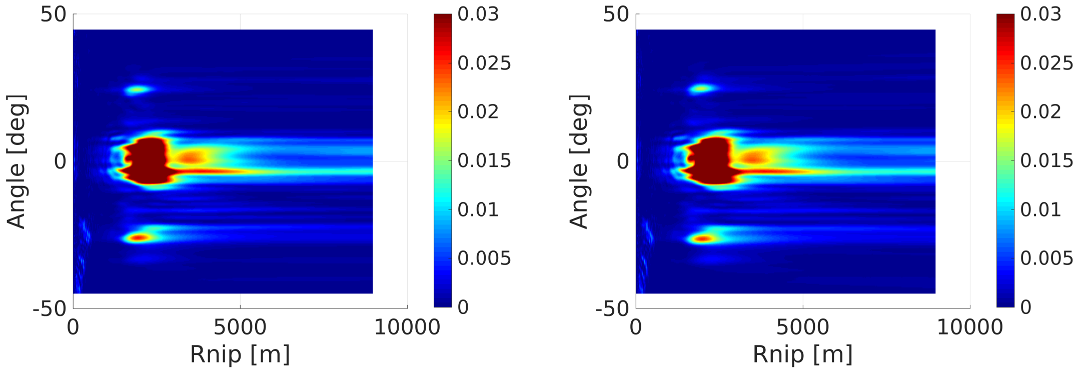

(a) Objective function of CRS (b) Objective function of multifocusing

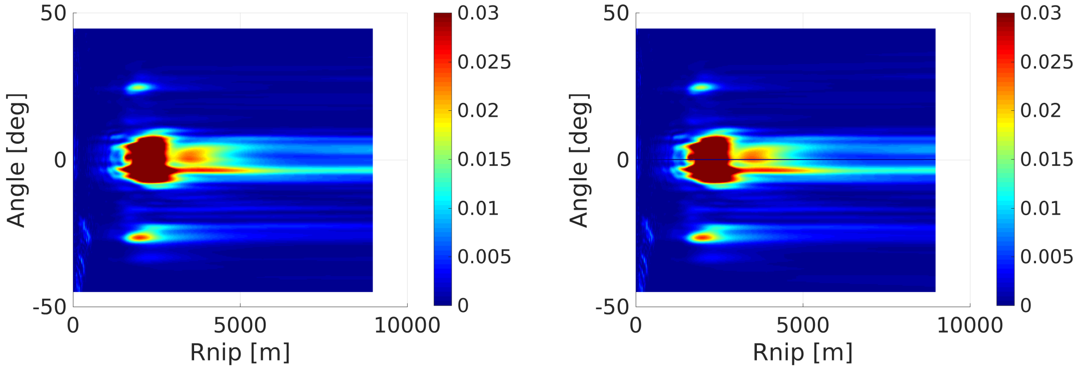

(c) Objective function of nCRS (d) Objective function of iCRS

Figure 6.26.: Objective function of the sample shown by an arrow in Figure 6.25. The offset-target ratio is 0.5 where a hyperbolic assumptions is still valid. Therefore, no differences between the non-hyperbolic operators and conventional CRS can be observed.

difference plots of nCRS minus iCRS and nCRS minus multifocusing show primarily white colours which means no significant differences are observable. In terms of accuracy they perform similarly on the marine field data. However, they show differences compared to the hyperbolic CRS represented by the difference plot of nCRS minus CRS. Differences for reflections are not visible, since those are white. In case of diffractions, mainly red colours appear which means a better fit for nCRS. Since the differences of nCRS to iCRS and multifocusing are almost nonexistent, the differences are the same for all non-hyperbolic operators compared to hyperbolic CRS. This is no surprise, since diffractions are higher order phenomena. The fit of diffractions is better for non-hyperbolic operators. This also shows in the estimated attributes, exemplarily shown for the moveout velocity in Figure 6.30. A reference velocity field, estimated using nCRS and difference plots of nCRS minus CRS, iCRS and multifocusing are shown. Red colours show a higher moveout velocity of nCRS while blue colours show higher moveout velocities for the other operators. The

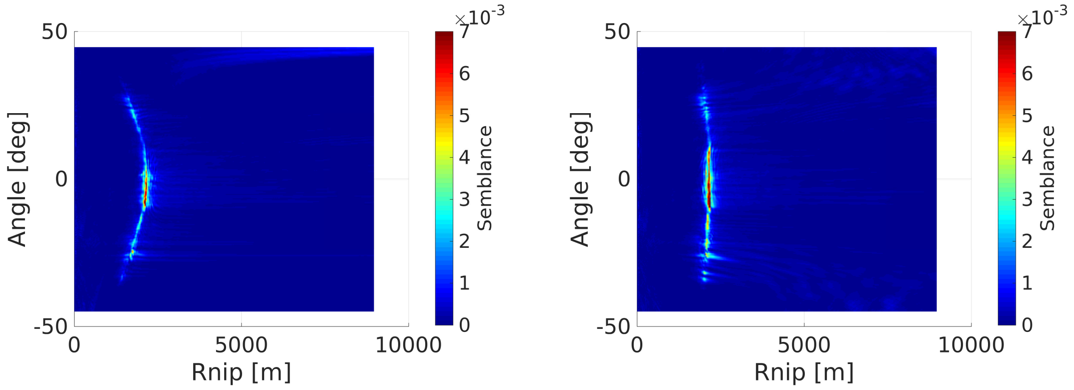

(a) Objective function of CRS (b) Objective function of multifocusing

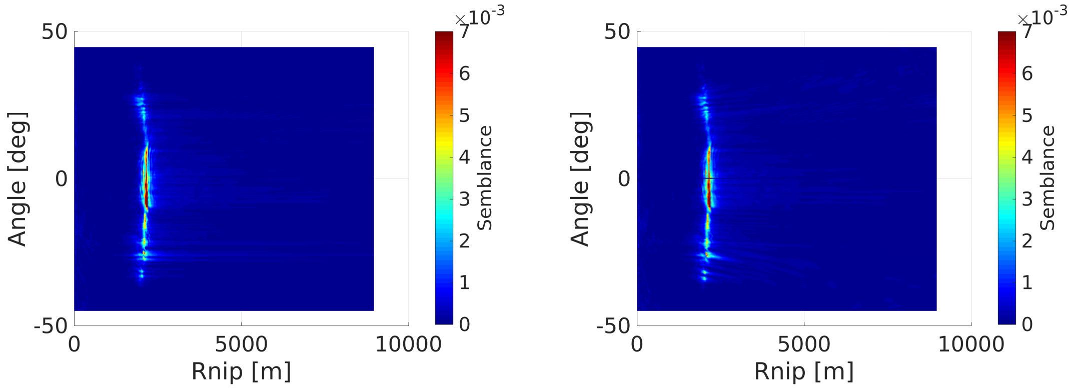

(c) Objective function of nCRS (d) Objective function of iCRS

Figure 6.27.: Objective function of the sample shown by an arrow in Figure 6.25. The offset-target ratio is 2.0 which exceeds the hyperbolic limit significantly. Therefore, the objective function of the conventional CRS operator differs severely from the non-hyperbolic variants. The difference between the individual non-hyperbolic expressions however, is negligible.

biggest differences are visible for nCRS minus CRS. In case of diffractions, CRS shows higher moveout velocities close to the apex while at the diffraction tail, nCRS shows higher moveout velocities, which seems more accurate because the semblance of nCRS is higher. Non-hyperbolic CRS and multifocusing show very similar moveout velocities apart from areas of very low coherence. Interestingly, even though the differences in the coherence between nCRS and iCRS are almost nonexistent, the moveout velocities show small differences. For dipping events, the moveout velocity of iCRS is higher than for nCRS. Unfortunately it is impossible to evaluate, which is more accurate. Therefore, the obtained velocities should be used carefully.

The observation, that non-hyperbolic operators perform better in case of diffractions

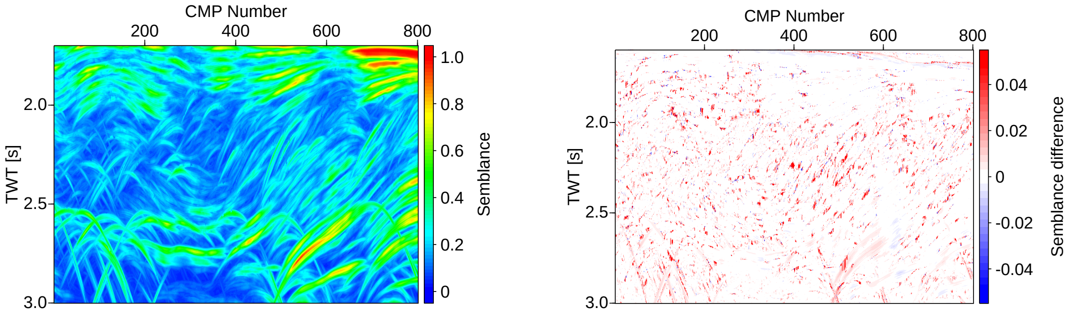

(a) nCRS reference semblance (b) CRS

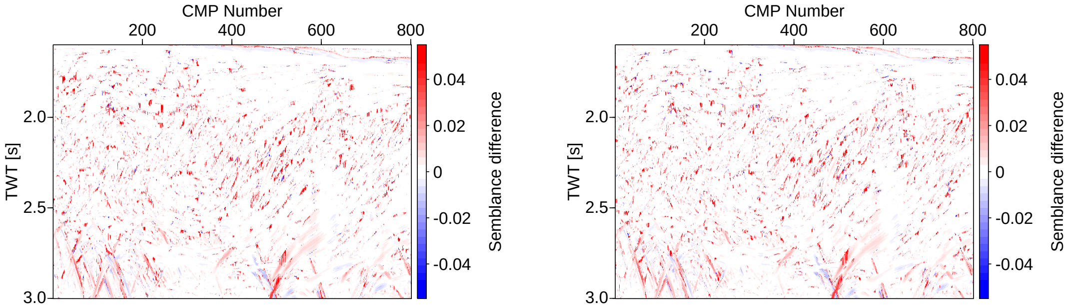

(c) Multifocusing (d) nCRS

Figure 6.28.: Semblance section obtained by the slowness shifted nCRS operator and difference plots of slowness shifted operators to their time shifted counterparts. A red colour indicates a higher semblance for the slowness shifted operator, while blue colours indicate a better semblance of time shifted operators.

than hyperbolic CRS, is further supported by a diffraction separation shown in Figure 6.31. An excerpt of the diffraction separation using nCRS and CRS is compared on the right hand side. The excerpt area is highlighted by the red box. In case of nCRS, more diffractions become visible and are more continuous. The arrows highlight diffractions where this can be observed in particular. Therefore, the results obtained in previous sections, particularly for diffractions, can be improved using one of the higher order non-hyperbolic operators.

Figure 6.32 shows a comparison of the computational cost of the compared operators. The additional computational overhead of the slowness shifted nCRS is very small (about 5 %) while the better accuracy for diffractions and lower sensibility with respect to the aperture are strong benefits. Depending on the task, nCRS shows the best trade-off between accuracy, stability and computational effort.

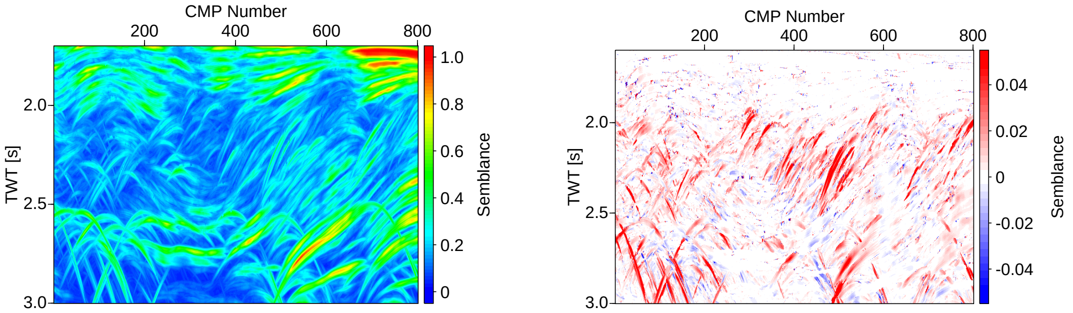

(a) nCRS reference semblance (b) nCRS - CRS

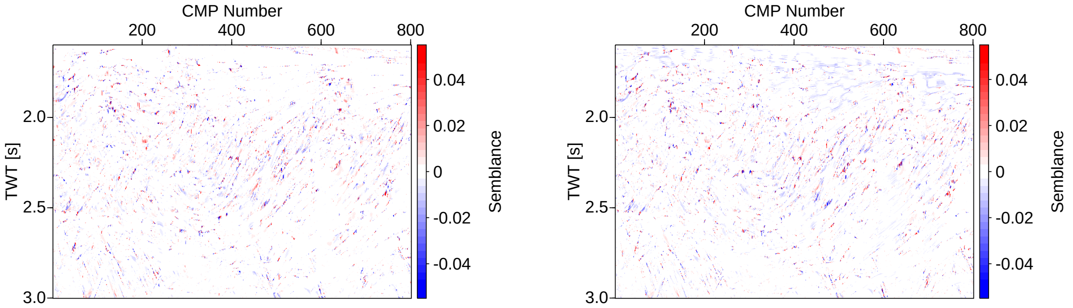

(c) nCRS - MF (d) nCRS - iCRS

Figure 6.29.: Semblance section obtained by the slowness shifted nCRS operator and difference plots of slowness shifted nCRS to the other slowness shifted CRS-type operators. A red colour indicates a higher semblance for the slowness shifted nCRS operator, while blue colours indicate a better semblance the other slowness shifted operator.

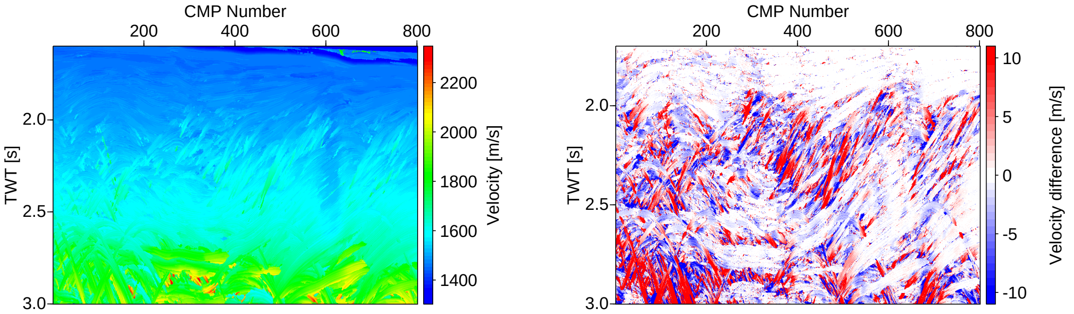

(a) nCRS reference velocity

(b) nCRS - CRS

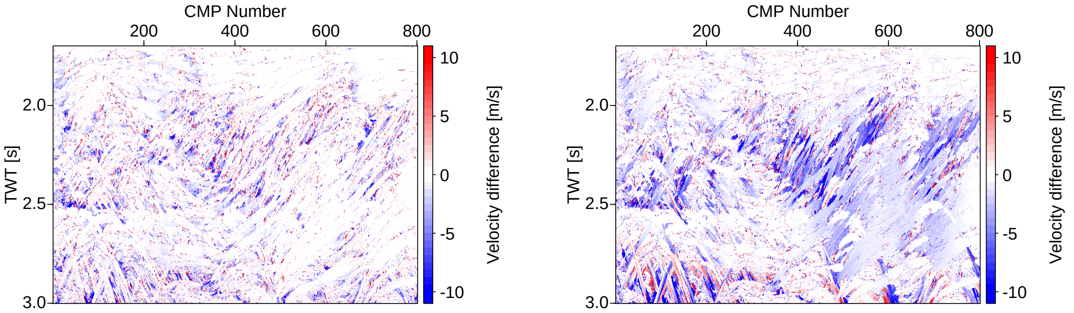

(c) nCRS - MF

(d) nCRS - iCRS

Figure 6.30.: Comparison of the estimated moveout velocities obtained by the different operators. The results from nCRS serve as reference for difference plots, since the differences are small. A red colour indicates a velocity for the slowness shifted nCRS operator, while blue colours indicate a lower velocity compared to the other slowness shifted operator.

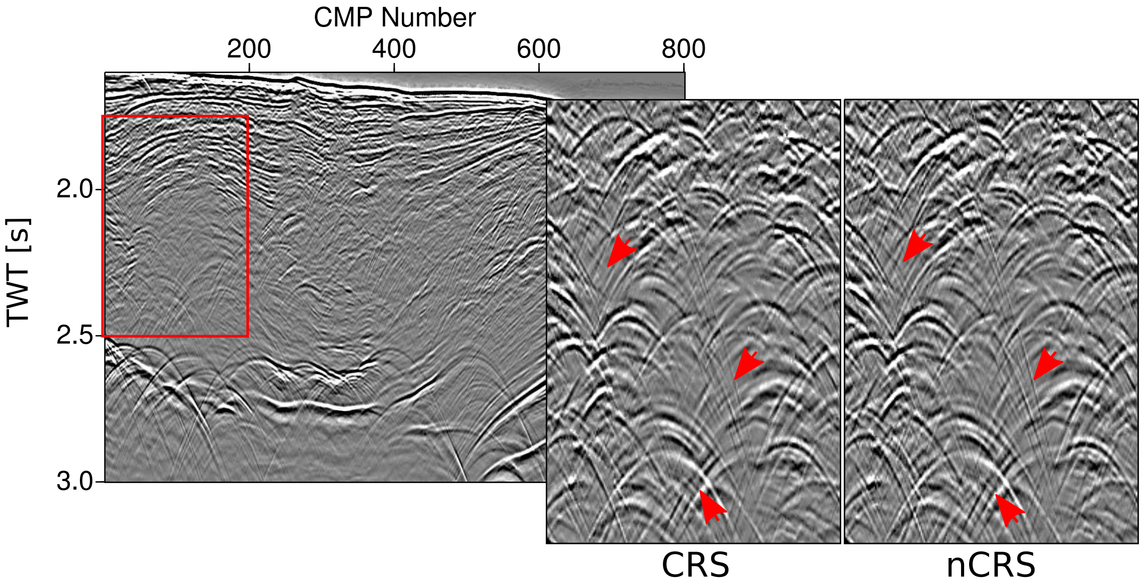

Figure 6.31.: Stacked section of the fault system. The red box shows the excerpt shown on the right, where a diffraction separation is performed using attributes obtained by the CRS and nCRS operators. Red arrows indicate improvements achieved by nCRS compared to CRS. Multifocusing and iCRS are not shown since they performed similar to nCRS.

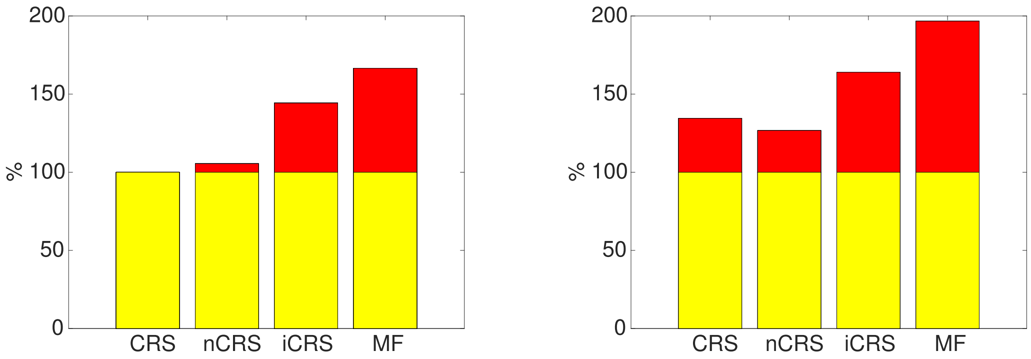

(a) Slowness shift

(b) Time shift

Figure 6.32.: Comparison of the computation time for each operator in their slowness (a) and time shifted version (b). The hyperbolic CRS in the slowness shifted version is the reference (100 %). The yellow colour represents the calculation time of CRS while the red colour is the additional computational cost of the corresponding operator.

Chapter 7.

Land data

The data set was acquired within the DOBREflection 2000 project by the Ukrainian national oil company Ukrgeofisika in 2000 and crosses the Donbas Foldbelt next to the Dniepr-Donets basin (Figure 7.1). The data was processed before by Menyoli et al. (2004) using the CRS method. In their work they did not account for conflicting dips. An interpretation of the deep seismic profile can be found in the work of Maystrenko et al. (2003). Structures like outcrops which indicate an inversion of the Donbas Foldbelt are shown in Saintot et al. (2003). The processing parameters for the CRS parameter estimation used in the CRS workflow are listed in Table 7.1. Table 7.2 shows the apertures used for zero-offset and partial stacks.

7.1. CRS stack

The data set was acquired within the DOBREflection 2000 project by the Ukrainian national oil company Ukrgeofisika. The profile crosses the Donbas Foldbelt next to the Dniepr-Donets basin (Figure 7.1) from the south east to the north west. The maximum offset is 12,800 m. In contrary to sedimentary data, hard rock data has a lower signal-to-noise ratio caused by mining and heterogeneity of rocks hosting mineralization. This leads to discontinuous reflections and diffractions (Górszczyk et al., 2015).

The data was processed before by Menyoli et al. (2004) using the CRS method. In their work they did not account for conflicting dips. An interpretation of the deep seismic profile from CMP processing can be found in the work of Maystrenko et al. (2003). Structures like outcrops which indicate an inversion of the Donbas Foldbelt are shown in Saintot et al. (2003).

The stacks image the Moho (Figures 7.2, 7.3 and 7.4), the Ukrainian shield (Figures 7.5, 7.6 and 7.7) and the beginning of the Donbas Foldbelt (Figures 7.8, 7.9 and

General parameters	
Dominant frequency	30 Hz
Coherence measurement	Semblance
Coherence time window	44 ms
Velocity constraints	
Near surface velocity	4213 m/s
Lower velocity variation from guide function	20 %
Upper velocity variation from guide function	20 %
Search apertures	
Minimum midpoint aperture	300 m at 0 s
Maximum midpoint aperture	500 m at 10 s
Minimum offset aperture	2000 m at 0 s
Maximum offset aperture	10000 m at 10 s
Conflicting dip handling	
Number of dip intervals	17
Dip intervals in °	[-90,-30], [-30,-20], [-20,-12.5], [-12.5, -7.5], [-7.5,-4], [-4,-2], [-2,2], [2, 4] ,[4,7.5], [7.5,12.5], [12.5,20], [20,30], [30,90]
Global optimization parameters	
Algorithm	Differential evolution
Number of individuals	20
Crossover probability	74.55 %
Differential weight	0.9362
Minimum number of iterations	30
Maximum number of iterations	200
Number of allowed stagnated iterations	10
Local optimization parameters	
Lower coherence threshold	1.00 at 0 s
Upper coherence threshold	1.00 at 15 s
Maximum Number of iterations	100
Minimum deviation required	10^{-4}
Transformation radius of R_N	100 m
Initial variation of emergence angle	2 °
Initial variation of R_{NIP}	3 %
Initial variation of R_N	2 °

Table 7.1.: Search parameters for the land data. No local optimization was performed.

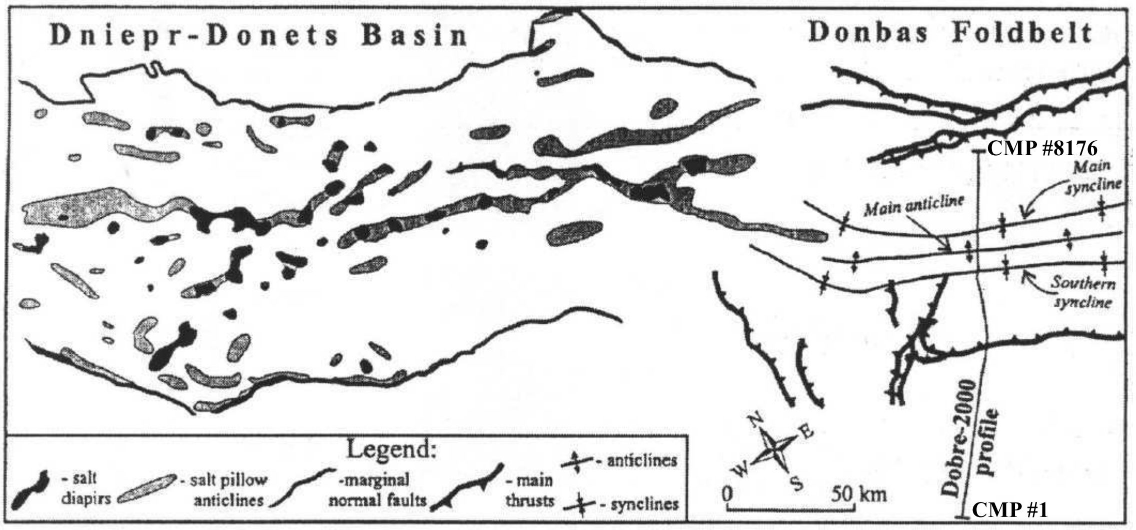

Figure 7.1.: Location of the profile after Menyoli et al. (2004).

Stacking parameters	
Minimum midpoint aperture	300 m at 0 s
Maximum midpoint aperture	500 m at 10 s
Minimum offset aperture	2000 m at 0 s
Maximum offset aperture	10000 m at 10 s

Partial stacks	
Regularized receiver interval	35 m
Minimum local midpoint aperture	50 m at 0 s
Maximum local midpoint aperture	150 m at 10 s
Local offset aperture	50 m

Table 7.2.: Stacking parameters for the land data.

7.10). The CMP stacks, especially, contain a lot of noise. The most prominent events are visible, however deeper events like the Moho in Figures 7.2, 7.3 and 7.4 are barely recognizable. The nCRS stacks reduce the noise significantly but also introduce a smearing of events. Furthermore, they enhance strongly coherent dipping noise, indicated by white arrows in Figure 7.3. However, when considering conflicting dips, nCRS stacks attenuate the coherent dipping noise, do not introduce smearing, but still show an improved signal-to-noise ratio (Figure 7.4). Therefore, subsurface events become more apparent and can be followed continuously which becomes important, e.g., for horizon tracking.

The conventional CRS without conflicting dip treatment seems to generate least noisy images. However, these images should be considered with care since not every apparent event is desired as demonstrated in Figures 7.2, 7.3 and 7.4 for the Moho. White arrows mark events in the stack with conflicting dips (Figure 7.4) that were previously masked by steep dipping coherent noise in Figure 7.3. In the excerpt of the data, that images the Ukrainian shield, small structures marked by white arrows in Figures 7.5, 7.6 and 7.7 are smeared and masked when conflicting dips are not considered. This is also the case for the shallower sediments at the beginning of the Donbas Foldbelt, where the data is of better quality (Figure 7.8, 7.9 and 7.10). As before we also observe masked events in this part of the data that we could not see with conventional CRS processing. This behaviour is of particular importance when prestack data enhancement (Baykulov and Gajewski, 2009) is performed, which can achieve considerable improvements in quality on poor data like this. For this method, the CRS wavefront attributes are required. However, if performed with conventional CRS processing, valuable information gets lost since the attributes are only available for the most dominant event, which might not be the desired event as our results show. Since the presented workflow provides attributes for all events that are imaged in the stacked sections, the regularized interpolated and therefore enhanced data will contain those events as well, which is important for follow up applications like time or depth migration.

Our results show that CRS with appropriate conflicting dip handling can suppress coherent steep dipping noise very effectively, which can be observed in various data. This improves identification and interpretation of horizons severely. Since we simply apply CRS for specific dip clusters, the same principle can also be applied to 3-D data. However, the computational cost becomes much higher as well, since 3-D CRS would need to be applied for dip and azimuth clusters.

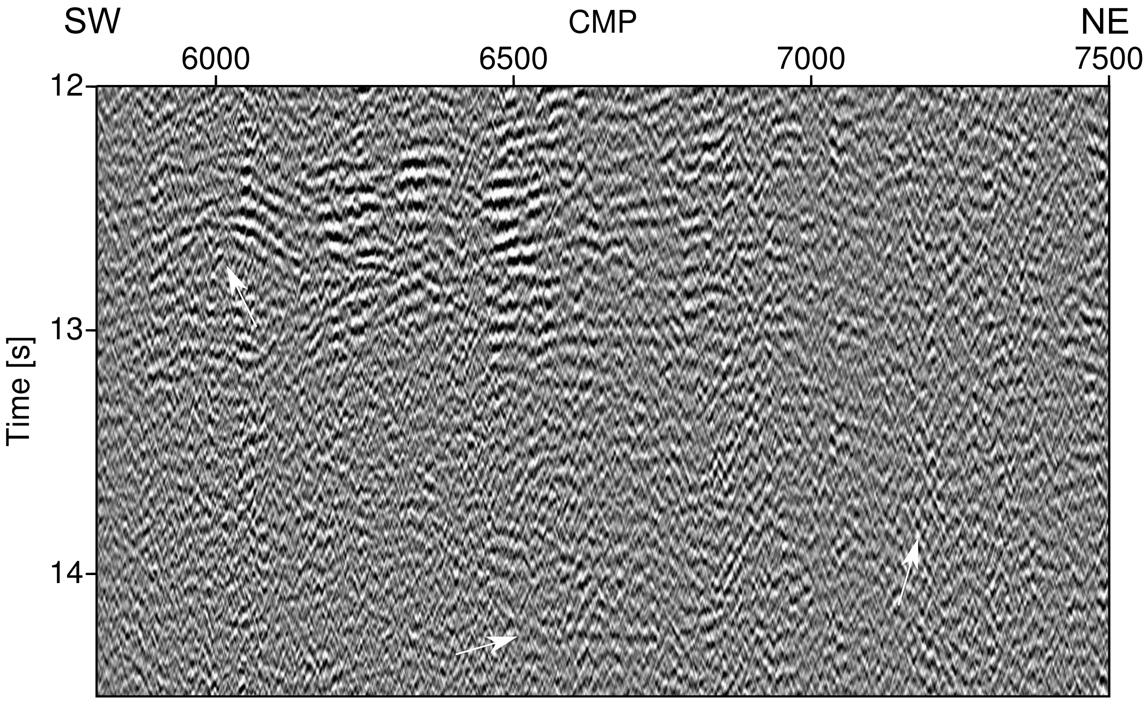

Figure 7.2.: Conventional CMP stack of an excerpt of the Moho.

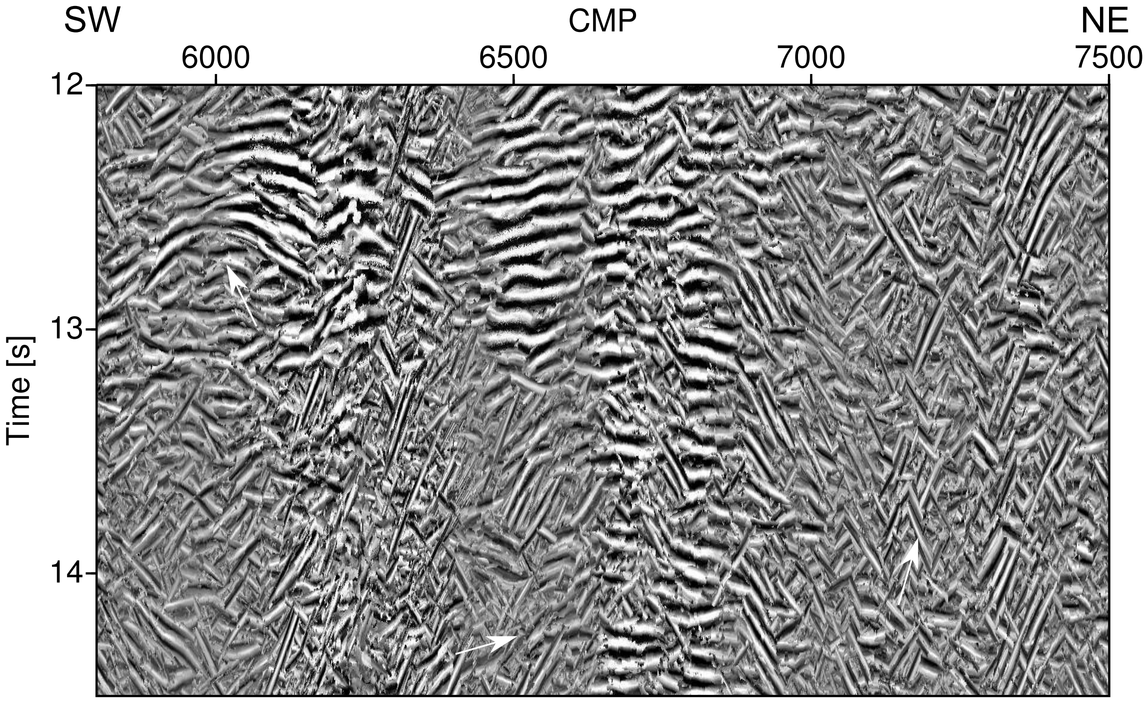

Figure 7.3.: Conventional nCRS stack of an excerpt of the Moho. Steep events seem truncated.

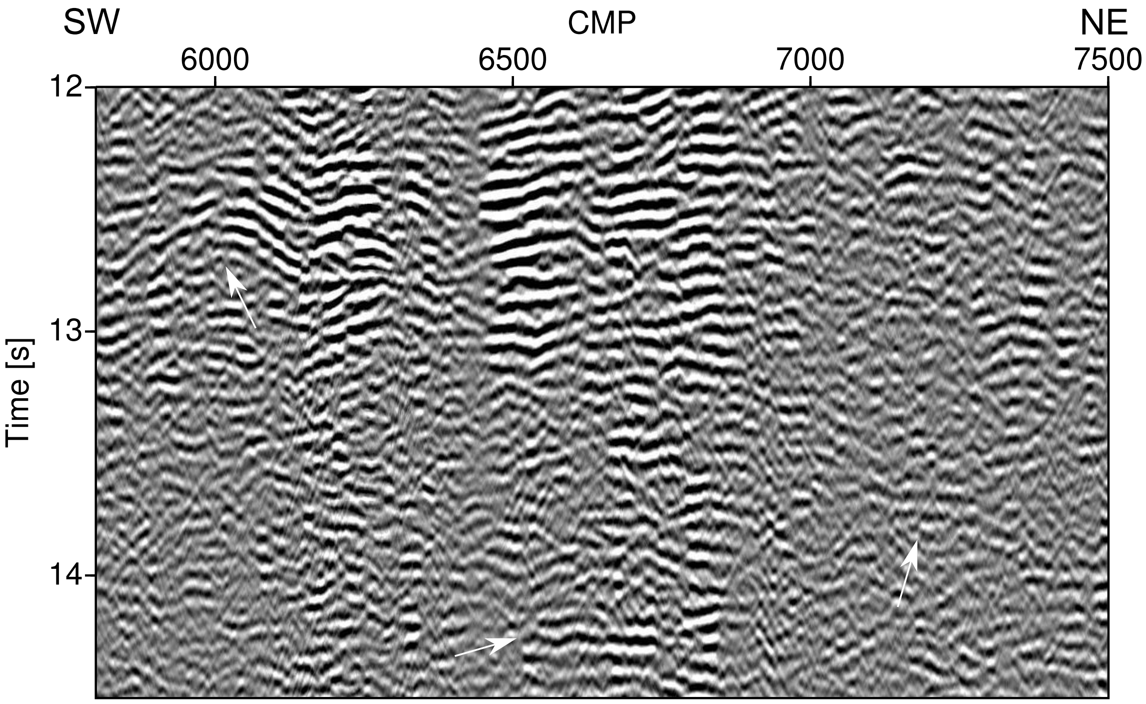

Figure 7.4.: Improved nCRS stack of an excerpt of the Moho using conflicting dip processing. Events seen in Figure 7.2 can be identified as noise and masked events become visible.

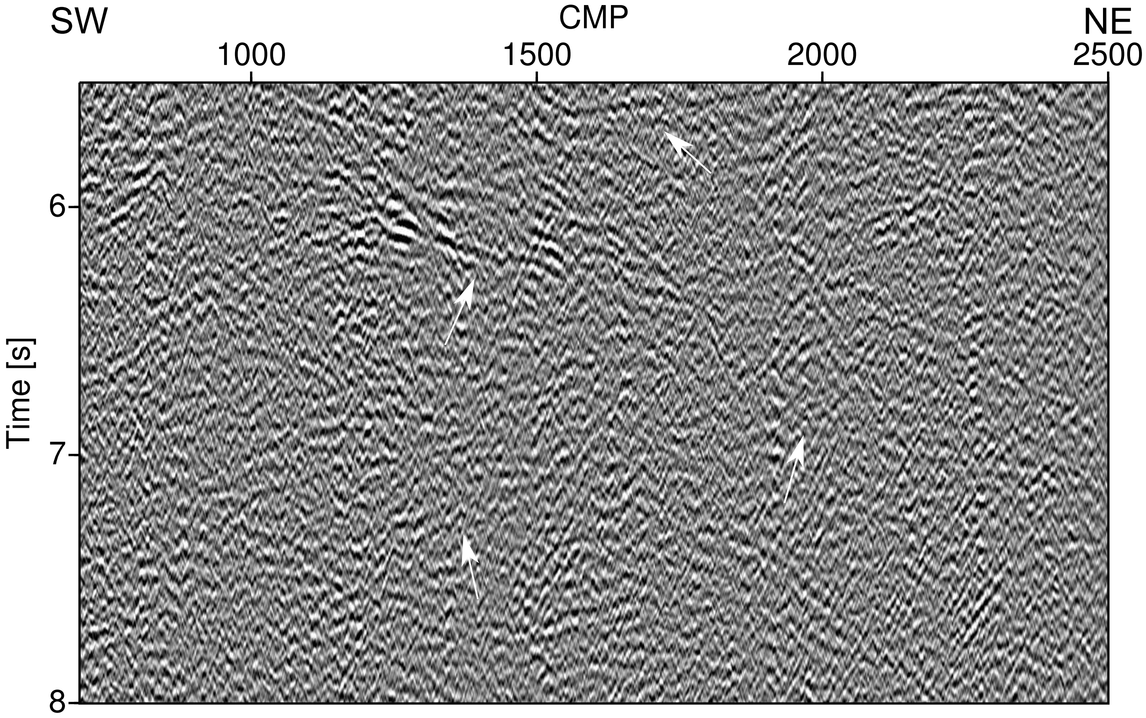

Figure 7.5.: Conventional CMP stack of an excerpt of deeper parts of the Ukrainian Shield in the south west of the profile.

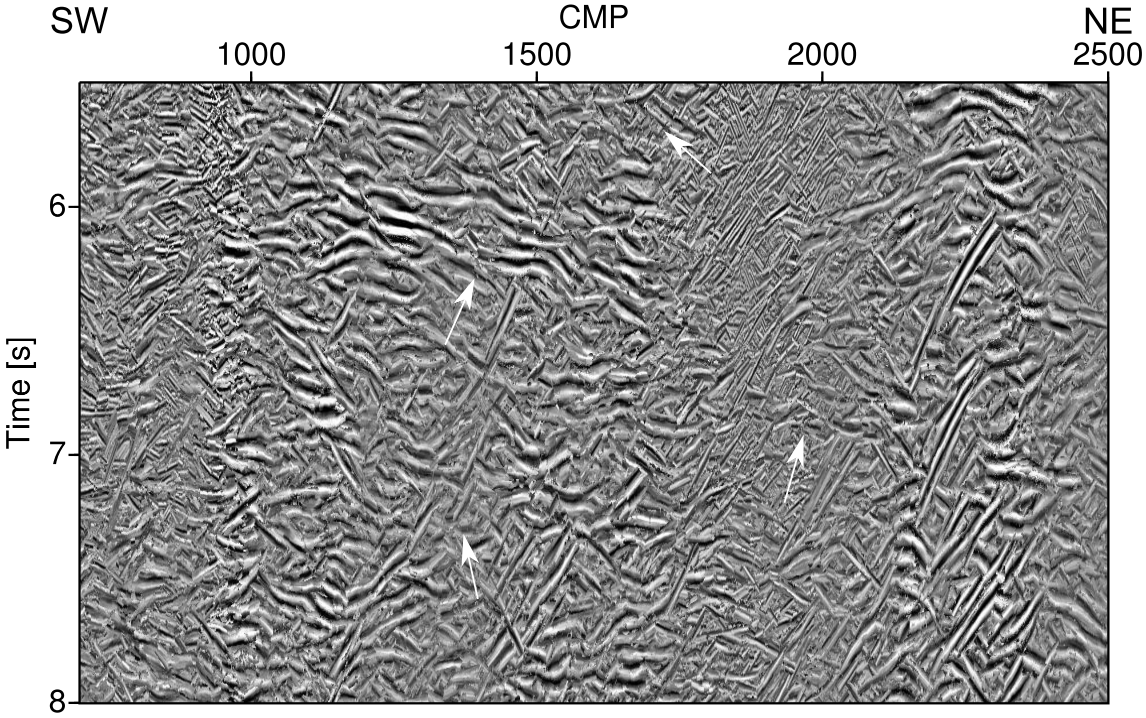

Figure 7.6.: Conventional nCRS stack of an excerpt of deeper parts of the Ukrainian Shield in the south west of the profile.

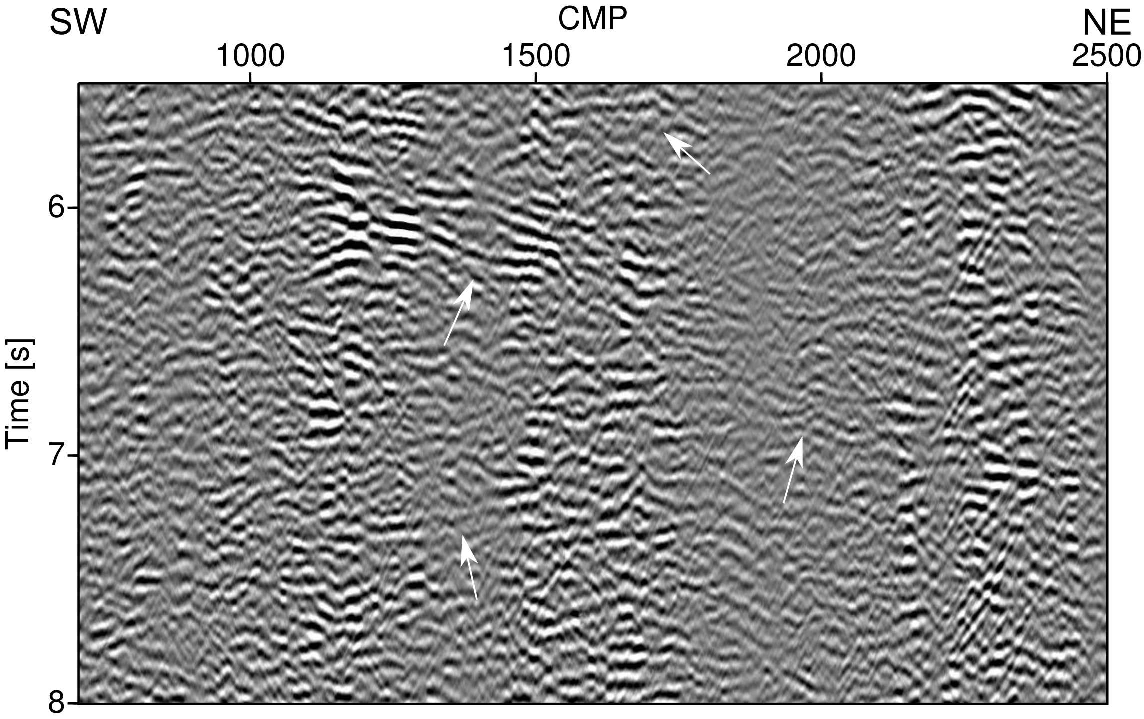

Figure 7.7.: Improved nCRS stack of an excerpt of deeper parts of the Ukrainian Shield in the south west of the profile.

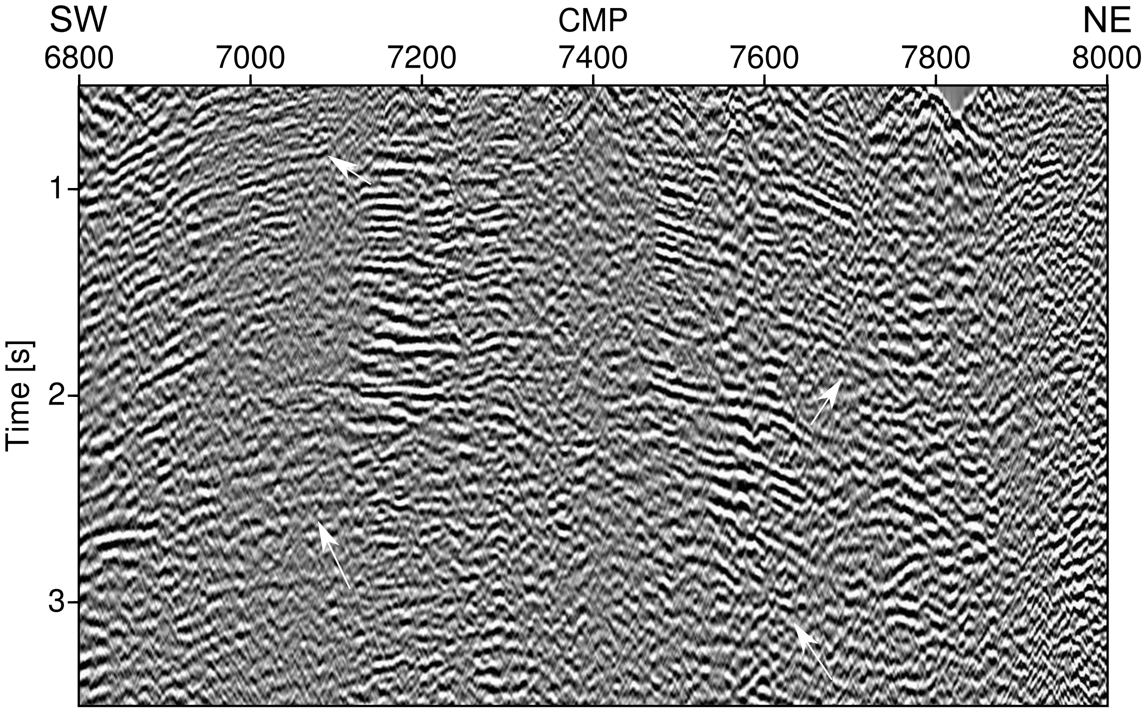

Figure 7.8.: Conventional CMP stack of the south west of the Donbas Foldbelt in the north east.

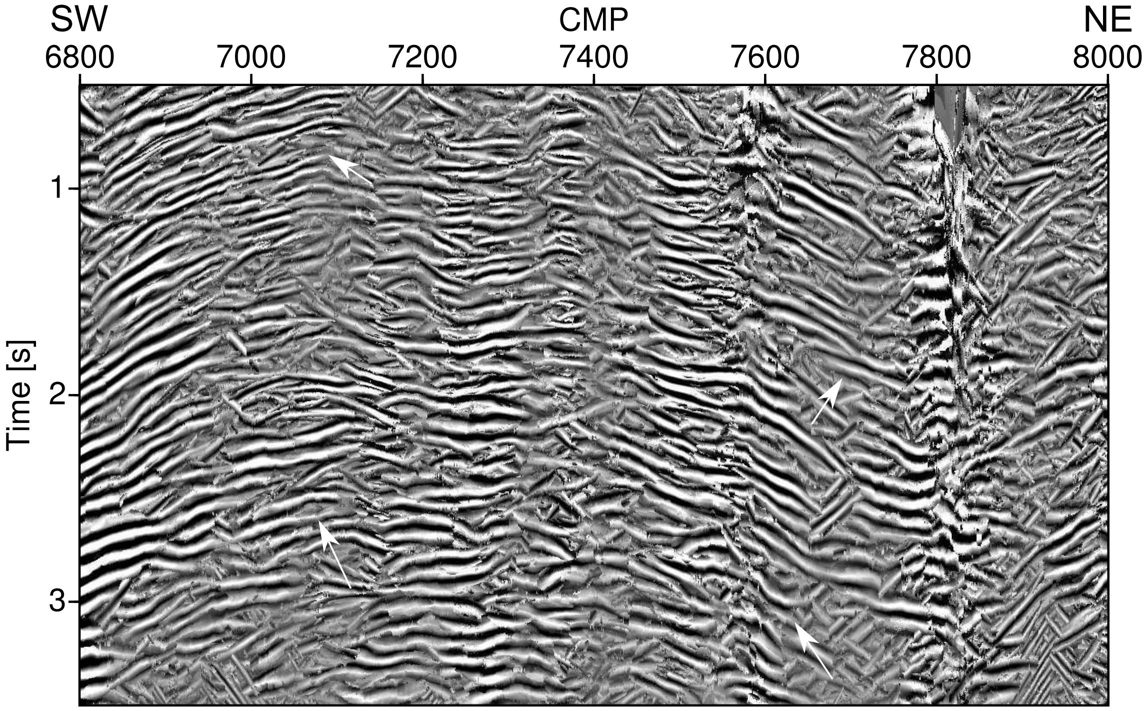

Figure 7.9.: Conventional nCRS stack of the Donbas Foldbelt in the north east.

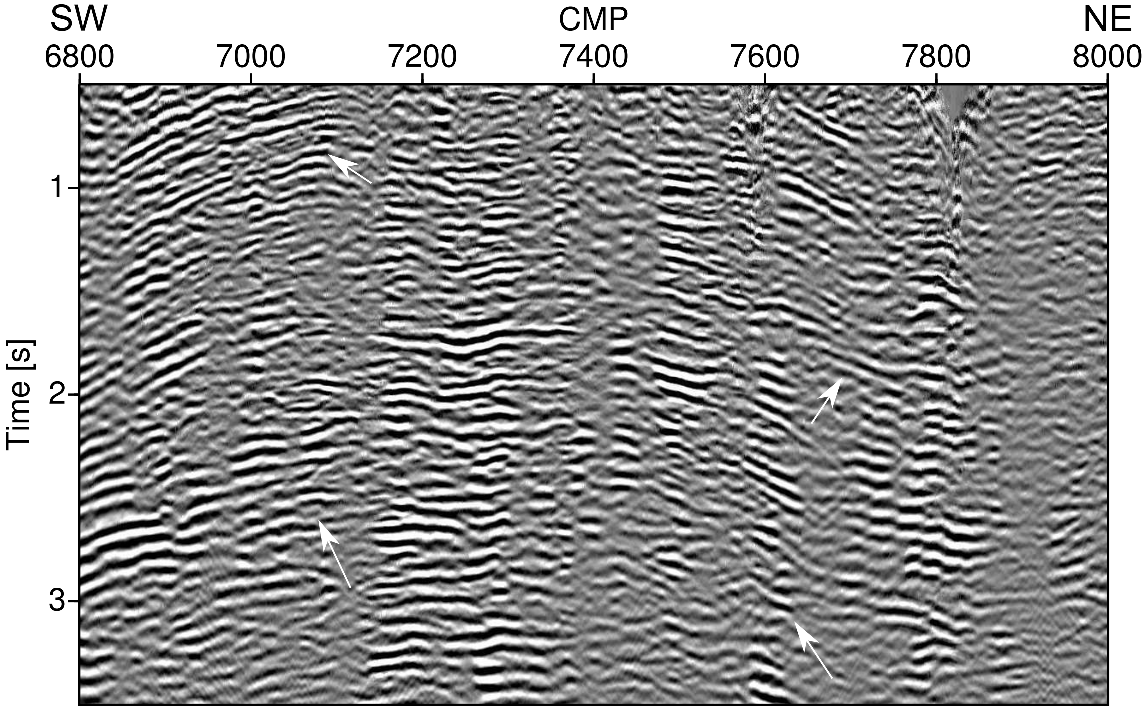

Figure 7.10.: Improved nCRS stack of the Donbas Foldbelt in the north east.

7.2. Data enhancement

Data enhancement in noisy land data is more important than in marine data since the data is of poor quality. This is especially important to obtain a reliable velocity model for, e.g., stacking or migration. The CMP gather for CMP 6486 in the middle of the Donbas Foldbelt in the north east of the profile is shown in figure 7.11. Compared to the CMP gather of the original data (Figure 7.11(a)), the enhanced CRS gather obtained without conflicting dip processing, shown in Figure 7.11(b), shows artificial low frequency noise in the middle and lower part of the CRS gather which is not visible in the CRS gather obtained by conflicting dip processing (Figure 7.11(c)). Furthermore, starting at 5 s, horizontal and dipping high frequency events appear in the CRS gather without conflicting dip processing. Those can also be seen in the corresponding frequency sections in Figure 7.12. The frequency content of the original CMP gather is shown in Figure 7.12(a). The CRS gather without conflicting dip processing (Figure 7.12(b)) changes the frequency content dramatically. Between 30 and 40 Hz is an additional plateau visible, that was not apparent before. A correct treatment of conflicting dips in the CRS framework (Figure 7.12(c)) however, does not change the frequency content, it just enhances the respective energy content as desired.

A velocity spectrum of CMP 6486 from the Donbas Foldbelt is shown in Figure 7.13. The velocity spectrum in the original CMP gather (Figure 7.13(a)) shows reliable maxima in the sedimentary part up to 4 s. In the crystalline part below, no reliable picks can be made. The enhanced CRS gather in Figure 7.13(b) shows the same spectrum obtained from data enhancement by partial CRS without conflicting dip handling. Maxima are better distinct and a few events in the crystalline rock can be picked. However, compared to Figure 7.13(c) where the proposed dip decomposition was applied, events are missing, especially at about 6 and 10 s. The maxima obtained by enhanced CRS gather show a higher semblance and can be picked more precisely than in the CMP gather, especially in the deeper part of the data which contains of crystalline rocks and the Moho at roughly 12.5 s.

In the next chapter, I conclude and discuss the results obtained.

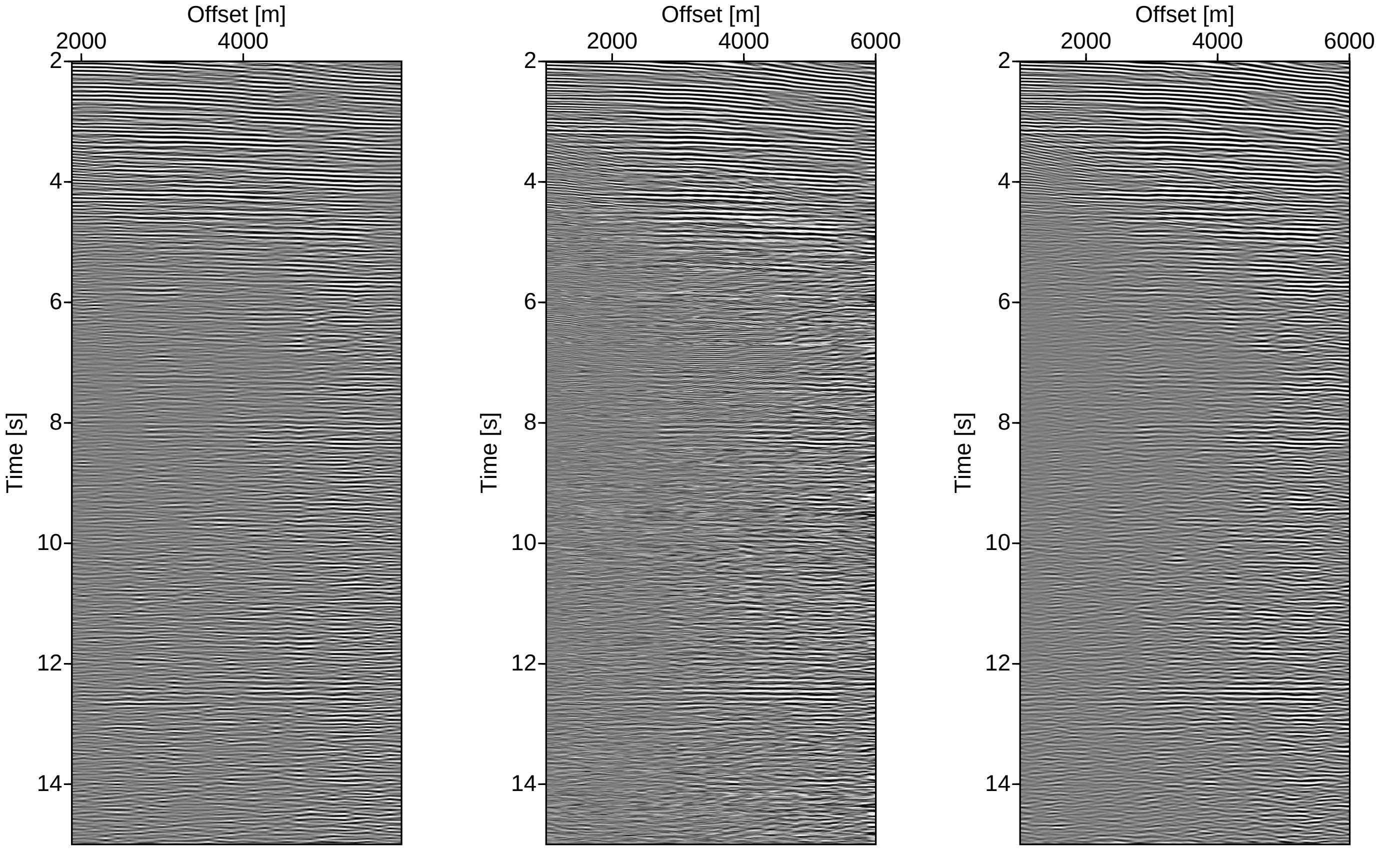

(a) CMP gather of original data

(b) CRS gather

(c) CRS gather with conflicting dips

Figure 7.11.: CMP gather from the Donbas Foldbelt from offsets of 1000 m to 6000 m. The offset for the original data (a) starts at 1890 m due to missing traces in acquisition for this CMP. Events in the enhanced data (c) are better recognizable and contains more and regularized traces. Furthermore, events are not truncated as in (b) but interfere with other events constructively and destructively.

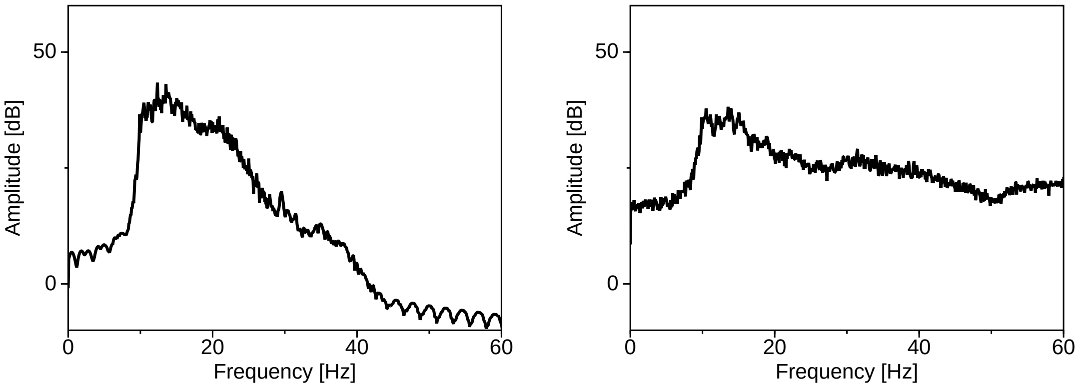

(a) Spectrum of original CMP gather

(b) Spectrum of CRS gather

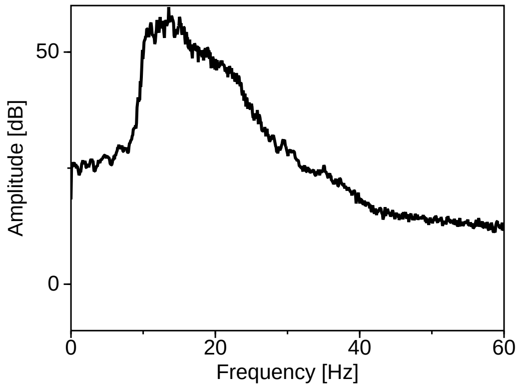

(c) Spectrum of CRS gather with conflicting dips

Figure 7.12.: Spectra of the CMP 6486 shown in Figure 7.11. The original frequency content (a) is changed by CRS without conflicting dip handling (b), while CRS with conflicting dip handling (c) just enhances the energy.

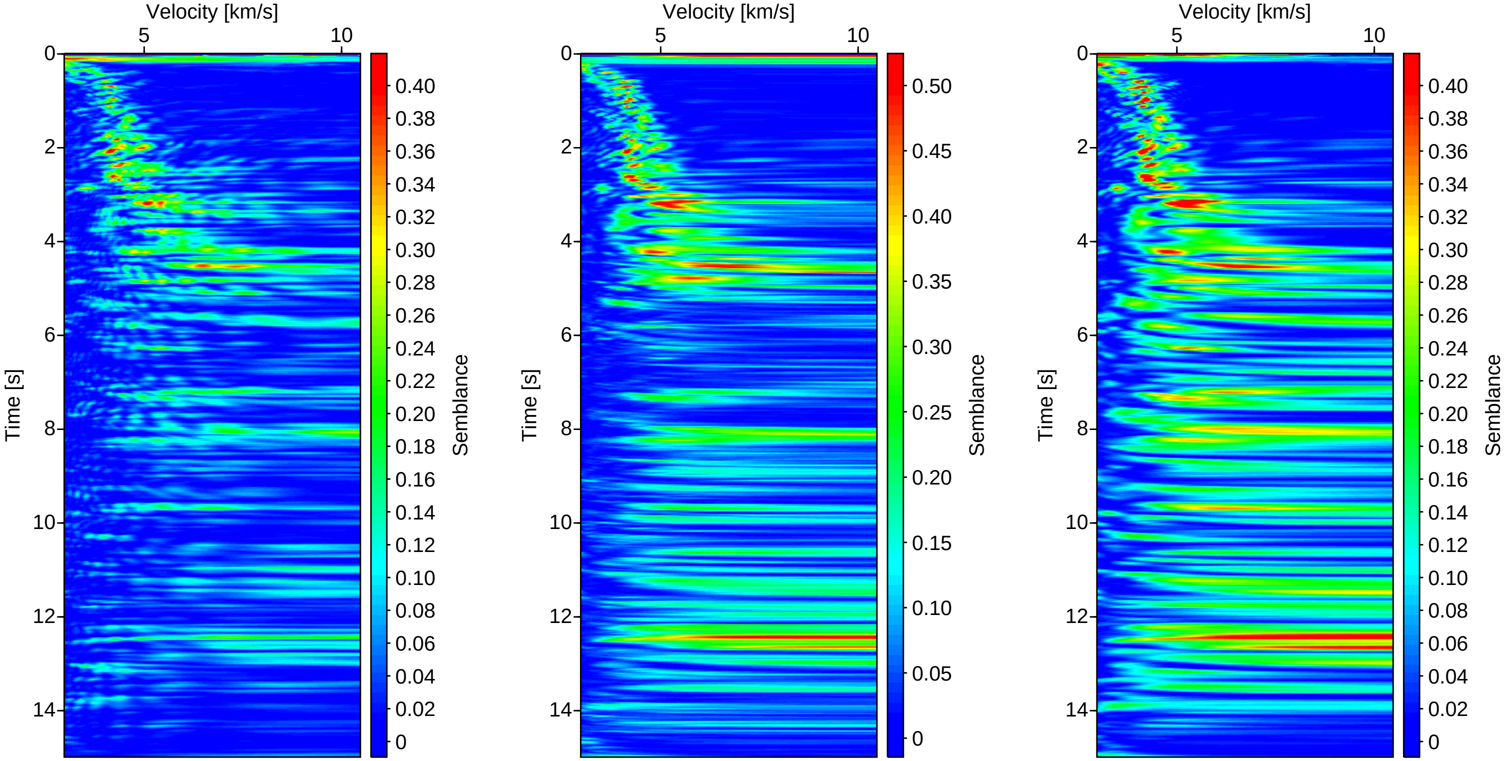

(a) Velocity spectrum of original data (b) Velocity spectrum of enhanced data (c) Velocity spectrum of enhanced data

Figure 7.13.: Velocity spectra used for velocity analysis. The enhanced data (b) and (c) show better peaks with more distinct maxima, especially in the deeper parts of the data. However, some events in (b) are missing.

Chapter 8.

Conclusions

As mentioned in the introduction the main aim of this thesis is to propose a reliable workflow that incorporates conflicting dip processing in the CRS framework without the necessity of a lower data redundancy or simplified operators while preserving the possibility of CRS attribute-based methods like data preconditioning. The developed workflow allows to do that without drawbacks, except a higher computational cost compared to most previously existing methods. The extended pragmatic approach shows areas on synthetic data where the conflicting dip treatment was not successful. An application to more complex field data is therefore not promising. The common-diffraction-surface method deals with a signal stretch which is equivalent to a change in the frequency content. This destroys amplitude information and loses valuable subsurface information. Furthermore, many operators have to be determined, leading to a very expensive method.

The obtained results from the proposed method show tremendous improvements for complex synthetic, marine and challenging land data. Moreover, the results from hard rock land data lead to the conclusion that the proposed method not only enhances the data quality but also preserves the frequency content, making it amplitude friendly which means it does not destroy amplitude information during the process, even in a very noisy environment.

An important reason for such improvements are the use of the full data redundancy, provided by the CRS method, during the parameter estimation. This is achieved by the adaption to a global optimization scheme, compared to a three step search strategy as before, which improves the quality of the estimated CRS wavefront attributes. The improved quality of the CRS wavefront attributes is also caused by the chosen algorithm called differential evolution which does not need a priori assumptions. However, a priori information can be used in the algorithm to improve its convergence. Since this algorithm is population based, it does not depend on a good initial solution as the previous method which further improves the stability and convergence of the parameter estimation algorithm.

The incorporation of conflicting dips is achieved by a simple partitioning of the search space along the angle dimension. This has two major benefits, a smaller search space for the parameter estimation, further increasing its stability, and a detected maximum in each cluster. Stacking all cluster results in the interference of the found events which leads to proper treatment of conflicting dip situations as the applications have shown.

Investigations of the available operators in literature that can be parametrized by the CRS wavefront attributes show, that in general a non-hyperbolic operator should be used rather than the hyperbolic CRS. They can be fitted more accurately and depend less on the choice of aperture. Which specific operator should be used in terms of accuracy cannot be answered since multifocusing, iCRS and nCRS perform similarly in that aspect. However, if computational costs matter, nCRS uses less time since the function evaluation is not as expensive as in iCRS and multifocusing who require additional computations such as focusing parameter or calculation of the reflection angle.
Every operator can be formulated using a slowness or time shift. The comparison shows that slowness shifted versions perform better computationally and lead to a more accurate fit. Since multifocusing is written in the time shifted version in literature, it is recommended to transform it into its slowness shifted version to obtain a better performance. However, slowness shifted nCRS provides the best trade-off between accuracy and computational cost.

In the land data, high dipping events are present in the whole data set. In this case, they are most likely noise, even though they also might be interpreted as diffractions. However, the investigation of pure noise data has shown, that CRS can fit diffractions in noise as well. Therefore, apparent diffractions in noisy data should be taken with care and need further investigation in order to be able to decide, whether they are truly diffractions or not.

The benefits of the proposed method can be used in existing CRS wavefront attribute-based methods shown exemplary by data enhancement, diffraction separation, time migration and velocity model building. In case of time migration, each dip cluster provides a velocity field. The combination of those velocities, with the corresponding semblance to decide whether they come from actual events or noise, allows to improve the automatically obtained velocity field for complex regions, i.e. salt body.
In principle, the proposed approach to handle conflicting dip situations does not even require a change in existing software. An application of existing CRS software with the appropriate parameter limitations lead to the same results apart from the quality of the attributes. This depends on the implementation and choice of the search algorithm. Therefore, the method is immediately available without a necessity of new software which is a significant benefit.

Chapter 9.

Outlook

Usually, the extension of a method to 3-D is rather complicated. Fortunately, the proposed method is simple to extent. The major difference is, rather than choosing pure dip cluster, dip and azimuth cluster need to be build. This requires more operators, which are also more expansive to determine since more traces are involved and eight instead of three attributes need to be estimated. Since azimuth and dip information are used in 3-D, only a few dip cluster should be required in dip and azimuth direction. The chance of intersecting events from similar dips and azimuths is low. The success of the correct treatment of conflicting dips in 3-D also depends on the azimuth coverage. Conflicting dip treatment for narrow azimuth data will be similar to the 2-D case, since very few azimuths are available. Therefore, more dip cluster and less azimuth cluster need to be determined. In case of wide and/or full azimuth data, more azimuths are available which yields the benefit of more available azimuth cluster, which reduces the necessity of a high number of dip cluster. An alternative solution might be to identify the global maximum, measure its extent in the search space and remove it. Afterwards a new search can be applied until all coherent maxima are found. The resulting discontinuous search space can be handled by the differential evolution algorithm making this approach in principle viable.

The search algorithm, used within the thesis, is straightforward to extent and was successfully applied to much higher dimensions than eight (Pedersen (2010)) as in 3-D ZO CRS. The main issue is the computational cost and the relatively high amount of function evaluations required. A solution can be the combination of DE with a local optimization scheme, accelerating the convergence.

The obtained dip corrected velocity field can not only be used for migration as shown in this thesis, but also demigration as suggested recently by Glöckner et al. (2016). In this work, only time processing is considered. However, the CRS wavefront attributes can also used to build an interval velocity model (Duveneck, 2004). Currently, this method is investigated more to incorporate informations stemming from diffractions in particular (Bauer et al., 2016b). This is not even restricted to active seismics. It can be used in passive seismics as well, shown by Schwarz et al. (2016). Furthermore diffractions contain valuable offset information, even in the ZO domain, which can make these approaches viable for other aspects like ground penetrating radar (Schwarz, 2015). The estimated attributes and the availability of CRS wavefront attributes for diffractions are crucial for these methods, which the proposed method provides. The merging of the proposed method and those ideas is ongoing research at the applied seismics group at the University of Hamburg.

Another interesting possibility is to use the developed method and apply it to converted ways, since a method based on CRS attributes is already available (Abakumov et al., 2012). However, an additional parameter is required, the ratio of the velocity of the primary V_p and the velocity of the shear wave V_s. Fortunately, differential evolution can be extended by a dimension easily, which not only allows to estimate the CRS wavefront attributes to account for converted waves, but also the V_p/V_s ratio. Applied iteratively, it would also reduce the impact of a constant V_p/V_s ratio assumption, since it can be updated at each iteration.
Diffractions play a major part in this thesis, therefore, the next section focuses on the use of this information for possible future applications.

9.1. Diffraction imaging

A diffraction separation is shown for the marine data within this thesis. An immediate question raised is: can this be used to do diffraction imaging?

Migration algorithms can be used on such data in order to focus the diffractions to provide an image of scattering points in the subsurface that can indicate faults or rough topography of subsurface structures like salt. Figure 9.1 shows a poststack time migrated image of diffraction separated data. In this case, a simple diffraction summation migration is used. Due to errors during the diffraction separation, artefacts appear which are suppressed by an applied dip filter in the frequency-wavenumber domain. Therefore, amplitude information are lost but the focused diffractions become easier to spot. Please note, the diffraction separation left reflection residuals in the data as previously shown in Figure 6.24. A comparison of the migrated diffractions with a poststack time migration of the full wavefield in Figure 9.2 shows that diffraction imaging can highlight major faults and improve the ability to spot and track them. However, this are just first tests to demonstrate the potential of diffraction imaging using the proposed CRS workflow. A recent work by Bauer et al. (2016a) introduces a method to obtain prestack diffraction data by traveltime decomposition, using CRS attributes. This is a promising technique for diffraction imaging which benefits from results obtained in this work.

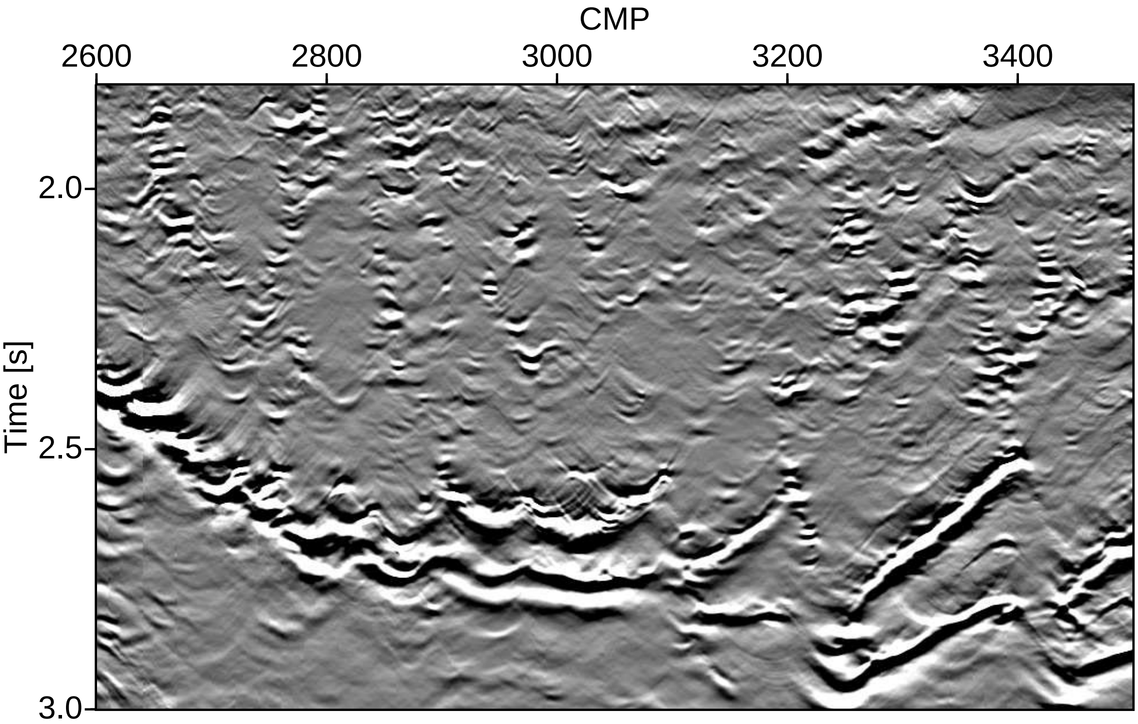

Figure 9.1.: Poststack time migration of diffraction only data from Figure 6.24.

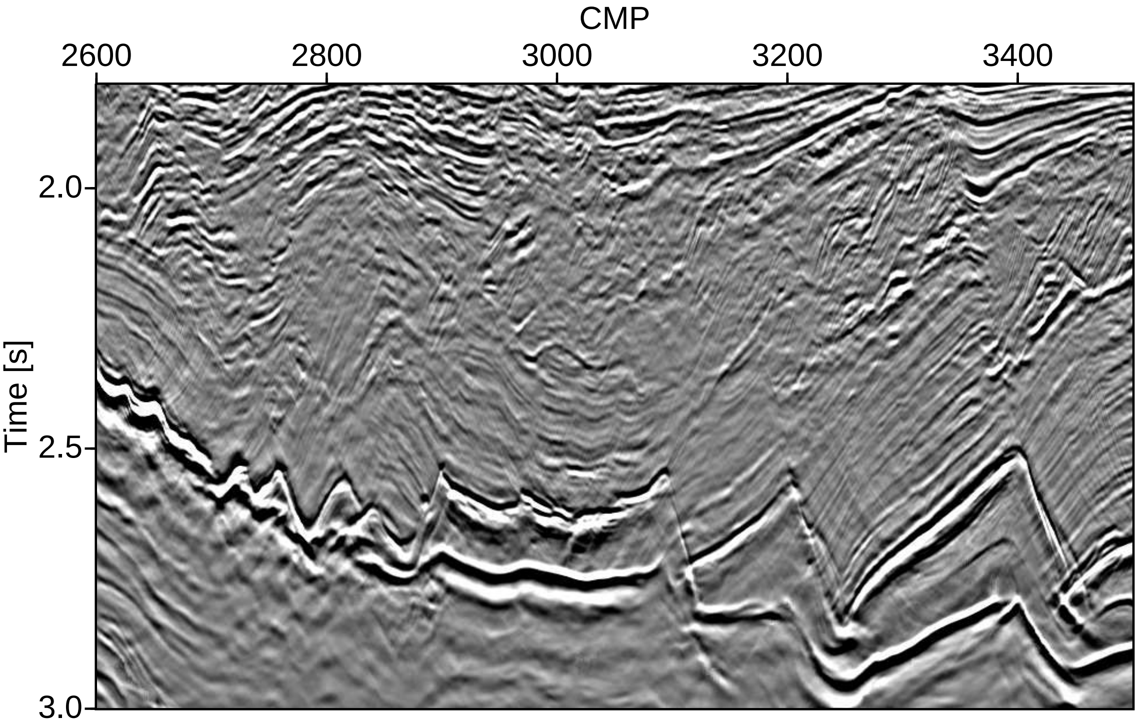

Figure 9.2.: Poststack time migration of the marine data.

9.2. Multiple prediction

Since the wavefront attributes are estimated automatically, sea floor multiples can be imaged, if not removed in pre-processing. However, the wavefront attributes can be used to remove multiples as well (Dümmong, 2010). Another simple method that takes almost no additional computational effort might be to take advantage of the dip corrected velocities. A horizontal sea floor produces multiples that bounce within the water column and arrive at times that are integral multiples of the primary reflection with the same moveout velocity as the primary reflection. Later arriving multiples intersect with deeper primary reflections but can be identified as multiples due to their differing moveout velocity. This is not necessarily the case for a dipping sea floor, as the apparent dip increases with each order of multiple. Since the moveout velocity is dip depended, the moveout velocity is not a valid choice to characterize multiples in general. The formulation of the implicit CRS operator allows a dip correction in form of Equation 2.26 which solves the problem of dipping sea floor multiples. Therefore, the dip corrected velocity can be used to predict multiples.

The approximate first arrival of the sea floor has to be predicted which can be done based on the coherence. The sea floor is a large impedance contrast with a more or less homogeneous overburden that produces a high coherence in most cases. Therefore, the sea floor should be the first layer of a significant increase of coherence. The first sea floor multiples are expected at traveltimes twice of the primary sea floor reflection. During the stacking process the algorithm can build an average of the dip corrected velocities at lower traveltimes and compare it to the moveout velocity at the considered sample. If it is lower than the average and similar to the dip corrected moveout velocity at the sea floor, the event can be considered as a multiple and stacked into a second section containing solely multiples.

After the application to every sample a CRS stack (Figure 9.3) and a stack of multiples (Figure 9.4) are available which, together with the moveout velocity field, can be used to adaptively subtract multiples from the prestack data. The predicted multiples are reliable for most parts, apart from salt body multiples. Particularly the bottom of salt is troublesome for this approach since the moveout velocity of the bottom of salt multiple does not differ much from the surrounding environment. However, this are just some first ideas and can be improved in the future.

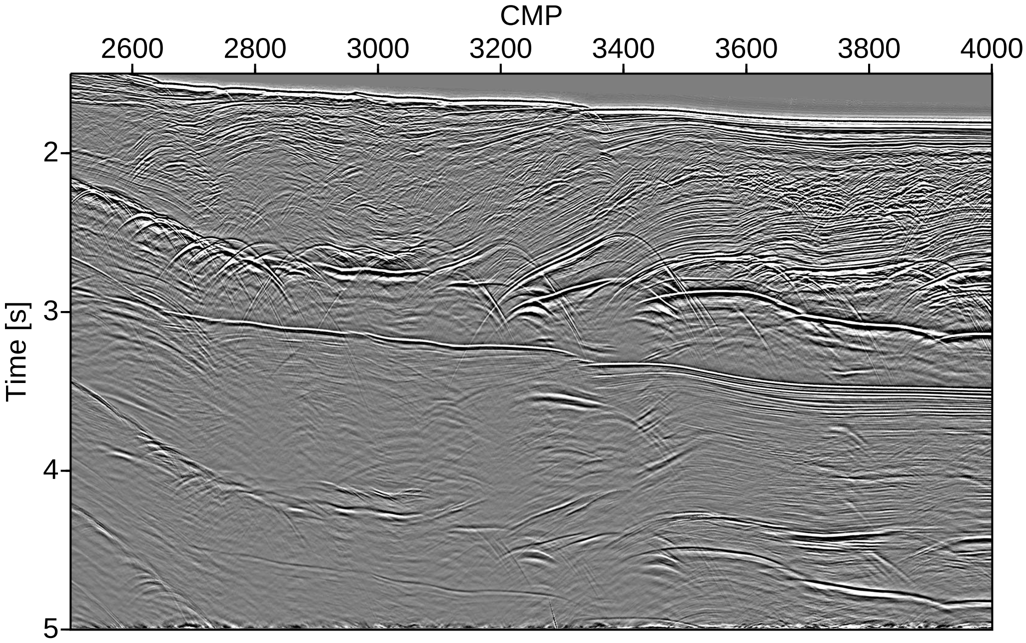

Figure 9.3.: Stack of the marine data set. The seafloor and deeper multiples blend with the subsurface at roughly 3 s.

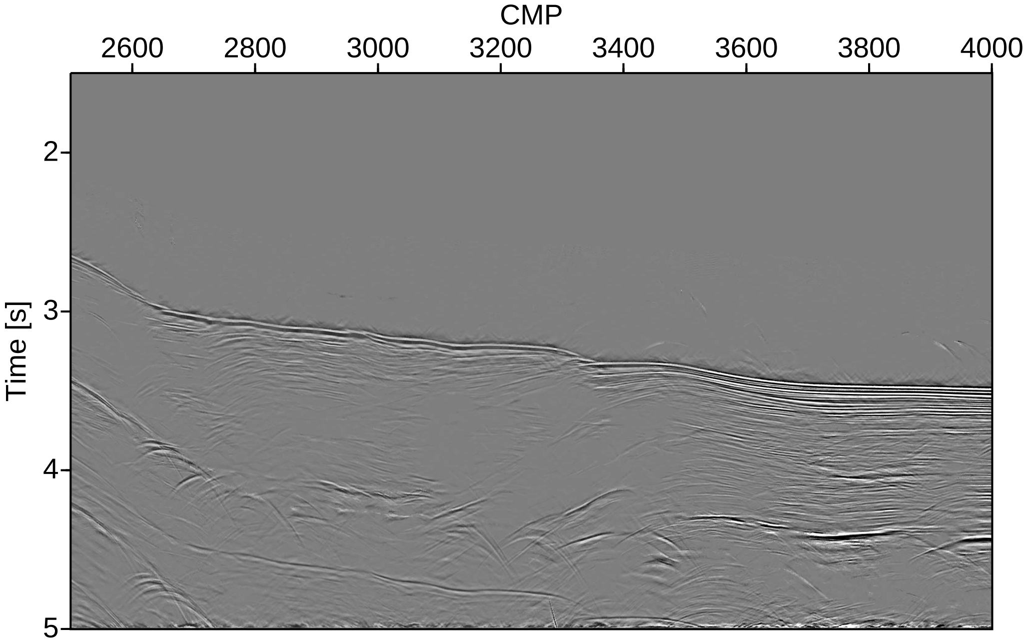

Figure 9.4.: Predicted multiples of the stack (Figure 9.3) based on the estimated dip corrected moveout velocity of Equation 2.26 shown in Figure 6.15. Most multiples are recognized except for salt body multiples, especially bottom of salt.

Appendices

Appendix A.

Nomenclature

Symbol	**Meaning**
A	Amplitude
α	Angle of emergence
C_R	Crossover parameter in differential evolution
C_S	Semblance
γ	Focusing parameter
h	Half-offset
H	Depth of circle
K_N	Curvature of normal wave
M	Width of time window
m	Coordinate of midpoint
μ	Mean value
N	Number of traces
N_P	Size of population
$\vec{\nabla}$	Gradient
O	Offspring in genetic algorithm
P	Prestack volume
p	Slowness
p_n	Gaussian probability distribution
R	Radius of circle
R_{CDS}	Radius of curvature for NIP or N wave in CDS operator
R_N	Radius of curvature of normal wave
R_{NIP}	Radius of curvature of normal-incidence-point wave
S	Stack
σ	Standard deviation
t	Traveltime
t_g	Traveltime from reflection point to receiver
t_s	Traveltime from source to reflection point
t_0	Zero-offset traveltime
θ	Reflection angle

V	Medium velocity
v_0	Near-surface velocity
V_{NMO}	Normal-moveout velocity
V_p	Velocity of primary wave
V_s	Velocity of shear wave
V_{tmig}	Time migration velocity
w	Weight in genetic algorithm
W_f	Diffraction weight
x_c	Central coordinate of circle
x_g	Coordinate of receiver
x_s	Coordinate of source
Δx_m	Midpoint displacement
Y	Parent in genetic algorithm
y	Mutation vector in differential evolution

Appendix B.

List of abbreviations

Abbreviation	Meaning
CDS	Common-diffraction-surface
CMP	Common-midpoint
COG	Common-offset gather
CRS	Common-reflection-surface
DE	Differential evolution
DMO	Dip-moveout
EA	Evolutionary algorithm
GA	Genetic algorithm
iCRS	Implicit common-reflection-surface
MF	Multifocusing
nCRS	Non-hyperbolic common-reflection-surface
NE	North-east
NIP	Normal-incidence-point
NMO	Normal-moveout
NW	North-west
SE	South-east
SW	South-west
ZO	Zero-offset

Appendix C.

Summary of publications

This is a list of works published during the course of the doctorate. Most of the works are cited in the text and therefore, appear in the bibliography as well.

Journal Papers

- Walda, J. and Gajewski, D. Determination and application of wavefront attributes by differential evolution and conflicting-dip processing. *submitted to Geophysics.*

Conference abstracts

- Walda, J. and Gajewski, D. (2015a). Common-reflection-surface stack improvement by differential evolution and conflicting dip processing. *SEG Technical Program Expanded Abstracts*, pages 3842–3847.

- Walda, J. and Gajewski, D. (2015b). Global optimization of the CRS operator using a genetic algorithm. *77th EAGE Conference and Exhibition 2015.*

- Walda, J. and Gajewski, D. (2015c). Handling the conflicting dip problem in the CRS/i-CRS method. *77th EAGE Conference and Exhibition 2015.*

- Walda, J., Schwarz, B. and Gajewski, D. (2016). A Competitive Comparison of Multi-parameter Stacking Approaches. *78th EAGE Conference and Exhibition 2016.*

Used software

Throughout the thesis I used a PC with a Unix operating system (Debian OS) under the GNU General Public License and part of a cluster called Thunder, operated by the Central IT Services (CIS), available to the applied geophysics working group in Hamburg.

The thesis is written with the typesetting software LaTeX.

The software developed in the framework of the thesis is based on a CRS implementation by Jürgen Mann with contributions from Sergius Dell and Mikhail Baykulov and is written in C++. It uses the Message Passing Interface (MPI) and is property of the Wave Inversion Technology (WIT) consortium.

Visualization and simple processing was done using the Seismic Un*x (Colorado School of Mine), Inkscape and PSTricks.

Acknowledgements

There are numerous people that helped during my studies in the Bachelor, Master and PhD program I would like to thank. I cannot thank all of them individually, since the list would grow too large. Nevertheless, I would like to thank those people who contributed continuously throughout my academic life.

I would like to thank

- **Dirk Gajewski** for the many opportunities, the freedom and support he gave me. He raised my interest in applied seismics during lectures, allowed me to join the working group as research assistant during my Bachelor thesis and made it possible for me to travel to Brazil, USA, Spain and Austria to present and attend at several conferences and workshops. Furthermore he gave me the opportunity and support to make my PhD at the University of Hamburg.

- **Claudia Vanelle** who helped me get familiar with and enjoy anisotropy as well as proofreading several works from me. Furthermore, thank you for allowing me to take charge of the exercises to lectures improving my teaching skills.

- **Ekkehart Teßmer** who helped me with programming and performance increasing issues as well as providing great ideas at several occasions.

- **TEEC** particularly Gerald Eisenberg-Klein and Henning Trappe for the opportunity to visit the company for short instances and test the developed method. The software I wrote within the thesis benefited tremendously from their input and the collaboration.

- **Sergius Dell** for so many information, feedback and discussions that increased my knowledge and made my work much more competitive. He is always willing to help.

- **Thomas Hertweck** for constructive feedback and interest during the early stage of this work and during consortium meetings and telling me about legal issues in the field of geophysics.

- **Dirk Becker** to let me be an assessor during oral exams of his lectures and review Bachelor thesis, thus giving me a broader idea of seismology and lecturing.

- **Martina Glöckner** for many discussions, all your feedback and proofreading as well as the many coffee sessions we shared.

- **Ivan Abakumov** for providing better insight to the zoo of multiparameter operators and particularly for testing first simple applications of the algorithm with your converted waves ideas.

- **Benjamin Schwarz** for many discussions and important critical yet constructive disputes.

- **Jesper Dramsch** who has become a good friend of mine over the years since we joined forces for semester exams in the master degree. Also thanks for company at the interesting open source software workshop and best of luck for your PhD program in Denmark.

- **Denys Zhurovich** a very interesting and great person who made working with the land data set possible.

- **Khawar-Ashfaq Ahmed** who is always cheerful and made the everyday life in the institute much more enjoyable. Also thanks for the trip to the NASA and the great experiences at the SEG annual meeting 2013 in Houston.

- **Philipp Witte** who is a major reason I looked more deeply into the optimization business.

- **Xie Yujiang** for important discussions and continuing the work for the 3-D case.

- **DOBREflection** for the land data.

- **TGS-NOPEC** for providing marine data.

- **SMAARTJV** for the synthetic data.

- **Family** for all the support I received during my studies. Without You I wouldn't have been able to achieve what I achieved.

- **Linnea Kemme**, my girlfriend who gave me all the support I needed at any given time. No words can describe how thankful I am to everything you did for me.

Bibliography

Abakumov, I., Kashtan, B., Schwarz, B., Vanelle, C., and Gajewski, D. (2012). Double-square root traveltime approximation for converted waves. *SEG Technical Program Expanded Abstracts.*

Bäck, T. (1996). *Evolutionary Algorithms in Theory and Practice.* Oxford Univ. Press.

Baker, J. (1985). Adaptive selection methods for genetic algorithms. In Grefenstette, J. and Erlbaum, L., editors, *Proceedings of the International Conference on Genetic Algorithms and Their Applications*, Hillsdale, NJ.

Barros, T., Ferrari, R., Krummenauer, R., and Lopes, R. (2015). Differential evolution-based optimization procedure for automatic estimation of the common-reflection surface traveltime parameters. *Geophysics*, 80(6):WD189–WD200.

Bauer, A., Schwarz, B., and Gajewski, D. (2016a). Enhancement of prestack diffraction data and attributes using a traveltime decomposition approach. *Studia Geophysica et Geodaetica*, pages 1–16.

Bauer, A., Schwarz, B., Lotze, M., Werner, T., and Gajewski, D. (2016b). Utilizing Diffractions in Wavefront-based Tomography. *78th EAGE Conference and Exhibition 2016.*

Baykulov, M. and Gajewski, D. (2009). Prestack seismic data enhancement with partial common-reflection-surface (CRS) stack. *Geophysics*, 74(3):V49–V58.

Bobsin, M., Schwarz, B., Vanelle, C., and Gajewski, D. (2015). Data-driven time migration using a multiparameter approach. *SEG Technical Program Expanded Abstracts*, pages 4350–4354.

Brest, J., Greiner, S., Boskovic, B., Mernik, M., and Zumer, V. (2006). Self-adaptive control parameters in differential evolution: a comparative study on numerical benchmark functions. *IEEE Transactions on Evolutionary Computation*, 10(6):646–657.

Das, S. and Suganthan, P. N. (2011). Differential Evolution: A survey of the state-of-the-art. *IEEE Transactions on Evolutionary Computation*, 15(1):4–31.

Davis, D. (1991). *Handbook of Genetic Algorithms.* Van Nostrand Reinhold, New York.

Dell, S., Downes, J., and Hertweck, T. (2013). Comparison of Non-hyperbolic and Standard CRS Using Complex Field Data. *SEG Technical Program Expanded Abstracts*, pages 4357–4361.

Dell, S. and Gajewski, D. (2011). Common-reflection-surface-based workflow for diffraction imaging. *Geophysics*, 76(5):S187.

Dell, S., Gajewski, D., and Vanelle, C. (2012). Prestack time migration by common-migrated-reflector-element stacking. *Geophysics*, 77(3):S73–S82.

Dümmong, S. (2010). *Seismic data processing with an expanded common reflection surface workflow.* PhD thesis, University of Hamburg.

Duveneck, E. (2004). Velocity model estimation with data-derived wavefront attributes. *Geophysics*, 69(1):265–274.

Eigen, M. (1973). *Ingo Rechenberg Evolutionsstrategie Optimierung technischer Systeme nach Prinzipien der biologischen Evolution.* Friedrich Fromman Verlag, Stuttgart-Bad Cannstatt.

Fomel, S. and Kazinnik, R. (2013). Non-hyperbolic common reflection surface. *Geophysical Prospecting*, 61(1):21–27.

Gelchinsky, B., Berkovitch, A., and Keydar, S. (1999a). Multifocusing homeomorphic imaging. *Journal of Applied Geophysics*, 42(3-4):229–242.

Gelchinsky, B., Berkovitch, A., and Keydar, S. (1999b). Multifocusing homeomorphic imaging: Part1. Basic concepts and formulas. *Journal of Applied Geophysics*, 42(3-4):229–242.

Glöckner, M., Schwarz, B., Vanelle, C., and Gajewski, D. (2016). Kinematic Time Demigration with an Automatically Generated Velocity Model. *78th EAGE Conference and Exhibition 2016.*

Goldberg, D. (1989). *Genetic Algorithms in Search, Optimization and Machine Learning.* Addison-Wesley Professional, 1 edition.

Goldberg, D. (1990). A note on Boltzmann tournament selection for genetic algorithms and population-oriented simulated annealing. Technical Report TCGA 90003, Engineering Mechanics, University of Alabama.

Górszczyk, A., Malinowski, M., and Bellefleur, G. (2015). Enhancing 3D post-stack seismic data acquired in hardrock environment using 2D curvelet transform. *Geophysical Prospecting*, 63(4):903–918.

Grefenstette, J. J. and Baker, J. (1989). How genetic algorithms work: a critical look at implicit parallelism. In *Proceedings of the Third International Conference on Genetic Algorithms*. Morgan Kaufmann, San Mateo, CA.

Guntern, C. (2016). Systematic Analysis of CRS-type operators. Master's thesis, University of Hamburg.

Höcht, G., Ricarte, P., Bergler, S., and Landa, E. (2009). Operator-oriented CRS interpolation. *Geophysical Prospecting*, 57(6):957–979.

Holland, J. H. (1975). *Adaption in Natural and Artificial Systems*. The University of Michigan Press, Ann Arbor.

Hubral, P. (1983). Computing true amplitude reflections in a laterally inhomogeneous earth. *Geophysics*, 48:1051–1062.

Jäger, R., Mann, J., Höcht, G., and Hubral, P. (2001). Common-reflection-surface stack: Image and attributes. *Geophysics*, 66:97–109.

Janikow, C. Z. and Michalewicz, Z. (1991). An Experimental Comparison of Binary and Floating Point Representations in Genetic Algorithms. pages 31–36.

Kitano, H. (1990). Designing Neural Networks Using Genetic Algorithms with Graph Generation System. *Complex Systems Journal*, 4:461–476.

Landa, E., Keydar, S., and Moser, T. J. (2010). Multifocusing revisited-inhomogeneous media and curved interfaces. *Geophysical Prospecting*, 58(6):925–938.

Liu, J. and Lampinen, J. (2002). On setting the control parameter of the differential evolution method. In *Proceedings of the 8th International Conference on Soft Computing (MENDEL)*, pages 11–18, Brno, Czech Republic.

Liu, J. and Lampinen, J. (2005). A fuzzy adaptive differential evolution algorithm. *Soft Computing*, 9(6):448–462.

Mann, J. (2001). Common-Reflection-Surface Stack and conflicting dips. *SEG Technical Program Expanded Abstracts*, Extended Abstracts:Session SP 5.3.

Mann, J. (2002). *Extensions and Applications of the Common-Reflection-Surface Stack Method*. PhD thesis, Logos Verlag, Berlin.

Mann, J., Jäger, R., Müller, T., Höcht, G., and Hubral, P. (1999). Common-reflection-surface stack - a real data example. *Journal of Applied Geophysics*, 42:301–318.

Mayne, W. H. (1962). Common reflection point horizontal data stacking techniques. *Geophysics*, 27(6):927–938.

Maystrenko, Y., Stovba, S., Stephenson, R., Bayer, U., Menyoli, E., Gajewski, D., Huebscher, C., Rabbel, W., Saintot, A., Starostenko, V., Thybo, H., and Tolkunov, A. (2003). Crustal-scale pop-up structure in cratonic lithosphere: DOBRE deep seismic reflection study of the Donbas fold belt, Ukraine. *Geology*, 31(8):733.

Menyoli, E., Gajewski, D., and Hübscher, C. (2004). Imaging of complex basin structures with the common reflection surface (CRS) stack method. *Geophysical Journal International*, 157(3):1206–1216.

Morris, G. M., Goodsell, D. S., Halliday, R. S., Huey, R., Hart, W. E., Belew, R. K., and Olson, A. J. (1998). Automated docking using a Lamarckian genetic algorithm and an empirical binding free energy function. *Journal of computational chemistry*, 19(14):1639–1662.

Mühlenbein, H. (1992). How genetic algorithms really work: I. Mutation and hillclimbing. In Männer, R. and Manderick, B., editors, *Parallel Problem Solving from Nature*, volume 2, North Holland, Amsterdam.

Müller, N. A. (2009). Treatment of conflicting dips in the 3D Common-Reflection-Surface stack. *Geophysical Prospecting*, 57(6):981–995.

Müller, T. (1999). *The Common Reflection Surface Stack Method: Seismic Imaging without explicit knowledge of the velocity model.* PhD thesis, University of Karlsruhe.

Netzeband, G. L., Gohl, K., Hübscher, C. P., Ben-Avraham, Z., Dehgani, G. A., Gajewski, D., and Liersch, P. (2006). The Levantine Basin-crustal structure and origin. *Tectonophysics*, 418:167–188.

Pedersen, M. E. H. (2010). Good parameters for differential evolution. Technical Report HL1002, Hvass Laboratories.

Price, R. (2005). *Differential Evolution: A Practical Approach to Global Optimization.* Springer.

Qin, A. K., Huang, V. L., and Suganthan, P. N. (2009). Differential Evolution algorithm with strategy adaption for global numerical optimization. *IEEE Transactions on Evolutionary Computation*, 13:398–417.

Qin, A. K. and Suganthan, P. N. (2005). Self-adaptive differential evolution algorithm for numerical optimization. In *Proceedings of the IEEE congress on evolutionary computation (CEC)*, pages 1785–1791.

Saintot, A., Stephenson, R., Stovba, S., and Maystrenko, Y. (2003). Structures associated with inversion of the Donbas Foldbelt (Ukraine and Russia). *Tectonophysics*, 373(1–4):181–207.

Schwarz, B. (2011). A new nonhyperbolic multi-parameter stacking operator. Master's thesis, University of Hamburg.

Schwarz, B. (2015). *Moveout and Geometry.* PhD thesis, University of Hamburg.

Schwarz, B., Bauer, A., and Gajewski, D. (2016). Passive seismic source localization via common-reflection-surface attributes. *Studia Geophysica et Geodaetica.*

Schwarz, B., Vanelle, C., and Gajewski, D. (2014a). Auxiliary Media-A Generalized View on Stacking. *76th EAGE Conference and Exhibition 2014.*

Schwarz, B., Vanelle, C., and Gajewski, D. (2015a). Shifted Hyperbola Revisited-The Two Faces of NMO. *77th EAGE Conference and Exhibition 2015.*

Schwarz, B., Vanelle, C., Gajewski, D., and Kashtan, B. (2014b). Curvatures and inhomogeneities: An improved common-reflection approach. *Geophysics*, 79(5):S231–S240.

Schwarz, B., Vanelle, C., Wißmath, S., Bauer, A., and Gajewski, D. (2015b). Efficient common-reflection-surface-based prestack slope determination for stereotomography. *SEG Technical Program Expanded Abstracts*, pages 5248–5253.

Soleimani, M., Piruz, I., Mann, J., and Hubral, P. (2009a). Common-Reflection-Surface stack: accounting for conflicting dip situations by considering all possible dips. *Journal of seismic exploration*, 18(3):271.

Soleimani, M., Piruz, I., Mann, J., and Hubral, P. (2009b). Solving the problem of conflicting dips in common reflection surface (CRS) stack. *1st International Petroleum Conference and Exhibition*, EAGE, expanded abstracts, A39.

Spinner, M. and Mann, J. (2007). CRS-based minimum-aperture time migration - A 2D land-data case study. *SEG Technical Program Expanded Abstracts*, pages 2354–2358.

Storn, R. (1996). On the usage of differential evolution for function optimization. In *Biennial Conference of the North American Fuzzy Information Processing Society (NAFIPS)*, pages 519–523.

Storn, R. and Price, K. (1997). Differential Evolution - a simple and efficient heuristic for global optimization over continues spaces. *Jornal of Global Optimization*, 11:341–359.

Taner, M. T. and Köhler, F. (1969). Velocity spectra-digital computer derivation applications of velocity functions. *Geophysics*, 34(6):859–881.

Tygel, M., Santos, L. T., and Schleicher, J. (1999). Multifocus moveout revisited: derivations and alternative expressions. *Journal of Applied Geophysics*, 42(3-4):319–331.

Walda, J. and Gajewski, D. (2015a). Common-reflection-surface stack improvement by differential evolution and conflicting dip processing. *SEG Technical Program Expanded Abstracts*, pages 3842–3847.

Walda, J. and Gajewski, D. (2015b). Global optimization of the CRS operator using a genetic algorithm. *77th EAGE Conference and Exhibition 2015*.

Walda, J. and Gajewski, D. (2015c). Handling the conflicting dip problem in the CRS/i-CRS method. *77th EAGE Conference and Exhibition 2015*.

Walda, J., Schwarz, B., and Gajewski, D. (2016). A Competitive Comparison of Multi-parameter Stacking Approaches. *78th EAGE Conference and Exhibition 2016*.

Wissmath, S. (2016). Finite-Offset CRS: Attribute Prediction and Application. Master's thesis, University of Hamburg.

Eidesstattliche Versicherung

Hiermit erkläre ich an Eides statt, dass ich die vorliegende Dissertationsschrift selbst verfasst und keine anderen als die angegebenen Quellen und Hilfsmittel benutzt habe.

Hamburg, den Unterschrift